Characterisation of Lateral Carrier Out-Diffusion and Surface Recombination in Ridge Waveguide Devices

Deepal Naidu, B.Sc. (Cardiff), M.Sc. (St-Andrews, Heriot-Watt)

Thesis submitted for the degree of Doctor of Philosophy

September 30, 2009

School of Physics and Astronomy

ProQuest LLC
789 East Eisenhower Parkway
P.O. Box 1346
Ann Arbor, MI 48106-1346

"History has demonstrated that the most notable winners usually encountered heartbreaking obstacles before they triumphed. They won because they refused to become discouraged by their defeats."

-B C Forbes

"A smooth sea never made a skilful sailor."

-English Proverb

"The journey is the reward."

-Chinese Proverb

Abstract

As laser devices are scaled down in size and involve the use of photonic structures etched through the active layer – a trend driven by the desire to improve device performance and functionality for future applications in optoelectronic integrated circuits – performance limiting mechanisms such as an increasing internal optical loss, deteriorating gain-mode overlap, lateral carrier out-diffusion and surface recombination can inflict restrictions on the further miniaturisation and overall performance.

In this project I have separately evaluated the relative impact of these mechanisms using ridge waveguide devices, with particular focus on the behaviour of the lateral out-diffusion and the surface-recombination mechanism in quantum-dot and quantum-well active regions. The approach of separately evaluating the relative impact of each mechanism is made possible by using the multisection characterisation technique. By this means the investigation in this study circumvents the problems associated with previous studies on lateral out-diffusion and surface recombination. Moreover, it furthers the overall analysis by measuring the effects as a function of injection-level and quantifying the change in non-radiative current density and overall internal quantum efficiency.

In quantum-dot shallow etched ridge waveguide devices (S-RWG) it is found that the mechanism of an increasing internal optical mode loss and increasing lateral out-diffusion current are the principal causes for the apparent increase in threshold current density with reducing ridge width from 10 to 4 μm. The internal optical loss was found to increase by a factor of 2.3 over this range and the non-radiative current density due to lateral out diffusion increased by a factor of 1.14 at an injection-level of 121 meV. The mechanism of a deteriorating gain-mode overlap was negligible in this range. Measurements of the lateral ambipolar diffusion length found that in self-assembled quantum-dot/wetting-layer systems the lateral ambipolar diffusion process can be inhibited in one of two ways: one good and one bad. This original result showed that the good way, in terms of benefiting the overall device performance, involves the inhibition due to three-dimensional carrier confinement in the quantum-

dots. The other involves populating the wetting-layer to a point where a higher order non-radiative recombination process reduces the average carrier lifetime and hence ambipolar diffusion length. Both regimes can reduce the loss of carriers to lateral carrier out-diffusion and surface recombination; however the latter is at the expense of increasing other non-radiative recombination processes. The ambipolar diffusion length was also found to be temperature dependent with a smaller diffusion length at lower temperatures. At 350 K the lateral ambipolar diffusion length varied from 0.75 μm to a maximum value of 1.5 μm over the injection-level range 65 meV to 84 meV. At 300 K the ambipolar diffusion length was smaller than 0.75 μm for injection-levels below 121 meV.

In quantum-well deep etched ridge waveguide devices (D-RWG) it was found that the D-RWG structure allowed much smaller ridge width (<2.8 μm) devices than S-RWG structures before as significant an increase in internal optical loss occurred. However, once a significant interaction of the wave amplitude and rough sidewalls does occur, the scattering loss in D-RWG structures was much more strongly affected. The D-RWG structure also provided no deterioration in the gain-mode overlap in the range 29 to 1.9 μm. A power law analysis of the measured non-radiative current density revealed that the principal threshold increasing mechanism in D-RWG devices was surface recombination. The fractional increase in threshold non-radiative current density for 1.5 mm lasers was significant. From a width of 29.1 to 9.6 μm the non-radiative current density increased by factor of 2 to a value of 462 A/cm^2, and from 29.1 to 2.8 μm by a factor of 11 to 2612 A/cm^2. The overall internal quantum efficiency at threshold in the 1.5 mm lasers was measured to significantly decrease as the ridge width was reduced. This is a direct consequence of an increasing fraction of applied current recombining via surface recombination. The measured decrease from a ridge width of 29.1 μm to 2.8 μm was 16.6 % to 1.8 %.

By characterizing the performance differences in the two RWG structures and the threshold increasing mechanisms of lateral out-diffusion and surface recombination in quantum-dot and quantum-well active regions respectively, knowledge of the criteria required for designing better devices for further miniaturisation and improved threshold performance was gained.

Acknowledgments

I would like to thank my supervisors, Prof. Peter Smowton and Prof. Huw Summers, for giving me the opportunity to conduct this research and for their guidance and support. The encouragement they both gave me during the difficult periods of the PhD was especially appreciated.

I would also like to thank the current and past members of the Optoelectronics group who helped create a friendly and stimulating research environment. In particular I would like to thank Angela Sobiesierski, Gareth Edwards, Karen Barnet, Chris Dunscombe and Dave Westwood for their support in the clean room. I would also like to thank Meletis Mexis, James Ferguson, Mohammed Al-Ghamdi, Gareth Mitchell, Stella Elliot, and Julie Lutti for their insightful discussions and support.

Finally I would especially like to thank my parents, Pagadal Swamy Srinivas (Sam) and Gita Naidu, and all my family for their belief in me and their endless encouragement. A special thanks also goes to my girlfriend Ayako Agarie. She has been extremely supportive and has inspired me endlessly.

Contents

Chapter 1: Thesis Rationale and Background

1.1 Presentation

With the successful integration of the electronic integrated circuit as a precursor, there is a natural progression towards integrating electronic and optical components together on a single multi-component chip. The vision is to achieve the advantages of what integration did for electronics: Future integrated optoelectronic circuits (OEICs) are to provide complete systems with enhanced performance, improved functionality, smaller sizes, improved reliability and lower cost compared with their system counterparts of interconnected discrete electronic and optical components. For example OEICs can utilise the inherent parallelism of optical components i.e. simultaneously transferring information on many beams of light or wavelengths as opposed to the serial nature of electronic transistors [1, 2]. Such integration can also eliminate the need for optical fibre interconnects thus greatly reducing the size and system costs and simplifying alignment issues. The potential aggregation of different optical and electronic components offers varied multi-functionality OEICs. This is particularly useful for specialised functions such as in medicine where OEICs are anticipated to provide 'Lab-on-a-chip' optical biosensors for cell diagnostics [3].

One major challenge for future OEICs is the successful integration and scaling-down of a laser light source that is comparable in size to the electronic components. In conventional semiconductor lasers, such as edge-emitting ridge-waveguides and VCSELs, scaling-down can offer lower threshold currents, higher modulation bandwidths and mode control. However performance limiting mechanisms such as an increasing internal optical loss, deteriorating gain-mode overlap, lateral carrier out-diffusion and surface recombination can inflict restrictions on the size and overall performance. These mechanisms are also relevant when photonic components are etched and incorporated into the active region (e.g. photonic crystal cavity lasers and distributed feedback gratings). Carriers diffusing laterally can either be lost to non-radiative surface recombination at an exposed surface or interface, or lost to recombination processes outside of the pumped area where round trip amplification occurs (lateral out-diffusion). The lateral diffusion length of carriers in the active

region is therefore a limiting factor on the size and performance of all semiconductor optoelectronic devices. For this reason material systems with small lateral carrier diffusion lengths are highly desirable for further device miniaturization and integration with photonic components. Part of this PhD project is to separately investigate the restrictions these individual mechanisms place on reducing the size of the ridge width in ridge-waveguide semiconductor laser devices. Focus is put on the effects of: (1) the internal optical loss, (2) gain-mode overlap, and primarily, (3) the loss of carriers to recombination processes outside of the pumped area where round trip amplification occurs (lateral out-diffusion), and (4) the loss of carriers to recombination at exposed sidewalls of the active region (surface recombination).

The process of lateral diffusion is also strongly governed by the dimensionality of the active region. In quantum-wells (QW), carrier confinement in the growth direction restricts diffusion to the two dimensions of the QW plane. By further reducing the dimensionality for confinement in two dimensions (quantum-wire [4]) or ideally in all three dimensions (quantum-dot) the diffusion of carriers can be further restricted. In an ideal quantum-dot system, where the dots are isolated zero-dimensional states, three-dimensional confinement completely localises carriers and thereby prevents diffusion. The zero-dimensional nature is also anticipated to provide many other advantages for quantum-dot active regions over quantum-well active regions [e.g. 5, 6]. Benefits such as reduced threshold current densities, temperature insensitive operation and high differential gain have already been demonstrated in self-assembled quantum-dot systems formed by the Stranski-Krastanow (S-K) growth mode [7]. However, due to dot size inhomogeneity and the formation of a wetting-layer, S-K self-assembled quantum-dots still fall short of the virtues predicted for an ideal quantum dot system. The implication on the lateral diffusion mechanism is one of the interests in this project since the presence and proximity of the 2-dimensional wetting-layer might well provide a means for lateral diffusion to occur. The process is thought to be: thermal escape into the wetting layer where carriers can diffuse along the two-dimensional plane; recapture into a dot; and eventual recombination of the electron-hole pair at some point in the structure. This coupled transport mechanism is anticipated to inhibit lateral carrier diffusion rather than completely suppressing it.

The effects of lateral out-diffusion and surface recombination on device performance have mainly been experimentally investigated by characterising the ambipolar diffusion length and surface recombination velocity. The techniques used to do this have varied from cathodoluminescence [8, 9], photoluminescence [10, 11, 12], electron-beam scanning [13], optical pump-probe [14], to I-V and L-I characteristics [15]. In most of these cases the measurements are not carried out on proper laser diode structures, or under electrical injection, or under proper working conditions e.g. high injection-level. Measurements under high injection-level conditions are preferred for understanding and optimisation of device characteristics. Investigations on the ambipolar diffusion length and surface recombination velocity under proper working conditions have been demonstrated in edge-emitting broad area [16, 17] and ridge waveguide [18, 19, 20, 21] lasers by fitting the threshold current dependence on the ridge width. These reports have relied on specific laser models and sets of assumptions to characterise the gain, optical mode, and recombination properties. Moreover other key mechanisms which can potentially affect the threshold and hence fitting of the data, such as an increasing internal optical loss and deteriorating gain-mode overlap, are not all taken into account. The focus of these studies, whilst useful, lack insight into the effects lateral out-diffusion and surface recombination have on device characteristics such as the recombination processes at threshold (radiative and non-radiative), overall internal quantum efficiency, changes in the gain-mode overlap, or the dependence as a function of injection-level.

One of the primary interests in this project involves characterising the effects of lateral out-diffusion and surface recombination on device performance in quantum-dot and quantum-well ridge waveguide devices. To gain a more complete understanding of the processes and resulting effects, we are not only interested in determining the ambipolar diffusion length, but also to experimentally characterise the modal gain, internal optical loss, radiative and non-radiative recombination current densities, and overall internal quantum efficiency, all as a function of carrier injection-level and ridge width. The approach we use circumvents the problems with previous techniques by: separately evaluating the mechanisms involved in the threshold dependence on ridge width, experimentally evaluating the gain, internal optical loss, and recombination processes, measuring the characteristics under high injection-levels and as a function of injection-level, and fitting a standard diffusion

length model to data that is only affected by the lateral out-diffusion effect. The techniques used include the multisection method [22] and laser threshold measurements.

Through evaluating these measured characteristics as a function of ridge width and carrier injection-level we present an investigation into the lateral out-diffusion effect in quantum-dot ridge waveguide devices. The investigation looks into modal gain, internal optical loss, radiative and non-radiative recombination processes, and the lateral ambipolar diffusion length. In an S-K quantum-dot system the mechanisms of lateral carrier transport and hence the lateral diffusion length in the coupled system of quantum-dots, wetting-layer, and quantum-well barrier are still indefinite. Reports have either suggested that lateral diffusion primarily occurs in the wetting layer [15] or barrier region prior to relaxation into the dot [23]. Part of this project analyses the lateral ambipolar diffusion length as a function of carrier injection-level so as to provide a clearer picture of the mechanisms involved. In doing so we illustrate that the lateral ambipolar diffusion length is a strong function of Fermi-level separation i.e. population of higher energy states in the quantum-dot and wetting-layer. The observed dependence is an original result and highlights that recombination in either the 2-dimensional wetting layer or surrounding quantum-well structure can affect the lateral ambipolar diffusion length with further carrier injection.

We present an investigation into the effects of surface recombination in quantum-well deep-etched ridge waveguide devices. By analysing the gain, internal optical loss, radiative and non-radiative recombination processes, and overall internal quantum efficiency, we are able to accurately explain the observed threshold current density dependence with ridge width. In such structures and even VCSELS, a threshold increase is often attributed to an increase in non-radiative recombination at the exposed sidewalls. In the investigation we are able to directly correlate and quantify the threshold increase to an increase in non-radiative recombination, and moreover associate it with surface recombination. The investigation also highlights the effect surface recombination has on the overall internal quantum efficiency. We find the internal quantum efficiency to be a strong function of carrier injection-level and also ridge width i.e. as the surface recombination process becomes evermore dominant.

1.2 Background

In order to provide a familiarisation with some of the terms and concepts relevant to this project, what follows is a brief revision of some background material. A more detailed account of the topics presented and also other topics are covered in good semiconductor laser physics and semiconductor physics text books such as [24] [25].

1.2.1 Ridge Laser Diode

The basic structure of a conventional edge-emitting ridge waveguide (RWG) laser diode with a separate confinement heterostructure is illustrated in Figure 1-1.

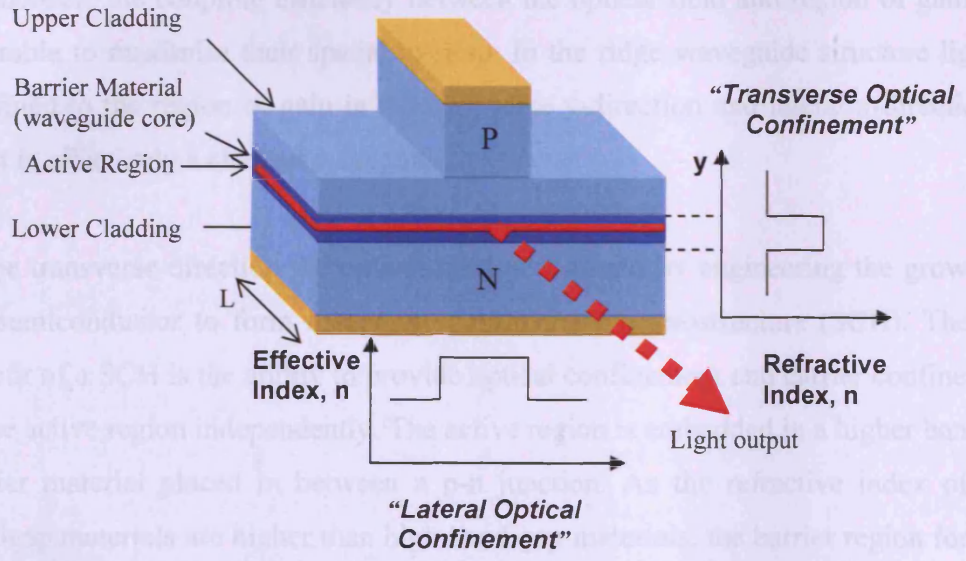

Figure 1-1. Illustration of the basic structure of a conventional ridge waveguide laser diode

The RWG device in Figure 1-1 consists of three basic components required for lasing action:

- A light-amplifying medium provided by the active region under the conditions of population inversion.
- A pump source provided by electrical injection of carriers into the active region

- A resonant optical cavity formed by cleaving the end facets at right angles to form two co-parallel partially reflecting mirrors (i.e. a Fabry-Perot optical cavity)

When a forward bias is applied to the laser diode, electron and hole carriers are injected into the active region to create a population inversion whereupon electrons in the conduction band and holes in the valence band can recombine radiatively to produce light of photon energy equal to the energy difference between the electron and hole states. As the emitted light is partially reflected back and forth through the active region it can grow in intensity (optical gain) by stimulating further electron-hole carrier recombination and generating more identical photons. Lasing action is obtained when the round-trip gain experienced by the light intensity equals the total optical losses. The whole process is initiated by spontaneous emission.

To increase the coupling efficiency between the optical field and region of gain it is desirable to maximise their spatial overlap. In the ridge waveguide structure light is confined to the region of gain in the transverse y-direction and lateral x-direction in what is effectively a channel waveguide.

In the transverse direction the optical field is confined by engineering the growth of the semiconductor to form a separate confinement heterostructure (SCH). The key benefit of a SCH is the ability to provide optical confinement and carrier confinement in the active region independently. The active region is embedded in a higher bandgap barrier material placed in between a p-n junction. As the refractive index of low bandgap materials are higher than high band gap materials, the barrier region forms a region of high refractive index (i.e. waveguide core) and the n and p regions form regions of low refractive index (i.e. waveguide cladding layers), in what is effectively a slab waveguide. Since the width of the barrier region can be changed without affecting the dimensions of the active regions, the optical mode profile can be controlled independently of the carrier confinement in the active region. In a similar way, because the width of the active region can be reduced without significantly affecting the optical mode profile, low-dimensional structures (such as quantum-wells and quantum-dots) can be used as active regions to facilitate the use of carrier quantisation effects without affecting the transverse waveguiding. Under forward bias, the p-n junction supplies carriers to the active region. The transport of carriers beyond

the active region and barrier is inhibited by the hetero-barriers formed between the core and cladding materials.

In the lateral direction, light guided within the slab waveguide has part of its amplitude in the cladding regions through its evanescent field. The evanescent wave in the upper cladding region experiences a refractive index step between the ridge and the surroundings. Within the ridge there is a higher refractive index so again optical confinement takes place.

The RWG structure also benefits from another type of guiding effect which is created by manipulation of the input current geometry to confine the gain region into a small region under the ridge. This then has an effect on the light field in that it can only be amplified and allowed to oscillate within that region.

Together the optical waveguiding in the transverse and lateral directions improve the spatial overlap between the optical field and gain profile in the ridge, thus increasing coupling efficiency and improving device performance.

1.2.2 Laser Threshold and Modal Gain

The amplification of light intensity is characterised by the optical modal gain (G). The modal gain in terms of space is defined as the fractional increase of light intensity in a given optical mode per unit distance. To obtain lasing action in the laser cavity, the optical modal gain provided by active region must equal the total optical loss. In the laser cavity the optical loss can be divided into the output (mirror) loss (α_m) caused by light transmission at the facets (a useful process), and the internal optical loss (α_i), which combines the effect of all other mechanisms such as scattering and free carrier absorption. At the laser threshold condition, the modal gain satisfies the round-trip amplification condition, given by

$$G = \alpha_i + \frac{1}{2L}\ln\left(\frac{1}{R_1 R_2}\right) = \alpha_i + \alpha_m \tag{1.1}$$

where L, R_1 and R_2 are respectively the cavity length, front facet reflectivity and back facet reflectivity (both are approximately around 0.3 for a GaAs/Air semiconductor interface.

In the laser cavity the optical gain provided by the active region typically occupies only a few percent of the volume occupied by the optical mode. Thus the modal gain expressed in (1.1) is actually representative of an overlap integral function between the optical mode profile and the localised material gain (g) profile which gives the net gain provided to the optical mode. For in-plane lasers the gain is commonly assumed to be invariant in x, y and z within the active region [24], however this may not always be the case. With this assumption the modal gain provided by the overlap between the optical mode profile and material gain profile is typically expressed as

$$G = \Gamma g \tag{1.2}$$

where Γ is termed the optical confinement factor and is defined as the ratio of the integrated light intensity within the active region (i.e. region of gain) to the total optical intensity throughout the laser structure.

1.2.3 Optical Transitions

The three types of optical transitions that can occur between two energy levels are illustrated in Figure 1-2.

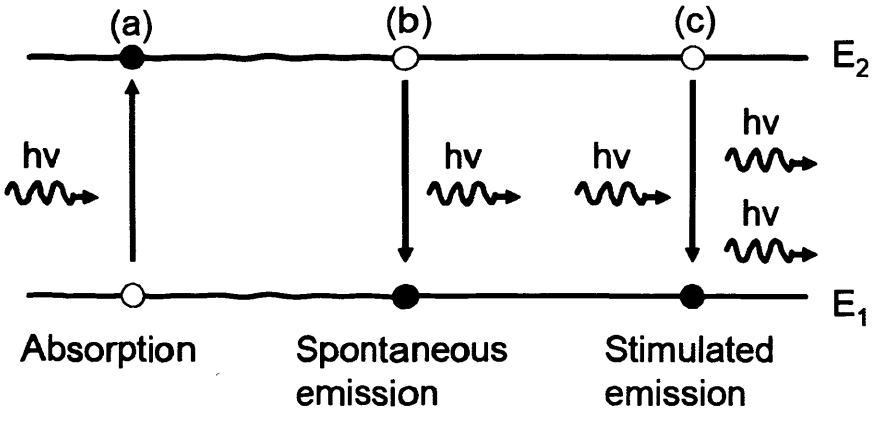

Figure 1-2. Illustration of the optical absorption (a), spontaneous emission (b) and stimulated emission (c) processes that can take place between two energy levels.

(a) Optical absorption. The energy of a photon equal to the energy difference between E_2 and E_1 is transferred to the electron causing an excitation to an empty state in E_2.

(b) Spontaneous emission. An electron in E_2 spontaneously relaxes to a free state in E_1, losing its energy to the generation of a photon ($hv=E_2-E_1$). This process is entirely random and generates photons with random phase and directions.

(c) Stimulated emission. An incoming photon of energy equal to the difference between E_2 and E_1, stimulates the electron in E_2 to relax to the lower energy state E_1, and lose its energy in the form of a new photon with equal phase, energy and direction as the incoming photon.

All of these processes are dependent on the occupation probability of either an electron or empty state (hole) being at a given energy state. In general the probability distribution of carriers can be described by Fermi-Dirac statistics, which for electrons is:

$$f = \frac{1}{e^{E-E_f/kT}+1} \tag{1.3}$$

where f is the probability of occupancy at energy E, E_f is the Fermi-level, k is the Boltzmann's constant, and T is the temperature. The Fermi-level is defined as the level where the Fermi function is equal to a half.

1.2.4 Non-radiative Recombination

1.2.4.1 Defect and Impurity Recombination

Defects and impurities in the crystal lattice can locally perturb the covalent bonding pattern of the crystal lattice and result in a localised energy state within the bandgap. Such energy states serve to trap an electron from the conduction band temporarily before releasing it to the valence band in what is an overall non-radiative process. This type of recombination is also known as Shockley-Read-Hall recombination due to work they did in studying this mechanism's recombination rate. The recombination rate of this mechanism is determined by the carrier with the slowest capture rate.

Furthermore, the recombination rate is reduced the closer the defect states are to the conduction band edge or valence band edge.

1.2.4.2 Surface Recombination

Surface recombination is analogous to defect and impurity recombination. It occurs at the exposed surface of the active region where the abrupt termination of the crystal lattice leaves behind unmatched bonds which result in defect states occurring in high density. The high densities essentially form a mini-band as opposed to individual energy levels. Surface recombination can be characterised by a surface recombination velocity rather than by a lifetime, τ, of carriers distributed throughout the whole active region volume. The surface recombination velocity is given by a capture rate of carriers located within some capture length, L_{cap}, of the surface [24]:

$$v_s = \frac{L_{cap}}{\tau} \tag{1.4}$$

1.2.4.3 Auger Recombination

Auger recombination is an indirect recombination of electron and hole carriers. The mechanism can require the involvement of additional carriers, collisions and phonons to conserve energy and momentum. There are several different Auger processes that can occur. The Auger recombination rate should increase rapidly as the carrier density increases because the mechanism is dependent on the presence of multiple carriers.

1.2.5 Quantum-Confinement

When the dimension of the active region is reduced to a size comparable to the wavelength of an electron, quantum confinement effects alter the allowed energy states in the conduction and valence band. To consider one dimension, the energy difference between the narrow-bandgap active region and wide-bandgap barrier material creates a one-dimensional potential well for charge carriers. The effect of the potential energy barriers on the behaviour of the charge carriers is considered by solving the time-independent Schrödinger's equation, which in one dimension is given by

$$\frac{\partial^2\psi(x)}{\partial x^2}+\frac{2m^*}{\hbar}(E-V(x))\psi(x)=0$$

(1.5)

where m* is the effective mass of the charge carrier, V(x) is the potential profile experienced by the charge carrier, E is the energy of the charge carrier, and ψ(x) is the wavefunction of the charge carrier. The potential energy barrier height experienced by electrons in the conduction band and holes in the valence band will be set by the band offsets.

In the case of an infinite potential well of width L, Schrödinger's time-independent equation can be solved to reveal that the energy of a carrier is quantised i.e. the carrier can only have particular discrete energy values:

$$E=E_n=n^2\left(\frac{\hbar^2\pi^2}{2m^*L^2}\right)$$

(1.6)

where n is the quantum number and is a positive integer. The n=1 state is the lowest energy state and is called the ground state. This state is often the one under most consideration as it is the most favourable for carrier population in accordance with the Fermi-Dirac carrier distribution. The lowest optical transition energy in a quantum-confined material is then the sum of the bandgap between the conduction and valence band plus the energy of the quantised states for electrons in the conduction band and holes in the valence band.

From the quantisation of the allowed energy states in the infinite potential well, it follows that the carrier wavefunctions for each quantised energy state will also be discrete and will have a standing wave distribution given by:

$$\psi(x)=\sqrt{\frac{2}{L}}\sin\left(\frac{n\pi}{L}x\right)$$

(1.7)

1.2.5.1 Low-dimensional active regions

When a semiconductor material is reduced in size to confine carriers in one or more dimensions by the quantum-confinement effect, the system is described as being low-

dimensional. A material system that confines carriers in one spatial dimension (quantum-well) is referred to as two-dimensional because carriers are only free to move in the two remaining dimensions. Similarly, material systems that confine carriers in two (quantum-wire) and three spatial dimensions (quantum-dot) are referred to as one-dimensional and zero-dimensional; with the latter providing complete carrier confinement.

1.2.5.2 Quantum-Wells

Quantum-well active regions are formed by sandwiching a narrow-bandgap semiconductor in between two layers of wider-bandgap semiconductor. The thickness of the quantum-well (typically 10 nm) is made comparable to the carrier wavelength to form a one-dimensional potential well. Size quantisation effects, as describe in the previous section, will form discrete energy states in the growth direction. However, in the plane of the quantum-well the energy states are not discrete and are given by the effective mass approximation of the energy band structure. Therefore in the plane of the quantum-well carriers are free to move around. The energy of an electron in the conduction band is given as

$$E = E_c + \frac{n^2\hbar^2\pi^2}{2m_e^* L^2} + \frac{\hbar^2(k_x^2 + k_z^2)}{2m_e^*} \tag{1.8}$$

where E_c is the conduction band energy, m_e^* is the effective mass of an electron in the conduction band, k_x and k_y are the wave-vector components from the two-dimensional band structure. A similar equation can be formed for the holes in the valence band.

Introducing energy quantisation into the active region and hence decreasing the dimensionality will significantly alter the density of states. The density of states gives a measure of the maximum number of carriers that can occupy an energy range. Illustrated in Figure 1-3 is the change in the density of states (DOS) for a quantum-well and quantum-dot in comparison to a bulk semiconductor material with no size quantisation of the energy spectrum. The density of states for a quantum-well is a step-like function. This type of function offers an improvement in performance over laser devices incorporating active regions with no carrier confinement. This is because the number of carriers populating the conduction band and valence band is largest

near the edges, whereas in the bulk material the density of states is small near the edges and increases as square root of increasing energy. The larger density of states near the band edges is more favourable for laser applications because the contribution of the higher energy states to the laser threshold is suppressed [26]. As a result of this and the quantised energy states the threshold current density will be reduced and so will its temperature dependence.

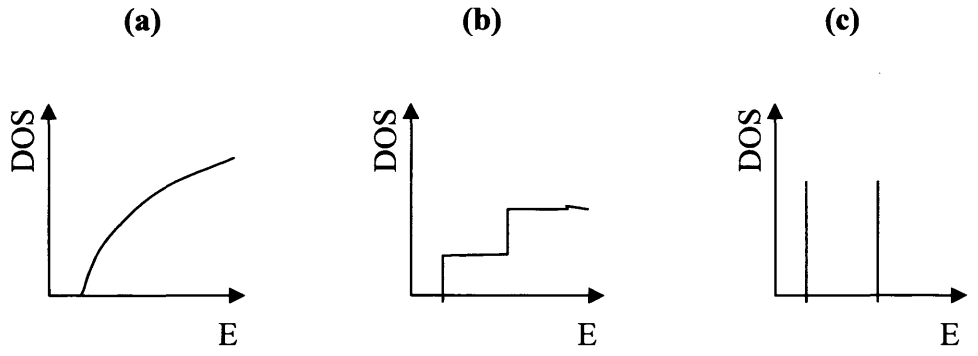

Figure 1-3. Density of states (DOS) as a function of energy for bulk material (a), a quantum-well (b), and a quantum dot (c).

1.2.5.3 Quantum-Dots

Quantum dots are the ultimate case of carrier confinement in all three dimensions which results in an energy spectrum consisting of discrete 'atom-like' energy levels. They are formed by surrounding a small sized narrow bandgap semiconductor island, of dimensions comparable to the carrier wavelength in x,y and z, by a wider bandgap material in all three dimensions The effect on the density of states is an even further improvement in comparison to bulk material and to quantum-wells in that delta function-like peaks centred at the energy levels are produced. This concentrates injected carriers to occupy an even narrower range of energy states. As such the density of charge carriers accumulated at the lasing transition is significantly enhanced at the expense of other energy states. This results in an even lower applied current density being required to reach threshold.

The fabrication of ideal semiconductor quantum-dot active regions has so far proved difficult. Of the various techniques tried to date the most prolific is the formation of

quantum-dots by self-assembly using the Stranski-Krastanow (S-K) growth mode. Quantum-dot active regions formed by this method have shown improved device characteristics such as reduced threshold current densities, temperature insensitive operation and high differential gain [7]. The method is a strain-induced self-organised growth mode whereby a lattice mismatched narrow-bandgap material is grown on the barrier material by epitaxy. The biaxial compressive strain induced by the mismatch is initially accommodated in the first few monolayers of growth. These initial layers are called the wetting-layer. After deposition of a few more monolayers the strain energy increases and so as to relieve some of this built up strain the growth mode switches from planer growth to the formation of three-dimensional islands. This growth mode can occur for a lattice mismatch as small as or even smaller than e.g. 7 % as observed for InAs dots grown on GaAs. One of the disadvantages of this technique is that the self-forming islands appear spontaneously and their sizes, composition and shape fluctuate leading to an inhomogeneous energy distribution of the whole quantum-dot ensemble rather than the idealised discrete 'atomic-like' energy transitions. These quantum-dot systems also suffer from the presence of excited energy states which are comparably spaced with the thermal energy of the carriers. In an ideal quantum-dot system the energy levels would be widely spaced in energy such that the probability of thermal activation of carriers to the excited states would be greatly reduced.

1.2.6 Carrier Transport

1.2.6.1 Carrier Drift and Diffusion

The movement of charge carriers (electrons and holes) in semiconductors can be categorised into two main transport mechanisms: carrier drift and diffusion. Carrier drift is the process whereby carriers move under the influence of an applied electric field. Carrier diffusion is when carriers flow from a region of high concentration to low concentration as a result of their random thermal motion.

A drift current arises when an electric field (E) is applied to a semiconductor. The electric field produces a force on charge carriers inside a semiconductor and as a result the carriers will have a net acceleration and net movement. This net movement

of charge is called drift. The total drift current density (J_{dft}) is the sum of the electron and hole carrier drift current densities:

$$J_{dft} = e(\mu_n n + \mu_p p)E \tag{1.9}$$

Where e is the electronic charge and n and p are the electron and hole carrier densities. The parameter μ_x is the carrier mobility where the subscript is used to indicate the mobility for either electrons or holes. The mobility describes how well a carrier moves under an applied electric field and it is related to the average velocity of a carrier that results from scattering events inside the semiconductor. In low electric fields this relation is given by $v_d = \mu E$.

Diffusion current arises when there is a carrier density gradient with the flow of charge carriers being from a region of high carrier concentration to low concentration. The total diffusion current density (J_{dif}) is the sum of the electron and hole carrier diffusion current densities which for a one-dimensional case is given by:

$$J_{dif} = e\left(D_n \frac{dn}{dx} - D_p \frac{dp}{dx}\right) \tag{1.10}$$

The parameter D_x is the carrier diffusion coefficient where the subscript x is used to indicate the diffusion coefficient for either electrons or holes. The diffusion coefficient describes how well a carrier moves in a semiconductor as a result of a density gradient. Although drift and diffusion are independent current mechanisms, the mobility and diffusion coefficient are no independent parameters. For non-degenerate semiconductors the relationship between the mobility and diffusion coefficient are given by the Einstein relationship, $D_x = (kT/q)\cdot\mu_x$. In the case of degenerate conditions the Einstein relationship becomes a function of the Fermi-level (i.e. carrier concentration) and is of the form, $D_x = 2/3\cdot(E_f/q)\cdot\mu_x$.

The total current density is the sum drift current density and diffusion current density for both electrons and holes which for a one-dimensional case is reduced to:

$$J = e(\mu_n n + \mu_p p)E + e\left(D_n \frac{dn}{dx} - D_p \frac{dp}{dx}\right) \tag{1.11}$$

1.2.6.2 Continuity Equations

The continuity equations describe how the carrier density in a semiconductor behaves with time and space. The general form of the continuity equation for electrons and holes are given by [25]

$$\frac{\partial n}{\partial t} = -\frac{1}{e}\nabla \cdot J_n + g_n - \frac{n}{\tau_n} \tag{1.12}$$

$$\frac{\partial p}{\partial t} = -\frac{1}{e}\nabla \cdot J_p + g_p - \frac{p}{\tau_n} \tag{1.13}$$

where g_n and g_p are the excess electron and hole generation rates caused by an external influence such as optical excitation. The last term on the right hand side of the equations are the excess carrier recombination rates where τ_n and τ_p are the excess carrier lifetimes for electrons and holes respectively. J_n and J_p are the total current densities for electrons and holes and are given by the sum of their drift and diffusion current density components.

For simplicity, we can consider the continuity equations in one-dimension and substitute in the drift and diffusion current density components of J_n and J_p into equations (1.12) and (1.13) to obtain the time-dependent diffusion equations for electrons and holes:

$$D_n \frac{\partial^2 n}{\partial x^2} + \mu_n\left(E\frac{\partial n}{\partial x} + n\frac{\partial E}{\partial x}\right) + g_n - \frac{n}{\tau_n} = \frac{\partial n}{\partial t} \tag{1.14}$$

$$D_p \frac{\partial^2 p}{\partial x^2} + \mu_p\left(E\frac{\partial p}{\partial x} + p\frac{\partial E}{\partial x}\right) + g_p - \frac{p}{\tau_p} = \frac{\partial p}{\partial t} \tag{1.15}$$

The carrier concentration, n, is given by the sum of the thermal equilibrium carrier concentration (n_0) and the excess carrier concentration (δn). However, since the

thermal equilibrium concentrations are independent of time and also space in a homogeneous semiconductor, only the derivatives of the excess carrier concentration need be considered in equations (1.14) and (1.15).

1.2.6.3 Ambipolar Diffusion

Excess electrons and holes do not move independently of each other. They drift and diffuse with the same effective drift mobility and diffusion coefficient. When electrons and holes are injected into the semiconductor, they drift apart in an electric field and diffuse with different speeds. This causes a spatial separation of charge which induces an internal electric field, creating a force of attraction between the two sets of charge carriers. The force of attraction holds the electron and hole carriers together, causing them to drift or diffuse together with a single mobility (μ_a) or diffusion coefficient (D_a). This transport mechanism is called ambipolar diffusion. The internal electric field created by the excess electron and hole concentrations is given by Poisson's equation

$$\nabla \cdot E_{\text{int}} = \frac{e(\delta p - \delta n)}{\varepsilon} = \frac{\partial E_{\text{int}}}{\partial x} \tag{1.16}$$

where ε is the permittivity of the semiconductor material.

By assuming the excess concentration of electrons and holes are approximately the same (i.e. approximate charge neutrality at any point in space and time; $\delta n \approx \delta p$) and noting that the generation rates and recombination rates are the same (e.g. $g_n = g_p = g$) because the electrons and holes are created and annihilated in pairs, the time dependent diffusion equations can be combined to give the ambipolar diffusion equation

$$D_a \frac{\partial^2 \delta n}{\partial x^2} + \mu_a E \frac{\partial \delta n}{\partial x} + g - R = \frac{\partial \delta n}{\partial t} \tag{1.17}$$

where

$$D_a = \frac{\mu_n n D_p + \mu_p p D_n}{\mu_n n + \mu_p p} \tag{1.18}$$

$$\mu_a = \frac{\mu_n \mu_p (p-n)}{\mu_n n + \mu_p p} \tag{1.19}$$

and R is the ambipolar recombination rate. Using Einstein's relations the ambipolar diffusion coefficient can then be reduced to

$$D_a = \frac{D_n D_p (n+p)}{nD_n + pD_p} \tag{1.20}$$

In applying equation (1.17) to model the steady-state lateral carrier density profile in the intrinsic active region of a laser, as is done in Chapter 4, a high-level injection regime is taken and simplifications can be made: Under high-level injection in the active region, $\delta n \approx \delta p >> n_i^2$, where n_i is the intrinsic carrier concentration in thermal equilibrium and is given by $n_o p_o$. In an undoped active region quasi charge neutrality is maintained [27]. The carrier generation rate term can be ignored as carriers are injected into the active region electrically with a current density J_d. In this regime the ambipolar diffusion equation is given by [28][20]

$$D_a \frac{\partial^2 \delta n}{\partial x^2} + \frac{J_d}{e} - R = 0 \tag{1.21}$$

and D_a reduces to

$$D_a = \frac{2 D_n D_p}{D_n + D_p} \tag{1.22}$$

1.3 Summary

In summary, this chapter has introduced the rationale of the thesis, as well as a brief on low-dimensional semiconductor ridge laser diodes and the carrier transport mechanisms.

The importance of suppressing the lateral carrier diffusion mechanism for realising continued improvements in device performance and integration with miniaturisation was discussed. Low-dimensional active regions were summarised and, by virtue of their 3-dimensional carrier confinement, quantum-dot material systems were put

forward as a potential means of suppressing lateral diffusion as compared to quantum-wells. A succinct revision of some of the terms and concepts relevant to the thesis was presented with particular focus on the steady-state ambipolar diffusion equation for a high injection-level regime in ridge lasers. The next chapter provides details of the experimental approach used in the investigations.

[1] S. S. Jha, "Perspectives in Optoelectronics", World Scientific Publishing Co. Pte. Ltd. 1994
[2] M. Dagenais, R. F. Leheny, J. Crow, "Integrated Optoelectronics," Academic Press, Inc. 1995.
[3] P. N. Prasad, "Nanophotonics," Wiley-Interscience, John Wiley & Sons, Inc. 2004.
[4] E. Kapon, D. M. Hwang and R. Bhat, "Stimulated emission in semiconductor quantum wire heterostructures," Physical Review Letters 63, 4, p430, 1989.
[5] Y. Arakawa and H. Sakaki, "Multidimensional quantum well laser and temperature dependence of its threshold current", Applied Physics Letter, 40, 939-941. 1982.
[6] M. Asada, Y. Miyamoto and Y. Suematsu, "Gain and threshold of three dimensional quantum box lasers", IEEE Journal of Quantum Electronics, QE-22, 1915-1921. 1986.
[7] D. Bimberg and N. Ledentsov, " Quantum dots: lasers and amplifiers", Journal of Physics: Condensed Matter, 15, R1063-1076. 2003.
[8] S. Evoy, G. F. Redinbo, and H. G. Craighead, "Cathodoluminescence and photoluminescence analysis of InGaAs/GaAs quantum well structures," Applied Physics Letters, 68, 9, p1259, 1996. Letters, 81, 2, p346, 2002.
[9] V. Malyarchuk, J. W. Tomm, V. Talalaev, and Ch. Lienau, "Nanoscopic measurements of surface recombination velocity and diffusion length in a semiconductor quantum well," Applied Physics
[10] R. J. Nelson, J. S. Williams, H. J. Leamy, B. Miller, H. C. Casey, Jr., B. A. Parkinson, and A Heller, "Reduction of GaAs surface recombination velocity by chemical treatment," Applied Physics Letters, 36, 1, p76, 1980.
[11] W. S. Hobson, F. Ren, U. Mohideen, R. E. Slusher, and M. Lamont Schnoes, "Silicon nitride encapsulation of sulfide passivated GaAs/AlGaAs microdisk lasers," Journal of Vacuum Science Technology, A, 13, 3, p642, 1995.
[12] A. Shaw, H. Folliot, and J. F. Donegan, "Carrier diffusion in InAs/GaAs quantum dot layers and its impact on light emission from etched microstructures," IOP Nanotechnology, 14, p571-577, 2003.
[13] L. Jastrzebski, J. Lagowski, and H. C. Gatos, "Application of scanning electron microscopy to determination of surface recombination velocity: GaAs," Applied Physics Letters, 27, 10, p537, 1975.
[14] K. Tai, T. R. Hayes, S. L. McCall, and W. T. Tsang, "Optical measurements of surface recombination in InGaAs quantum well mesa structures," Applied Physics Letters, 53, 4, p302, 1988.
[15] A. Fiore, M. Rossetti, B. Alloing, C. Paranthoen, and J. X. Chen, "Carrier diffusion in low-dimensional semiconductors: A comparison of quantum wells, disordered quantum wells, and quantum dots," Physical Review B, 70, 205311, 2004.
[16] B. W. Hakki, "Carrier and gain spatial profiles in GaAs stripe geometry lasers," Journal of Applied Physics, 44, 11, 1973.
[17] W. T. Tsang, "The effects of lateral current spreading, carrier out-diffusion, and optical mode losses on the threshold current density of GaAs-AlGaAs stripe geometry DH lasers," Journal of Applied Physics, 49, 3, p1031, 1978.
[18] S. Y. Hu, D. B. Young, A. C. Gossard, and L. A. Coldren, "The effects of lateral leakage current on the experimental gain/current-density curve in quantum-well ridge waveguide lasers," IEEE Journal of Quantum Electronics, 30, 10, p2245-2250, 1994.
[19] S. Y. Hu, S. W. Corzine, K.-K. Law, D. B. Young, A. C. Gossard, L. A. Coldren, and J. L. Merz, "Lateral carrier diffusion and surface recombination in InGaAs/AlGaAs quantum-well ridge-waveguide lasers," Journal of Applied Physics, 76, 8, p4479-4487. 1994.
[20] G. J. Letal; J. G. Simmons, J. D. Evans and G. P. Li, "Determination of active-region leakage currents in ridge-waveguide strained-layer quantum-well lasers by varying the ridge width," IEEE Journal of Quantum Electronics, 34, 3, p512-517, 1998.
[21] S. A. Moore, L. O'Faolain, M. A. Cataluna, M. B. Flynn, M. V. Kotlyar and T. F. Krauss, "Reduced surface sidewall recombination and diffusion in quantum-dot lasers," IEEE Photonics Technology Letters, 18, 17, p1861-1863, 2006.

[22] P. Blood, G. M. Lewis, P. M. Smowton, H. Summers, J. Thompson, and J. Lutti, "Characterisation of semiconductor laser gain media by the segmented contact method," IEEE Journal of Selected Topics in Quantum Electronics, 9, 5, p1275, 2003.
[23] D. P. Popescu, P. G. Eliseev, A. Stintz, and K. J. Malloy, "Carrier migration in structures with InAs quantum dots," Journal of Applied Physics, 94, 4, p2454-2458, 2003.
[24] L. A. Coldren and S. W. Corzine, "Diode lasers and photonic integrated circuits," Wiley Series in Microwave and Optical Engineering, 1995.
[25] D. A. Neamen, "Semiconductor Physics and Devices," 3rd Edition, McGraw-Hill, 2003.
[26] V. M. Ustinov, A. E. Zhukov, A. Y. Egorov, and N. A. Maleev, "Quantum dot lasers," Oxford University Press, 2003.
[27] G. Adolfsson, S. Wang, M. Sadeghi,, J. Bengtsson, A. Larsson, J. J. Lim, V. Vilokkinen, P. Melanen, " Effects of lateral diffusion on the temperature sensitivity of the threshold current for 1.3μm double quantum-well GaInNAs-GaAs lasers," IEEE Journal of Quantum Electronics, 44, 7, p607-616. 2008
[28] W. Joyce, "Carrier transport in double-heterostructure active layers," Journal of Applied Physics, 53, p 7235-7239. 1982.

Chapter 2: Experimental Procedures

2.1 Multisection Device Characterisation Technique

2.1.1 Overview

The experimental techniques used in this project, including the multisection method for gain and recombination processes, laser wavelength and optical power and laser near-field, are described in this chapter.

The multisection characterisation technique [1, 2, 3] is based on measurements of single-pass edge-emitted amplified spontaneous emission ASE as a function of pumped amplification length from a single test-structure. These measurements allow the modal gain spectra, modal loss spectra, internal optical loss, spontaneous emission spectra, radiative current density, non-radiative current density, and overall internal quantum efficiency to be characterised.

The multisection test-structure is illustrated in Figure 2-1. It consists of 5 identical 300 μm long sections which are electrically separated by a 4 μm break in the p-contact and GaAs+ capping layer. These breaks limit current leakage into neighbouring sections thereby allowing each section to be individually pumped. Optical feedback is prevented in the device by a damaged back facet and a long passive absorbing region that is formed by choosing not to excite the back three sections. Length dependent ASE measurements are carried out by electrically exciting either section 1, section 2 or both simultaneously. As such, the amplification length can be made to vary from L to 2L. A detailed description of how this test-structure is fabricated is given in Chapter 3.

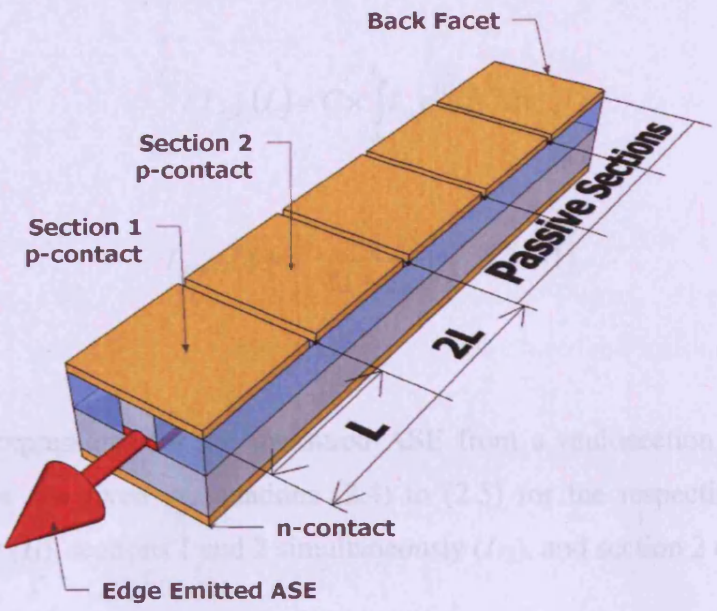

Figure 2-1. Architecture of the multisection test-structure

2.1.2 Measured Amplified Spontaneous Emission

A point source of spontaneous emission of a particular polarisation, per unit energy interval, per second, and per unit area of the active region is given by I_{sp}. After amplification by a net gain $(G-\alpha_i)$ over a distance x, the intensity from I_{sp} is given by [4]:

$$I(x) = I_{sp} e^{(G-\alpha_i)x} \tag{2.1}$$

Where G is the modal gain and α_i is the internal optical loss for that polarisation.

An expression for the externally measured single-pass amplified spontaneous emission (ASE) intensity from a uniformly pumped section of length L can be found by integrating for all amplified point source intensities (i.e. equation (2.1)) over the excitation length L and taking account of a measurement calibration factor, C. The measurements calibration factor includes the effects due to the fraction of spontaneous emission that couples into the waveguide, the facet reflectivity, collection geometry, and the calibration factor of the measuring apparatus [3]:

$$I_{ASE}(L) = C \times \int_0^L I_{sp} e^{(G-\alpha_i)x} dx \tag{2.2}$$

$$I_{ASE}(L) = C \cdot \frac{I_{sp}}{G-\alpha_i} \cdot \left(e^{(G-\alpha_i)L} - 1\right) \tag{2.3}$$

From (2.3), expressions for the measured ASE from a multisection device can be formed. These are given in equations (2.4) to (2.5) for the respective pumping of section 1 only (I_1), sections 1 and 2 simultaneously (I_{12}), and section 2 only (I_2).

$$I_1 = C \cdot \frac{I_{sp}}{G-\alpha_i} \cdot \left(e^{(G-\alpha_i)L} - 1\right) \tag{2.4}$$

$$I_{12} = C \cdot \frac{I_{sp}}{G-\alpha_i} \cdot \left(e^{(G-\alpha_i)2L} - 1\right) \tag{2.5}$$

$$I_2 = C \cdot \frac{I_{sp}}{G-\alpha_i} \cdot \left(e^{(G-\alpha_i)L} - 1\right) \cdot \left[e^{-(A+\alpha_i)L}\right] \tag{2.6}$$

A is the modal absorption of the un-pumped region and is a positive quantity. The exponential term in square brackets thereby accounts for the absorption of the ASE through the un-pumped section 1 region of length L.

2.1.3 Net Modal Gain and Net Modal Loss

An analytical expression for the net modal gain, G-α_i, can be obtained by comparing the ASE between different amplification lengths. In the multisection analysis the ASE intensity from an amplification length of L (equation (2.4)) and $2L$ (equation (2.5)) are compared to give:

$$G-\alpha_i = \frac{1}{L}\ln\left(\frac{I_{12}}{I_1}-1\right)$$

(2.7)

This expression allows the net modal gain spectra to be obtained in absolute units from the measured ASE spectra of the multisection device. The expression is independent of spontaneous emission and also measurement calibration factor.

By using a similar approach, an expression for the net modal loss spectrum, $(A+\alpha_i)$, can be obtained by comparing equations (2.4) and (2.6) to give the following analytical equation which is also independent of I_{sp} and the measurement calibration factor:

$$(A+\alpha_i) = \frac{1}{L}\ln\left(\frac{I_1}{I_2}\right)$$

(2.8)

Given in Figure 2-2 is an example of a net modal gain (G-α_i) and net modal loss ($A+\alpha_i$) spectra from a quantum-dot system. At the low energy region, the gain and loss spectra converge to a loss value that corresponds to the internal optical loss [3][5]. In this region there is zero optical gain and zero optical absorption and as such the only loss experienced by the optical mode is from scattering and free carrier absorption. In the example, α_i is measured to be 3.4 cm^{-1}. If the internal optical loss is approximately invariant across the spectra, then the value for α_i can be used to convert the net modal gain and loss spectra into a modal gain (G) and modal absorption (A) spectra. This then allows the transparency energy to be determined from the high energy point where the modal gain (G) equals zero.

For a system in quasi-thermal equilibrium the transparency energy is equivalent to the quasi-Fermi level separation, ΔE_f. The quasi Fermi level separation is used throughout the investigations in this project as an intrinsic measure of how hard a device is being pumped. This facilitates characteristics of different devices to be compared at a common level of pumping. For example in Chapter 4 the modal gain spectra of

different ridge width devices are compared at a common quasi-Fermi level separation to evaluate changes in the overlap between the optical mode profile and material gain profile. Such evaluation processes are discussed in more relevant detail in the experimental results chapters.

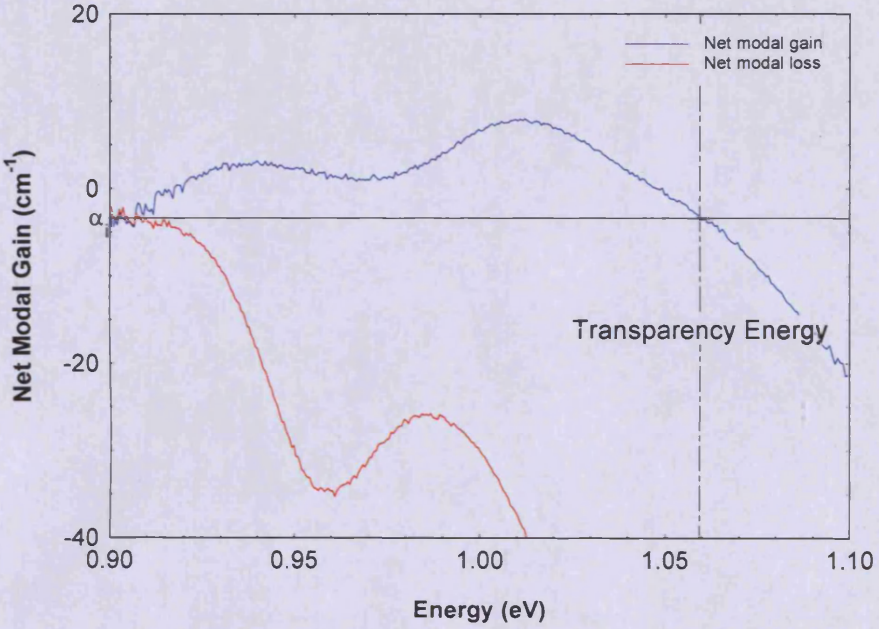

Figure 2-2. Net modal gain and net modal loss spectra from a quantum-dot device at a drive current density of 883 A/cm^2.

2.1.4 Spontaneous Emission

In a similar manner to the derivation of the net modal gain, equations (2.4) and (2.5) can also be compared to obtain an analytical expression for the measured spontaneous emission spectrum, $C.I_{sp}=[I_{sp}]_m$, in arbitrary units:

$$[I_{sp}]_m = C \cdot I_{sp} = \frac{1}{L}\ln\left(\frac{I_{12}}{I_1}-1\right)\cdot\frac{I_1^2}{I_{12}-2I_1} \tag{2.9}$$

To obtain the unamplified spontaneous emission spectrum, I_{sp}, in real units of per unit energy interval, per second, per unit area of the active region, it is necessary to

determine the measurement calibration factor, C. The approach used to do this – as first described by [2] – determines C from an analysis of the population inversion factor, Pf, which for a specific polarisation is proportional the ratio of the measured modal gain (G) to measured spontaneous emission ($[I_{sp}]_m$); and from [3] is given as:

$$Pf = \frac{f_1 - f_2}{f_1(1-f_2)} = C\left(\frac{n^2(h\nu)^2 w_{\text{mod}}}{3\hbar^3 c^2 \pi^2}\right)\left(\frac{G}{[I_{sp}]_m}\right) \tag{2.10}$$

Where w_{mod} is the effective optical mode width across the active region in the growth direction, and is defined as the width of the active region over the transverse optical confinement factor. Parameters f_1 and f_2 are the occupation probabilities for an electron in the upper and lower states of the transition at photon energy $h\nu$. Their values range from 0 to 1 indicating unoccupied or fully occupied states respectively. As such the population inversion factor describes the occupancy of the electrons and holes at transition energy $h\nu$. The population inversion factor tends to unity and saturates with increasing current when either f_1=1, f_2=0, or f_1=1 and f_2=0. In the measured spectrum the region where this usually occurs is at low photon energies. In Figure 2-3 an example of a Pf spectrum obtained from a quantum-dot system is shown for various drive current densities. The region where the Pf spectrum saturates can readily be identified at low photon energies and as such equation (2.10) can be set to unity and the measurement calibration factor can be determined. This method of calibrating data has been successfully applied in a number of studies to characterise both quantum-well and quantum-dot material systems [2, 6, 7, 8]. Alternatively, if the system is in quasi thermal equilibrium, the Pf spectrum can be described by Fermi-Dirac statistics [2, 9]:

$$Pf = C\left(1 - e^{\left(\frac{h\nu - \Delta E_f}{kT}\right)}\right) \tag{2.11}$$

Equation (2.11) can then be fitted to the measured Pf spectrum using the value of ΔE_f obtained from transparency energy on the modal gain spectrum. These thermal fits can be used to indicate where the Pf spectra saturate and tend to unity. In Figure 2-3

the P*f* spectra are all fitted with equation (2.11). Once C is known the measured spontaneous emission spectra can be calibrated into real units by application of equation (2.9). An example of spontaneous emission spectra, I_{sp}, from a quantum-dot system is given in Figure 2-4.

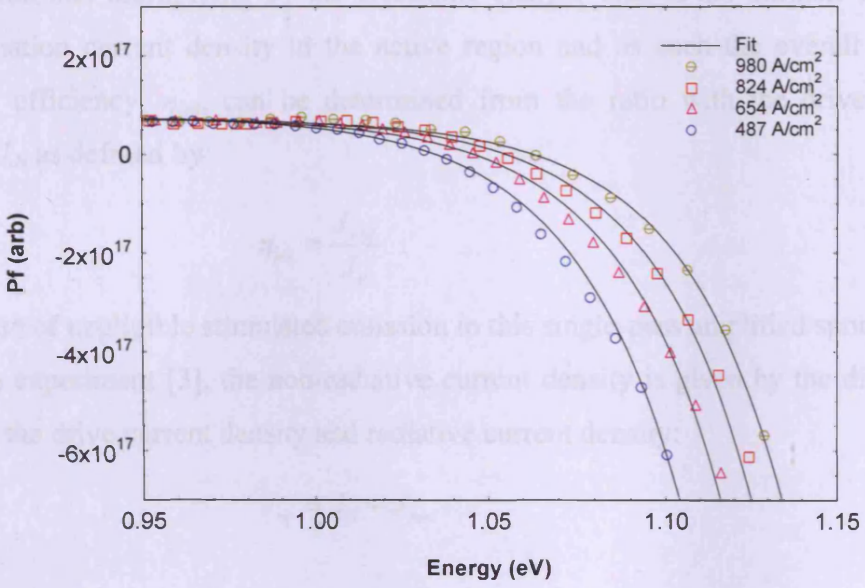

Figure 2-3. Example of a P*f* spectrum taken from a quantum-dot system for various current densities. The open symbols are the measured data and the solid line is a fit using (2.11.

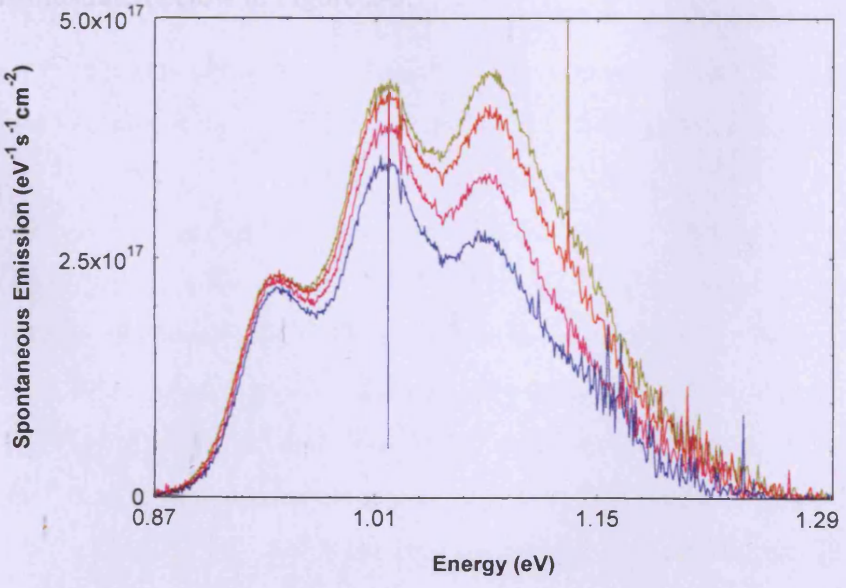

Figure 2-4. Example of the spontaneous emission spectrum, I_{sp}, from a quantum-dot system for various current densities.

2.1.5 Radiative and Non-Radiative Current Density and the Overall Internal Quantum Efficiency

Having determined the spontaneous emission spectra, the radiative current density, J_{rad}, can be found by summing the integrated spontaneous emission spectra for each polarisation and multiplying by the electronic charge. This is the intrinsic radiative recombination current density in the active region and as such the overall internal quantum efficiency, η_{int}, can be determined from the ratio with the drive current density, J_d, as defined by:

$$\eta_{\text{int}} = \frac{J_{rad}}{J_d} \tag{2.12}$$

In the case of negligible stimulated emission in this single-pass amplified spontaneous emission experiment [3], the non-radiative current density is given by the difference between the drive current density and radiative current density:

$$J_{nr} = J_d - J_{rad} \tag{2.13}$$

2.1.6 Experimental Set-up

The experimental set-up used for measuring the ASE from a multisection test-structure is illustrated below in Figure 2-5:

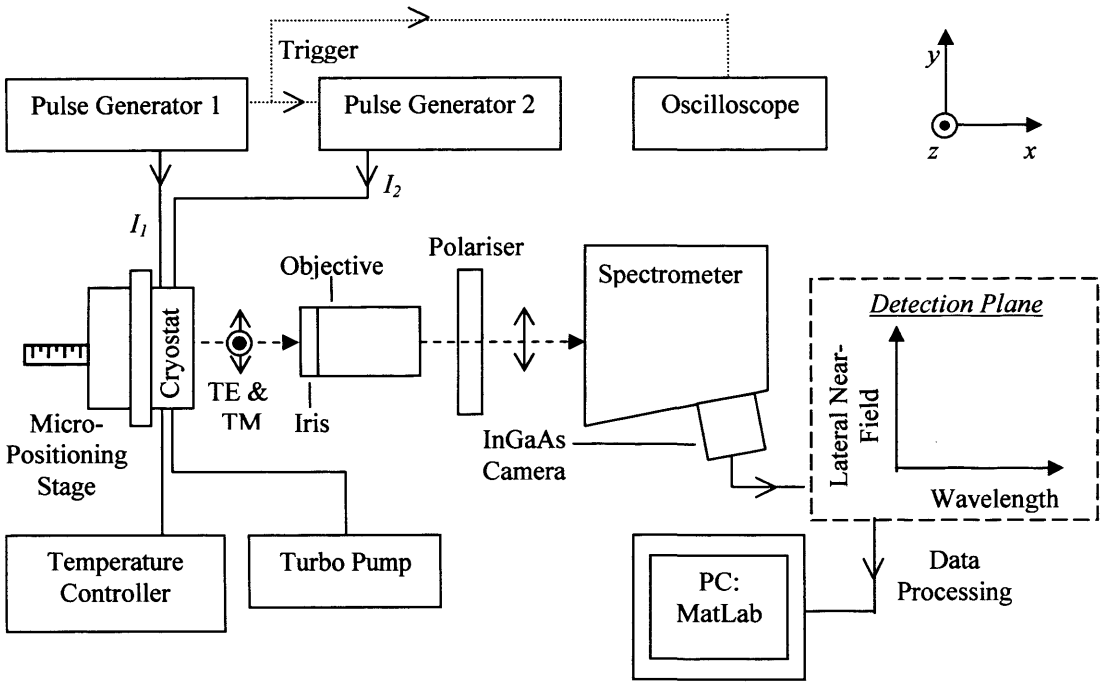

Figure 2-5. Schematic of the experimental set-up used to measure ASE from a multisection test structure.

The experimental apparatus was initially assembled by Dr. Craig Walker for measuring the threshold current and lasing wavelength from a laser as a function of temperature. The system also had an additional intention for multisection experiments on oxide-stripe multisection test-structures. Since then improvements have been made in the collection-geometry, device alignment, and current calibration to allow ASE measurements on ridge waveguide multisection test-structures where the signal levels and emission area are much reduced in comparison to broad area oxide stripe devices.

The device is placed in an Oxford Instruments MicrostatN cryostat and is operated by two pulse generators; one for section 1 and one for section 2. To avoid heating effects a low duty cycle of typically 0.25 % was used to drive each section. An oscilloscope and current probe are used to monitor the current output from the pulse generators. To maintain the temperature of the device the cryostat is attached to an Oxford Instruments ITC601 temperature controller and a vacuum system and with liquid nitrogen cooling through an inlet in the cryostat and an internal heating element, the temperature can be controlled from 80 K to 500 K.

Edge-emitted light is collected by a microscope lens with an iris diaphragm that limits the geometrical collection half-angle to approximately 10°. The collected light is focused onto the entrance slit of a spectrometer. A polariser is placed in the optical path of the focused light to select either TE or TM polarised emission. For accurate alignment of the image of the device onto the entrance slits and for the collection of light that emerges from pumped region of the device only (essential for accurate modal gain measurements [9]), the cryostat is fixed to a micro-positioning stage that has 6 degrees of movement: linear movement along x, y, and z; and rotation in the x-y, x-z, and y-z planes.

The ASE spectrum is measured by a Xenics Xeva 1.7-320 Infrared InGaAs camera which can measure wavelengths within the range 850 nm to 1700 nm. The camera detection plane is placed at the output plane of the spectrograph. The diffraction grating in the spectrograph disperses light in the x-y plane, and as such the x-axis of the camera corresponds to wavelength. The camera is spectrally calibrated with the infrared transition lines of a HeNe laser source. By orientating the device such that the growth direction is perpendicular to the x-y plane, the y-axis of the camera is made to image the lateral near-field (i.e. across the plane of the active region) of the device. The detection mode in the InGaAs camera consists of integrating the incident light over a fixed period of time. This integration time is adjusted depending on the light level. Data output is in a text file data array representing the pixels of the camera.

A MatLab program was written by me to process the data giving the final output in the form of analysis e.g. modal gain spectra, spontaneous emission spectra. The program first zeros the data with respect to the background signal and calibrates it with respect to the system response. Then it allows the user to spatially select the centre of the lateral near-field and averages over a typical width of 10 pixels in the y-axis. Subsequently data from different grating centre wavelengths are spectrally stitched together and then analysed. The amplitude response of the experimental set-up is calibrated with an Oriel quartz tungsten halogen lamp from Newport. The light from the lamp is measured in accordance to the collection distance and voltage setting specified by the manufacturer. Calibration of system is then readily done using the ratio of measured response from the lamp to the known response as quoted by the manufacturer.

2.2 Laser Measurements

The experimental set-up illustrated in Figure 2-5 can also be used for measuring the lasing wavelength and light-current characteristic of a laser device (as initially setup by Dr. Craig Walker). This set-up has the advantage of being able to: maintain the temperature, determine the polarisation of the lasing mode, monitor the lasing wavelength, and monitor the lateral near-field. The last two points are especially useful for observing filamentation and changes in the lasing mode with increasing current. Such changes are often said to be the cause of kinks in the L-I curve above threshold, but here we are able to directly correlate such effects.

The experimental routine is similar to the ASE measurements from a multisection test-structure. A laser device is placed inside the cryostat and is temperature controlled. The device is connected to a pulse generator and is driven with a duty cycle that is the same as for the ASE multisection measurements. Light is collected by the microscope objective and focused through the polariser and into the spectrometer where the light is dispersed in the x-y plane and imaged onto the InGaAs camera. The x- and y- axis of the camera's InGaAs array again correspond to wavelength and lateral near-field respectively. An example of the lasing wavelength and lateral near-field from a deep-etched 5.8 μm ridge waveguide quantum-well device taken using this set-up is given in Figure 2-6.

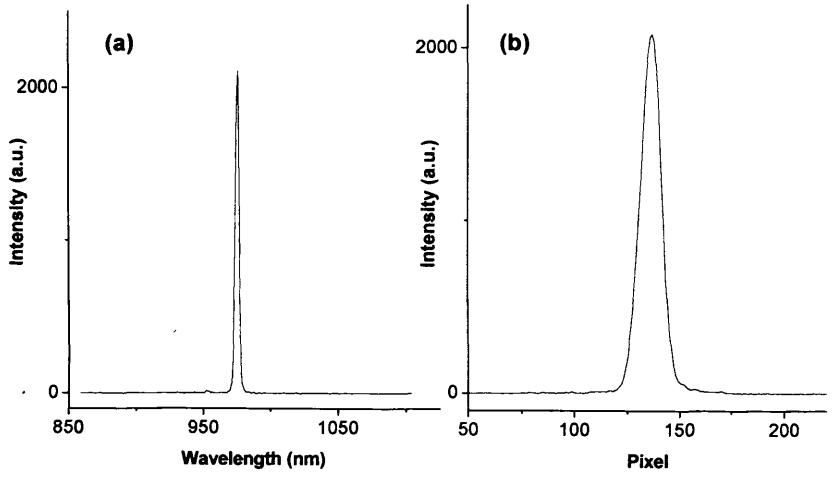

Figure 2-6. Example of the lasing spectrum (a) and lateral near-field profile (b) from a 1.5 mm-long deep-etched 5.8 μm-wide ridge waveguide quantum-well laser.

Measurement of the light-current characteristic is taken by using a fixed integration time on the camera and averaging over 5 frames for each current. Changing the integration time during the measurement will artificially change the observed light level. The recorded light level for a given current is taken by firstly subtracting the background light-level and then summing the measured signal on the camera over the entire mode. This data processing is done using MatLab. The drawback of this technique is that the light is measured in arbitrary units over the integration time. Consequently information of the light power is lost. Furthermore, changes in the integration time will affect comparison of the external differential efficiency between devices. This set-up was therefore only used in this project for determining the lasing wavelength and polarisation, and for monitoring mode changes, filamentation and wavelength changes. L-I measurements were done separately with an integrating sphere as described later on in this section.

It should be noted that before the back facet and contact breaks are etched into the GaAs+ capping layer (done to increase the inter-contact resistance and limit current spreading); it is possible to use the multisection device as a laser by connecting all five sections to the pulse generator. In this case there is no longer a passive absorber region as the entire cavity length is pumped and optical feedback occurs. As such the multisection device has the unique advantage of allowing laser measurements and ASE measurements from the same device. However, once the multisection device is fully processed into a proper multisection test-structure (i.e. increasing the inter-contact resistance to prevent current spreading, and physically smashing the back facet to stop optical feedback) the device is then no longer suitable usable for laser measurements.

The experimental set-up used for measuring the P-I characteristic with an integrating sphere is illustrated in Figure 2-7. To maintain temperature control, the laser device is again placed inside a cryostat that is fixed to a micro-positioning stage. The device is connected to a pulse generator and is driven with a duty cycle that is the same as the ASE multisection measurements. The facet of the device is aligned in front of the input port of an Ophir 3A-IS-IRG integrating sphere, which is capable of measuring the power of divergent beams with a maximum divergence of ± 40° in the wavelength

range 800 – 1700 nm. The device is aligned to obtain maximum signal. The P-I characteristic is taken by averaging the power reading over 5 seconds. An example of a P-I characteristic from a quantum-well device is shown in Figure 2-8. The threshold current density is determined by extrapolating the slope of the P-I curve above threshold to zero power.

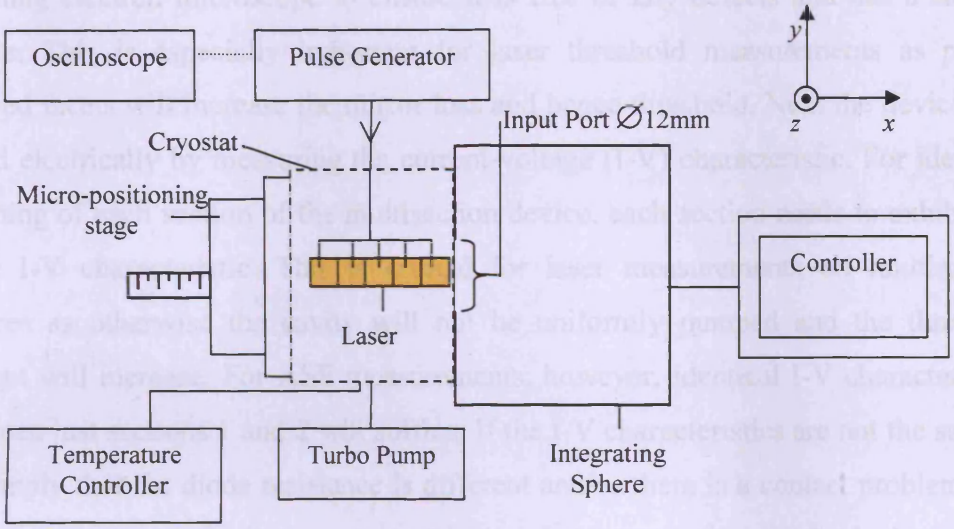

Figure 2-7. Schematic of the set-up used to measure the P-I characteristic of a laser device. Illustrated in the diagram is how a multisection device can be driven as a laser.

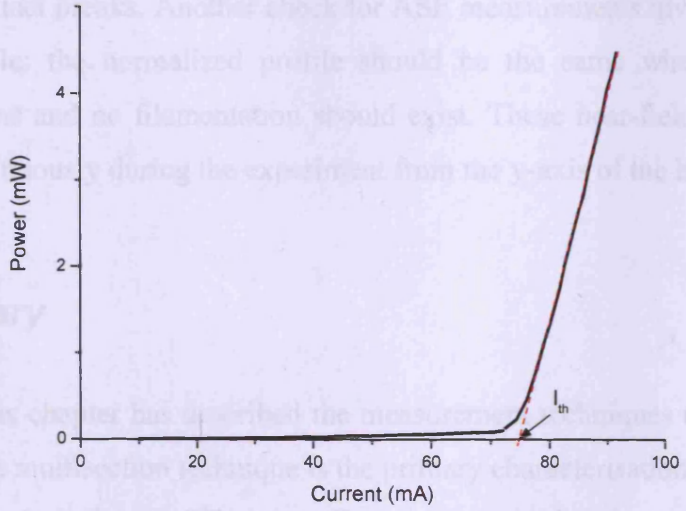

Figure 2-8. Example of a power vs. current curve for a 1.5 mm-long deep-etched 5.8 µm-wide ridge waveguide laser. The light power is calculated for emission from both facets.

2.3 Device Checks

In the experiment is it important to ensure the devices are operating correctly and are therefore able to provide accurate results. Each device is therefore subjected to certain checks before being measured. Initially the facet of each device is checked in a scanning electron microscope to ensure it is free of any defects and has a smooth cleave. This is especially important for laser threshold measurements as poorly cleaved facets will increase the mirror loss and hence threshold. Next the devices are tested electrically by measuring the current-voltage (I-V) characteristic. For identical pumping of each section of the multisection device, each section needs to exhibit the same I-V characteristic. This is critical for laser measurements on multisection devices as otherwise the cavity will not be uniformly pumped and the threshold current will increase. For ASE measurements, however, identical I-V characteristics between just sections 1 and 2 will suffice. If the I-V characteristics are not the same it can imply that the diode resistance is different and/or there is a contact problem. For ASE measurements the inter-contact resistance between sections is checked to ensure it is very high compared to the diode resistance; thereby ensuring the current leakage between sections is limited. In ridge waveguide devices, typically good inter-contact resistances of greater than 1 kΩ are achieved when the GaAs+ capping layer is etched away in the contact breaks. Another check for ASE measurements involves the lateral near-field profile: the normalized profile should be the same when pumping the different sections and no filamentation should exist. These near-field checks can be monitored continuously during the experiment from the y-axis of the InGaAs camera.

2.4 Summary

In summary, this chapter has described the measurement techniques used throughout this project. The multisection technique is the primary characterisation method used to investigate the lateral out-diffusion effect in conventional quantum-dot ridge waveguide devices, and also the performance limiting effect of surface recombination in quantum-well deep-etched ridge mesa devices. Laser threshold measurements are used to confirm the results and also to deduce the relative contributions these mechanisms have on threshold performance.

[1] J. D. Thompson, H. D. Summers, P. J. Hulyer, P. M. Smowton, and P. Blood, "Determination of single-pass optical gain and internal optical loss using a multisection device," Applied Physics Letters, 75, 17, p2527, 1999.
[2] G. M. Lewis, P. M. Smowton, J. D. Thompson, H. D. Summers, and P. Blood, "Measurements of true spontaneous emission spectra from the facet of the diode laser structure," Applied Physics Letters, 80, 1, p1, 2002.
[3] P. Blood, G. M. Lewis, P. M. Smowton, H. Summers, J. Thompson, and J. Lutti, "Characterisation of semiconductor laser gain media by the segmented contact method," IEEE Journal of Selected Topics in Quantum Electronics, 9, 5, p1275, 2003.
[4] A. Oster, G. Erbert, and H. Wenzel, "Gain spectra measurements by a variable stripe length method with current injection," Electronics Letters, 33, p864, 1997.
[5] S. Inada, M. Yoshita, M. Okano, T. Ihara, H. Akiyama, and L. Zhang, "Measurements of cavity-length-dependent internal differential quantum efficiency and internal optical loss in laser diodes," Japanese Journal of Applied Physics, 47, 4, p2288-2290, 2008.
[6] I. C. Sandall, P. M. Smowton, H-Y. Liu, and M. Hopkinson, "Nonradiative recombination in multiple layer In(Ga)As quantum-dot lasers," IEEE Journal of Quantum Electronics, 43, 5, p698, 2007.
[7] G. Tsvid, J. Kirch, L. J. Mawst, M. Kanskar, J. Cai, R. A. Arif, N. Tansu, P. M. Smowton, and P. Blood, "Spontaneous radiative efficiency and gain characterisics of strained layer InGaAs-GaAs quantum-well lasers," IEEE Journal of Quantum Electronics, 44, 8, p732, 2008.
[8] I. O'Driscoll, P. M. Smowton, P. Blood, "Low-Temperature nonthermal population of InAs/InGaAs quantum dots," IEEE Journal of Quantum Electronics, 45, 4, p380, 2009.
[9] J. Lutti, "Optical properties of InP/AlGaInP quantum dot laser heterostructures," PhD Thesis, Cardiff University 2005.

Chapter 3: Device Fabrication

3.1 Overview

This chapter outlines the procedure for fabricating ridge waveguide lasers and multisection test structures. These test-structures are designed for multisection characterisation experiments. Throughout this project the multisection technique is used to evaluate specific aspects of device performance. In Chapter 4 shallow-etched ridge waveguide (S-RWG) multisection test-structures are used to investigate and characterise the effect of lateral out-diffusion on the performance of an InAs/InGaAs quantum-dot DWELL system. In Chapter 5 deep-etched ridge waveguide (D-RWG) test-structures are used to study the performance limiting effect of surface recombination in an InGaAs quantum-well system. The significance of this quantum-well structure is that it is effectively the quantum-well part of the DWELL system. Here the terms shallow-etched and deep-etched are used to describe a ridge etch depth being at the interface between the upper-cladding and waveguide region, and an etch depth 200nm below the waveguide region, respectively.

In the subsections of this chapter aspects of the key fabrication steps, like electron beam lithography, dry-etching, and insulation/planarisation will be described. In addition processing issues will be raised and brief discussions of the development work will be given.

3.2 S-RWG and D-RWG Multisection Test Structures

Illustrated in Figure 3-1 is the basic design of the ridge waveguide (RWG) multisection test-structure. The RWG is fabricated using Ar/Cl_2 inductively coupled plasma dry etching and is planarised and electrically insulated using Benzocyclobutene (BCB). The p- and n- type contacts are AuZn and AuGe/Ni/Au respectively. The contacts are segmented into 300 μm long sections and are electrically isolated from each other. Each segment is individually wired and can be separately pumped. The basic process-flow for creating the structure is given in Figure 3-2. The main aspects of the process-flow are discussed in the sub-sections.

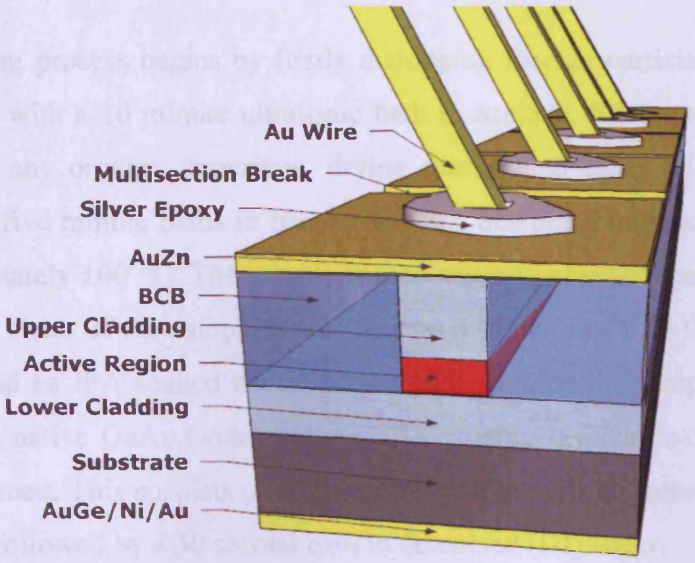

Figure 3-1. Illustration of a deep-etched ridge multisection test-structure.

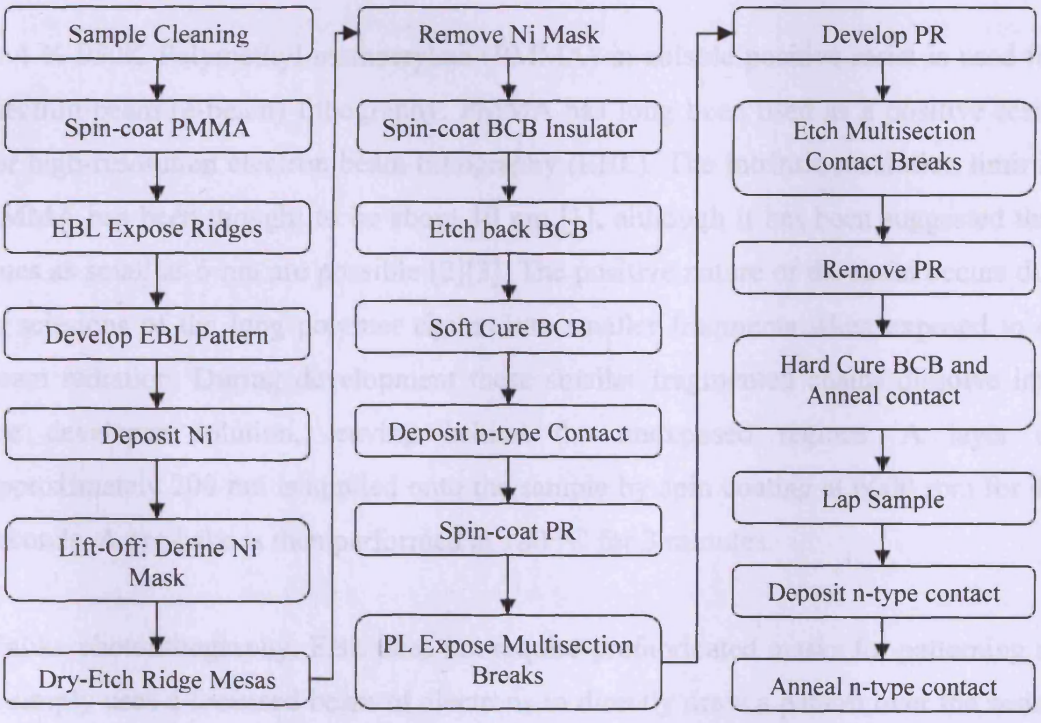

Figure 3-2. Process-flow for ridge waveguide multisection test-structures.

3.2.1 Sample Cleaning

The cleaning process begins by firstly dislodging foreign particles on the surface of the sample with a 10 minute ultrasonic bath in acetone. Subsequently the surface is cleaned of any organic impurities, drying marks, and other thin film residues by successive five minute baths in trichloroethene, acetone, methanol, and isopropanol, at approximately 100 °C. The sample is then visually checked using a microscope to ensure it is clean. If the sample is still observed to be dirty then the whole process is repeated and an IPA soaked cotton bud is used to wipe the sample if necessary. To remove the native GaAs oxide on the GaAs capping layer a de-oxidation process is then performed. This consists of a 30 second bath in a dilute ammonia (NH_3) solution (5% NH_3) followed by a 30 second bath in deionised (DI) water.

3.2.2 Electron Beam Lithography

A 4 % 950K Polymethyl-methacrylate (PMMA) in anisole positive resist is used for electron-beam (e-beam) lithography. PMMA has long been used as a positive resist for high-resolution electron beam lithography (EBL). The intrinsic resolution limit in PMMA has been thought to be about 10 nm [1], although it has been suggested that lines as small as 6 nm are possible [2][3]. The positive nature of the resist occurs due to scissions of the long polymer chains into smaller fragments when exposed to e-beam radiation. During development these smaller fragmented chains dissolve into the developer solution, leaving behind the unexposed regions. A layer of approximately 200 nm is applied onto the sample by spin coating at 6000 rpm for 45 seconds. A pre-bake is then performed at 180 °C for 3 minutes.

Unlike photolithography, EBL does not require prefabricated masks for patterning as it simply uses a focussed beam of electrons to directly draw a pattern over the resist. However this 'serial' pattern generation process is very time consuming compared to the parallel nature of photolithography. EBL offers higher resolution patterning than standard ultraviolet photolithography (sub 100 nm compared to micrometer resolution). With high resolution patterning, lithographic imperfections are reduced and consequently smoother sidewall profiles are achieved. This is important for

reducing sidewall scattering in RWG devices [4]. Another benefit of EBL is the large depth of focus. This is illustrated in Figure 3-3 where the large depth of focus has allowed 200 nm lines and holes to be written over a 2.5 μm deep mesa without a significant loss in resolution. Such patterning would not be possible with photolithography.

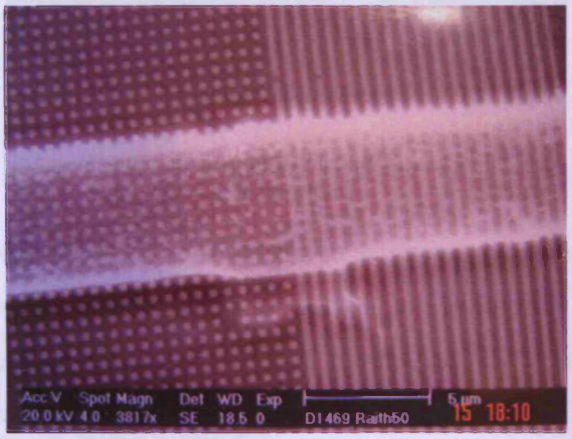

Figure 3-3. An SEM image of 200 nm lines and holes exposed over a 2.5 μm deep mesa using our RAITH50 EBL system.

In general an EBL system consists of: an electron source; an electron column that accelerates, shapes, focuses, deflects and blanks the electron beam; a mechanical x-y-z stage that positions the wafer under the electron beam; and a computer that controls the alignment and pattern generation process. The system used in this work was a RAITH-50 with a LaB_6 electron source. The system is capable of beam acceleration voltages of 200 eV – 30 keV. In this work the acceleration voltage was typically 20 keV; higher acceleration voltages were generally used for patterning sub 100 nm features, minimising proximity effects, and/or increasing the beam current. The system has a laser interferometer stage with 2 nm resolution allowing multilevel lithography. A minimum linewidth of 50 nm is quoted from the manufacturer but generally this is hard to achieve due to resolution limiting mechanisms. However, I have managed to get the system to produce linewidths of approximately 65 nm, as illustrated in Figure 3-4.

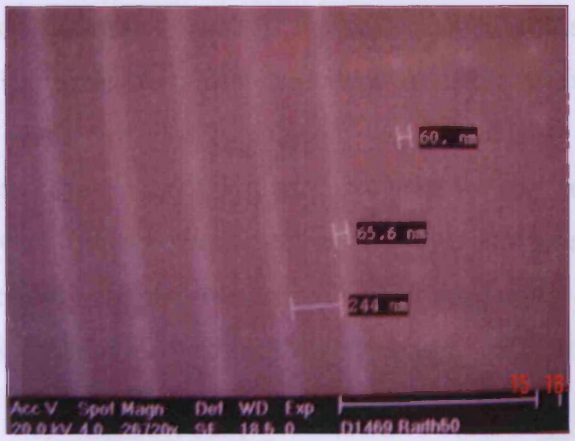

Figure 3-4. An SEM image of ~65 nm lines and holes exposed in PMMA using our RAITH50 EBL system.

In the RAITH-50, design patterns are written in segments called write-fields (WF). In a WF exposure the stage is stationary and patterns are written by vector scanning the position of beam over an exposure grid that covers the WF area. Smaller WF sizes have smaller grid spacing and hence smaller step size resolution. The design pattern is formed by moving the stage to correctly stitch neighbouring WF exposures together. Stitching errors can arise by random jumps between shapes due to insufficient settling times, hysteresis, and beam drift [5]. The latter effect also causes pattern variations due to changes in the beam current and hence exposure dose. To avoid beam drift the exposure time should be kept as low as possible and the environment temperature and humidity should be well controlled. In this fabrication process we mainly desire well defined edges and good stitching results. To achieve well defined edges requires: a small WF, good focus, and small step size. Good stitching requires: small write fields for greater placement accuracy, low beam drift, and very good WF alignment (e.g. zoom corrections between 0.9999 – 1.0001). The problem with reducing the WF size is that it increases the stage movement and hence overall exposure time. Longer exposure times are more likely to experience significant beam drift. In this fabrication process a 100 μm WF size was empirically found to give the best lithography results (i.e. negligible stitching errors and smooth edges).

In EBL the resolution is mainly limited by the scattering of the electron beam in the resist and substrate. These scattered electrons are low in energy and can be classed as either forward (in the direction of the original beam) or back scattered secondary electrons. Scattering has two major effects: patterned features are broadened in

diameter as the beam penetrates through the resist; and the resist gets unintended additional exposure from electrons scattered back from the semiconductor material. This latter affect leads to closely placed features being overexposed from neighbouring features, thereby creating patterns which are bigger than intended. The phenomenon is known as the proximity effect and it is counteracted by grading the exposure dose in closely spaced features. In this fabrication process, proximity corrections to the exposure dose were not required as ridge features were placed far apart.

In the EBL pattern the ridges are separated by a 300 μm pitch and are batched together in groups of varying ridge widths (typically ranging from 1 to 30 μm). Distributing different ridge widths across the whole sample like this ensured a good yield of each different ridge width. Had they been put into groups of the same width then localised processing errors, like large dust particles or edge beads, would have decreased the yield from a particular width.

After exposure the EBL pattern was developed in a 1:3 solution of methyl isobutyl ketone (MIBK) to isopropanol (IPA) for 30 seconds. This was followed by a 30 second rinse in IPA and a N_2 blow dry.

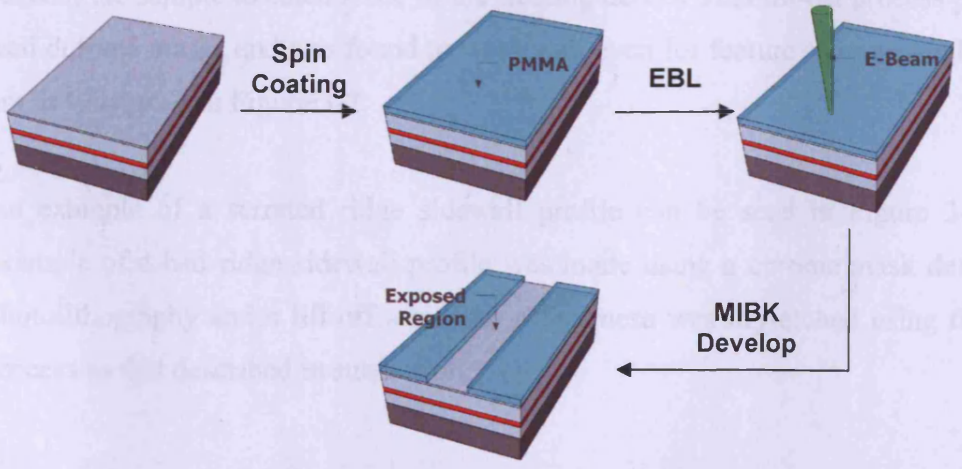

Figure 3-5. Illustration of EBL procedures

3.2.3 Lift-Off

The transfer of the EBL pattern into the semiconductor material is achieved by inductively coupled plasma (ICP) etching. Since PMMA itself is not hard enough to act as a mask for ICP pattern transfer deep into the semiconductor material, it was necessary to transfer the patterned PMMA template into a material which was. This was achieved by a lift-off process. During the development, SiO_2, Cr, and Ni were all empirically tested as masks. From this work the best mask was found to be Ni. It provided enough etch resistance for deep-etching into semiconductor material; it could easily be removed; and it generally lifted-off without serrating the edges. To form the mask, Ni was deposited onto the patterned PMMA template in an Edwards thermal evaporator at a rate of 0.1 nm min^{-1} to a thickness of 70 nm. A lift-off process was then followed to remove the unwanted PMMA and Ni, leaving behind a patterned layer of Ni in the form of the original EBL pattern. This required immersing the sample into a bath of hot acetone (100 °C) and gently shaking it until the PMMA dissolved and concomitantly the Ni lifted-off. The process is illustrated in Figure 3-6. During the lift-off process it was important to ensure the lifted-off Ni did not redeposit back onto the sample because it adhered extremely well to the surface and could not be removed by further acetone baths or even ultrasonic agitation. To reduce the amount of Ni debris floating around in the acetone bath, filter paper was placed beneath the sample to catch some of the floating debris. This lift-off process provided well defined masks and was found to work well even for feature sizes as small as 200 nm as illustrated in Figure 3-7.

An example of a serrated ridge sidewall profile can be seen in Figure 3-8. This example of a bad ridge sidewall profile was made using a chrome mask defined by photolithography and a lift-off step. The ridge mesa was dry-etched using the same process as that described in subsection 3.2.4.

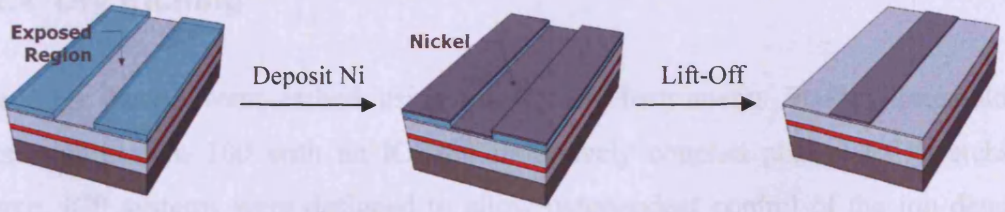

Figure 3-6. Illustration of the lift-off process.

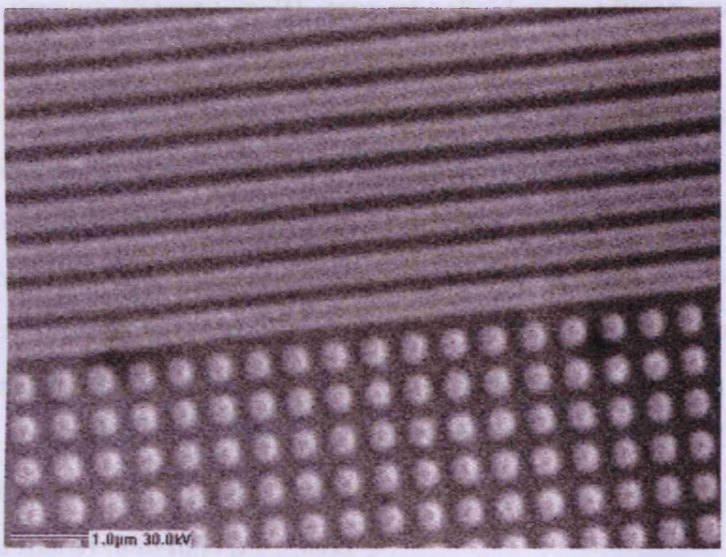

Figure 3-7. An SEM image of 200 nm Nickel mask lines and holes formed by the lift-off process.

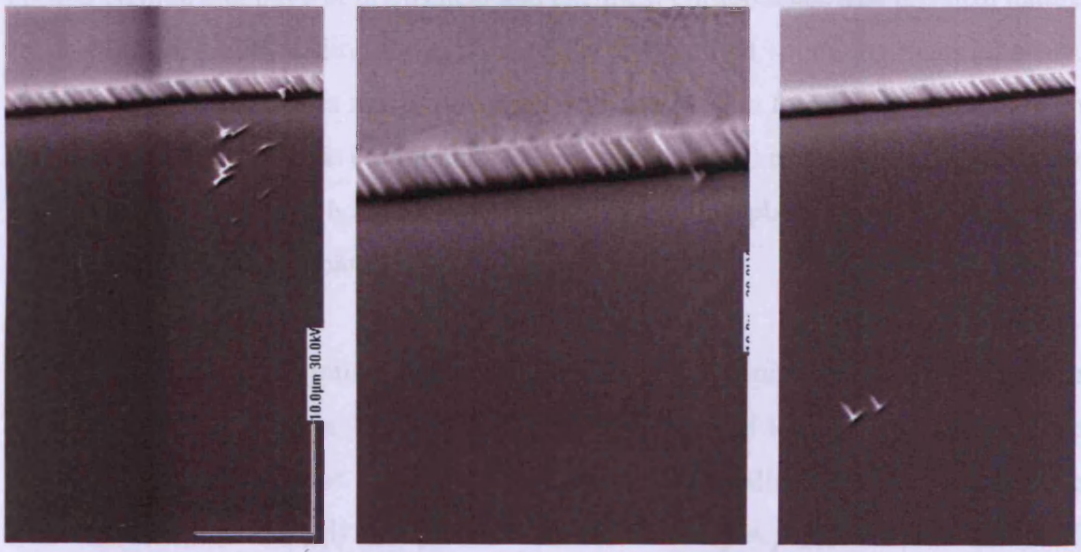

Figure 3-8. SEM images of a serrated ridge sidewall profile. The ridge sample was processed using a Cr mask defined by photolithography and lift-off. The ridge mesa was defined by ICP dry-etching as described in subsection 3.2.4

3.2.4 Dry Etching

The ridge mesas were etched using an Oxford Instruments Plasma Technology Plasmalab system 100 with an ICP380 inductively coupled plasma (ICP) etching source. ICP systems were designed to allow independent control of the ion density and ion energy. In cylindrical ICP etching systems, such as this one, an inductive coil surrounds a dielectric vacuum chamber in which the plasma is contained. When an RF current flows through the coil, a RF magnetic field is produced and this in turn induces a RF electric field inside the chamber. Electrons in the chamber are accelerated by this electric field and a dense plasma is created by these accelerating electrons [6]. Increasing the ICP RF power increases the density of ions in the plasma. For separate control of the ion energy impinging on the sample, the system also has a separately controlled RIE configuration whereupon the sample sits on an electrode. The electrodes of the RIE component capacitively couple to the plasma. Increasing the RIE power increases the energy of the ions impacting the sample surface. This description is a somewhat simplified but sufficient description of the ICP system. A more detailed description of ICP systems in general can be found in [6] and specifically for this system in [7].

Plasma etching can have both physical and chemical components. The physical nature arises from ions bombarding the surface of the sample and sputtering material away. Chemical etching involves reactive species from the plasma forming compounds with the surface material. These compounds either leave the surface by their own accord or are removed by physical bombardment. Most dry etching plasma processes require a combination of both mechanisms.

By empirically investigating different process gas chemistries (from a possible combination of Ar, Cl_2, and BCl_3), stage temperatures, and RIE and ICP powers, the best plasma conditions for etching smooth vertical sidewalls in GaAs/AlGaAs were found. Development of this etch process was new to the group and was principally led by Angela Sobiesierski who is a postdoctoral researcher at Cardiff University. The best process conditions were: a 9:1 Ar to Cl_2 gas chemistry, stage temperature of 25 °C, RIE power of 50 W, ICP power of 300 W and a chamber pressure of 10 mTorr. The Ar ions in the plasma provided a physical etch mechanism and the Cl_2 a chemical

mechanism. This balance of two etch mechanisms gave the best vertical etching. Deviating from this balance in favour of more Cl_2 ions made etching more isotropic and consequently undercut the ridge profile. Adding a higher Ar concentration maintained vertical etching but made the surface and sidewalls very rough. An example of the etch profile achieved by the optimised process can be seen in Figure 3-9 and Figure 3-10.

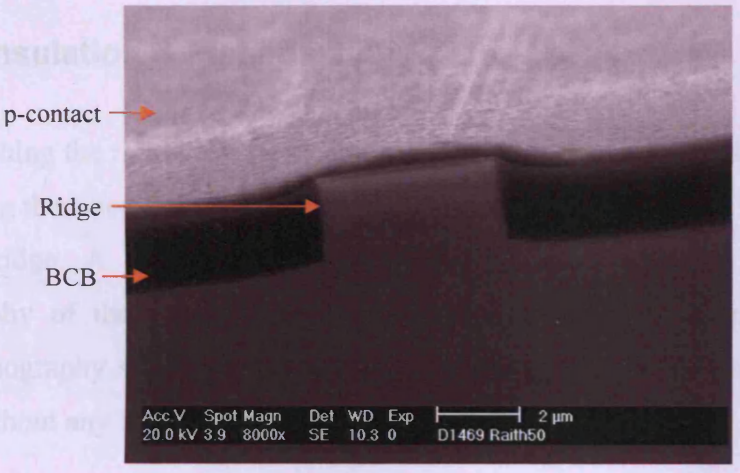

Figure 3-9. An SEM image of a metallized and insulated RWG device and underlying etched profile.

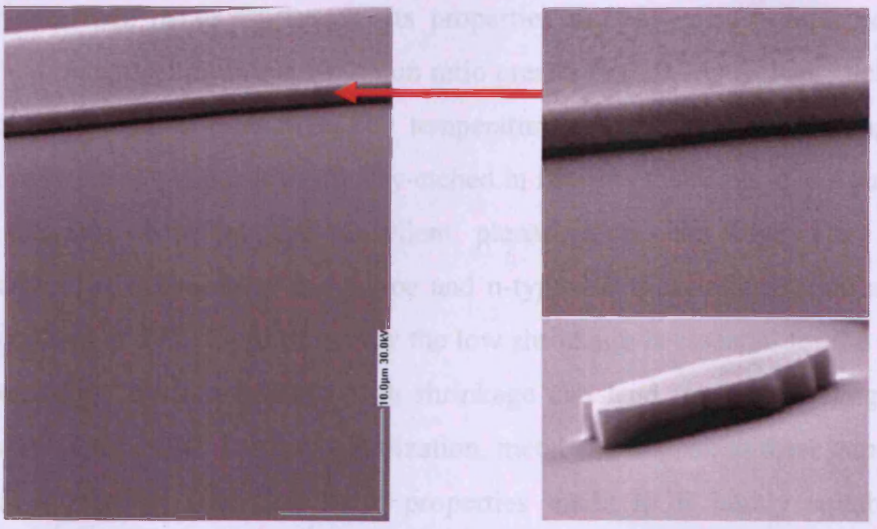

Figure 3-10. SEM images of a good ridge sidewall profile achieved by ICP dry-etching using a 9:1 Ar to Cl_2 gas chemistry at 25 °C, on a sample with a Ni mask defined by e-beam lithography and lift-off.

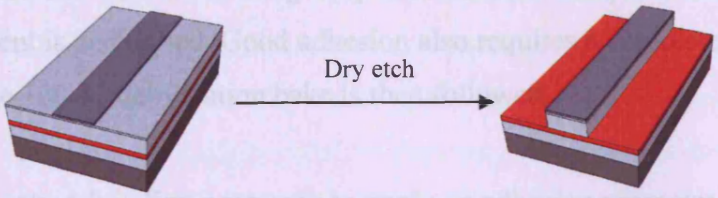

Figure 3-11. Dry-etch illustration for a shallow-etched ridge

3.2.5 Insulation & Planarisation

After etching the ridges an electrical insulation layer is required in the etched regions. Insulating these regions ensures the only current path is through the top p-type contact of the ridge. A secondary purpose of the insulation layer is to planarize the topography of the surface. This then provides a flat focal plane for subsequent photolithography steps and allows large contacts pads to be deposited on top of the ridge without any breaks.

The material used for insulating the etched regions was benzocyclobutene (BCB). BCB is a spin-on dielectric polymer which is commercialised by Dow Chemical under the trade name Cyclotene. Its properties include: a low-dielectric constant; excellent planarisation (a planarization ratio greater than 0.9 is typically achieved in a single coat), a high glass transition temperature (>350 °C), low shrinkage (< 5 % when fully cured), and it is easily dry-etched in fluorine based plasma. Apart from the low dielectric constant and excellent planarization, the high glass transition temperature is desirable as the p-type and n-type electrical contacts are annealed at temperatures of 370 °C. Additionally the low shrinkage is essential for the fabrication of these ridge devices because high shrinkage can lead to gaps forming along the sidewalls of the ridge. During metallization, metal can deposit in these gaps and short the p-i-n junction. Together these properties made BCB highly suitable for the fabrication process of RWG multisection test-structures.

For defect free coating and good adhesion between the BCB and sample it is necessary to remove any contaminants (organic or inorganic) from the surface of the semiconductor sample. Spin-on polymers tend to pull away from contaminated areas

leaving pinholes and uneven coverage [8]. To clean the sample a 2 minute oxygen plasma treatment is performed. Good adhesion also requires a completely dry surface, thus a 2 minute 100 °C dehydration bake is then followed.

Before BCB coating it is first necessary to apply an adhesion promoter to the surface. An adhesion promoter provides good interfacial adhesion by acting as a coupling agent between the BCB resin and semiconductor surface [9]. The adhesion promoter Dow AP3000 is applied to the sample by puddle dispensing it onto the whole sample and then spin-coating at 3000 rpm for 30 seconds to form a uniform film. Following this, BCB resin is immediately puddle dispensed onto the sample and spin-coated at 3000 rpm for 30 seconds to form a film thickness of approximately 3 μm. The BCB film is next baked on a hot plate at 100 °C for 2 minutes to remove solvents and stabilise the film. This prevents it from flowing during subsequent handling and processing steps. At this point the quality of the film is checked through a microscope to ensure it is mostly uniform (apart from edge beads), and free of dispensing bubbles, striations, and pinholes. Since the morphology of the cured BCB film – and hence back-etching profile – will be influenced by any such defects, poor quality films are removed (using DOW T1100 BCB) and reapplied.

BCB is cured by thermal polymerisation at temperatures above 200 °C [10]. No catalysts are required, and except for early out-gassing of residual solvent (between temperatures of approximately 30 – 150 °C [10]) the curing process produces no other volatile by-products [11]. To prevent oxidation of the BCB film, which may negatively influence the insulating and dielectric properties, the BCB film was cured in a nitrogen (N_2) atmosphere. The first stage of the curing process was to soft-cure the BCB film to 75 – 82 % complete polymerisation. Soft cured BCB was found to be easier to etch and also found to provide better adhesion to the Au/Zn metallization. The process was done by slowly ramping up the temperature from room temperature to 210 °C at a rate of 5 °C/minute and holding at 210 °C for 40 minutes. Slowly ramping up the temperature was found to produce better planarization and also prevent bubbles from degassing effects.

After the soft-cure bake, the BCB was then dry etched back in the ICP. An etch recipe of 3:1 O_2 to C_4F_8 with 75 W RIE power, 1500 W ICP power, and a table temperature

of 20 °C was empirically found to give a well controlled and uniform etch. Etching was stopped just after the top of the ridges are exposed and free of BCB. Since the etch rate was found to vary according to the age of the BCB it was necessary to etch the BCB in stages and continually monitor the progress with a microscope. As the BCB layer on top of the ridges got thinner, thin film fringes were observed. When these fringes eventually disappeared to reveal the shiny grey GaAs ridge top, the top of the ridges were free of BCB. To confirm this, SEM measurements were also taken to ensure the ridge top was indeed exposed. An illustration of the BCB coating process is given in Figure 3-12.

Having insulated and planarised the regions between the ridges, metallization of the p-type contact then followed. Details of the metallisation process can be found in the subsection titled metallisation.

The final hard-cure of the BCB (100% polymerisation) was done after the p-type contact metallisation and multisection patterning (described in the next section). First the temperature was ramped up slowly from room temperature to 300 °C at a rate of 10 °C/minute and then held at 300 °C for 1 hour. The faster ramp up rate is permitted because the BCB film has already been 75 – 82 % cured. Following the 1 hour BCB hard cure, the temperature of the sample was ramped up to 370 °C for 3 minutes to anneal the p-type contact with the GaAs ridge top. Since this is above the glass transition temperature of BCB (T_g > 350 °C), the mechanical structure of the BCB film is expected to degrade slightly. However the study by [10] shows the weight should only decrease by < 1 %/min at 370 °C; therefore the degradation should not be very significant. Indeed observations of the BCB film after annealing showed no cracks or significant shrinkage; the sides of the ridges and the regions between the ridges were still covered with BCB.

Before BCB became available, a number of alternative insulation and planarization techniques were investigated using existing materials and processes. These included depositing a silicon dioxide (SiO_2) dielectric layer; planarizing and coating the sidewalls with PMMA; and using anodic oxide to insulate the sidewalls. Of these alternative techniques, only the SiO_2 method produced working devices. Briefly: SiO_2 was deposited onto the sample by thermal electron beam evaporation. Complete

coverage of the surface topography proved difficult especially for deep etched ridges. The poor coverage of the sidewall resulted in the p-n junction shorting after metallization. To improve sidewall coverage and planarization the sample stage was placed at an angle to the SiO_2 flux source and rotated during the deposition process. This improved coverage of the sidewall but the layer was thin and non-conformal. By using SiO_2 to insulate the sidewalls subsequent processing steps were required to open up the tops of the ridges for contacting. Lifting-off the SiO_2 on the tops of the ridges by etching the Ni mask did not work because of the thick SiO_2 coverage. The solution found was to lithographically pattern contact windows and then etch the SiO_2 with HF acid. This required using the EBL to accurately overlay a contact window pattern over the existing surface topography; which proved difficult and time consuming mainly because of the system conditions. This technique worked well for ridge widths approximately greater than 4 μm but not so for narrow ridge widths. In narrow ridge widths the contact windows could not be as accurately placed on the ridge tops and moreover the HF etching of the SiO_2 increasingly acted on the sides of the ridge.

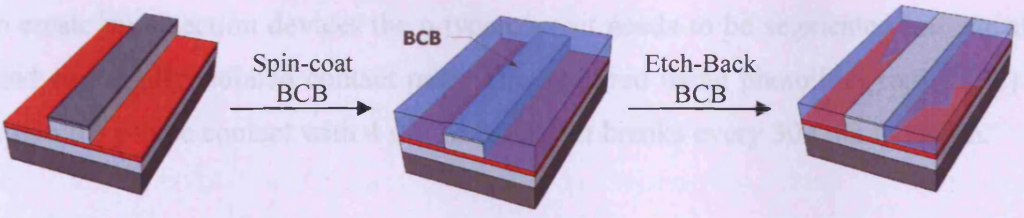

Figure 3-12. BCB process

3.2.6 Metallisation

Metals were deposited on the semiconductor and/or dielectric surface in an Edwards thermal evaporator. In a thermal evaporator a metal source is held in a resistive heater called a boat under high vacuum conditions (~10^{-6} mBarr). When the boat is heated to a high enough temperature the metal source melts and starts evaporating. Consequently high temperature metallic atoms travel through the vacuum until they impinge and condense on the sample. Over time a film of the metal source accumulates on the surface of the sample with a very conformal profile.

In GaAs systems Schottky barriers are generally formed between the GaAs layer and metal film. To counteract this, multiple metal layers are used to auto dope the surface. For p-type GaAs, a layer sequence of 10 nm Zn and 300nm Au was deposited. For n-type GaAs, a layer sequence of 100 nm AuGe, 28 nm Ni, 300 nm Au was used. The metals were typically deposited at a rate of 0.15 nm/min. These contact layers are well known to give good Ohmic contacts.

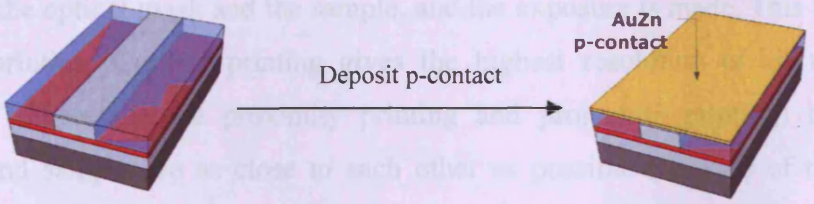

Figure 3-13. p-type metallization

3.2.7 Multisection Patterning

To create multisection devices the p-type contact needs to be segmented into equally sized electrically isolated contact pads. This required using photolithography (PL) to pattern the p-type contact with 4 μm wide contact breaks every 300 μm in length.

In PL a predefined pattern on an optical mask is transferred to a photosensitive resist (PR) using ultraviolet light (UV). The PR can be classified as either positive or negative depending on whether it becomes more or less soluble after UV exposure. Here we use the positive PR, Shipley Microposit S1813 SP15. When exposed to UV radiation, a positive PR undergoes photo activated chemical changes which cause it to become more soluble in the developer solution. The benefits of positive PR include sharper resolution then its negative counterpart and the lack of swelling during development. They can also be used in much thicker coatings (1-3μm) than negative PR. As a result, they are more resistant to chemical etches, and are more reliable in problem areas such as steps, which leads to resist thinning. Unexposed PR can easily be removed by hot acetone.

Optical masks are patterned plates with opaque and transparent regions relating to the desired pattern to be imprinted on the PR. Exposure onto a positive PR will pattern a direct copy of the mask pattern. In manual systems such as the one in the lab (Karl Suss Hg-Lamp), an optical mask is placed over the sample and is brought into contact with it, and is then backed off slightly to produce an air gap. Next the sample is positioned into alignment by micrometer adjustments. This alignment process is performed with the aid of a microscope. Finally, physical contact is re-established between the optical mask and the sample, and the exposure is made. This is known as contact printing. Contact printing gives the highest resolution of all the printing methods (others include proximity printing and projection printing) because the pattern and sample are as close to each other as possible (because of this only 1x masks are used). When in contact, a flood exposure of UV light shines through the transparent regions of the optical mask and onto the PR. Developing the PR then washes away the exposed regions, leaving behind a direct copy of the mask pattern.

The first stage of the PL procedure was to spin-coat the Shipley Microposit S1813 SP15 at 6000 rpm for 45 seconds to give a PR coating of approximately 1.3 μm in thickness. The PR was then soft baked at 97 °C for 3 minutes to evaporate off the solvents and harden it, thereby making it more resistant for subsequent processing steps and less soluble in the developer solution. Spin-coating films inevitably bring about edge beads that are several times the thickness of the central film. In order to achieve good close contact during exposure, and hence good resolution, it was necessary to remove these edge beads by exposing them to a high dose of UV radiation and then dissolving them away in the developer. After this an optical mask pattern consisting of 4 μm wide channels separated by a 300 μm pitch was aligned perpendicular to the ridges and exposed for 6 seconds. The pattern was then developed for 15 seconds in a 1:3 solution of Shipley Microposit 2401 to deionised water. The next step of the lithographic process was to hard bake the patterned PR at 97 °C for 3 minutes. Hard baking was necessary in order to improve interfacial adhesion and harden the PR.

After patterning the PR with 4 μm wide channels the next stage was to transfer this pattern into the p-side AuZn contact and form segmented contact pads. This was achieved by using the PR as a mask and wet etching the AuZn in the exposed 4 μm

breaks. The PR was then removed with a bath of acetone, followed by a rinse in IPA. This patterning process is illustrated in Figure 3-14.

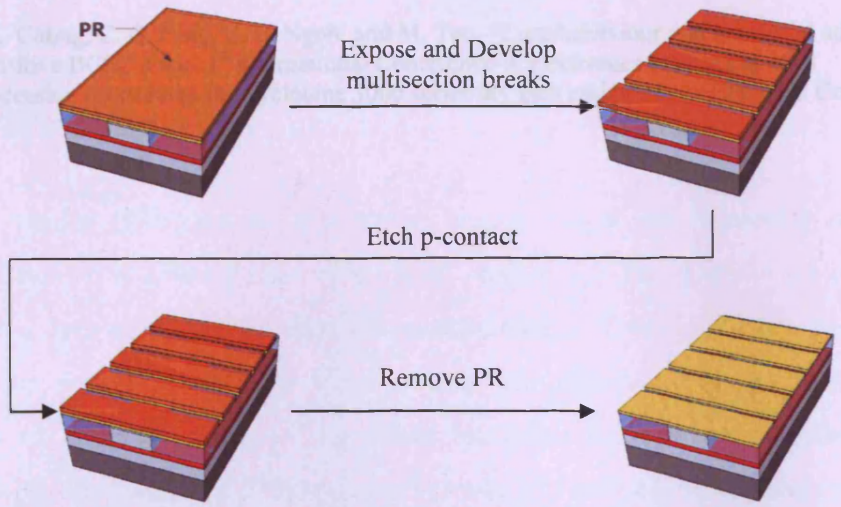

Figure 3-14. Process for patterning multisection contact breaks

3.2.8 Summary

In this chapter the fabrication procedures for making ridge waveguide lasers and multisection test-structures have been outlined. Aspects of key fabrication steps have been described in detail along with brief discussions of certain development issues. These included optimising the EBL process and etch protocol for fabricating vertical ridges, as well as a technique for insulating and planarizing the sidewalls and surface topography. Ridge waveguide test-structures are used throughout the investigations of this project to analyse various aspects of device performance by using the multisection characterisation technique.

[1] H. G. Craighead, R. E. Howard, L. D. Jackel, and P. M. Mankeiwich, "10-nm linewidth electron beam lithography on GaAs," Applied Physics Letters, 42, 38, 1983.
[2] W. Chen, H Ahmed, "Fabrication of sub-10 nm structures by lift-off and by etching after electron-beam, exposure of poly(methylmethacrylate) resist on solid substrates," Journal of Vacuum Science and Technology B, 11, 2519, 1993
[3] M. Khoury, D. K. Ferry, "Effect of molecular weight on poly(methylmethacrylate) resolution," Journal of Vacuum Science and Technology B, 14, 75, 1996
[4] C. G. Poulten, C. Koos, M. Fujii, A Pfrang, T. Schimmel, J. Leuthrod, W. Freude, "Radiation modes and roughness loss in high-index contrast waveguides," IEEE Journal of selected topics in quantum electronics, 12, 6, p 1306, 2006
[5] RAITH Lithography Course Notes September 2002
[6] M. Sugawara, "Plasma etching: fundamentals and applications," Oxford University Press, 1998

breaks. The PR was then removed with a bath of acetone, followed by a rinse in IPA. This patterning process is illustrated in Figure 3-14.

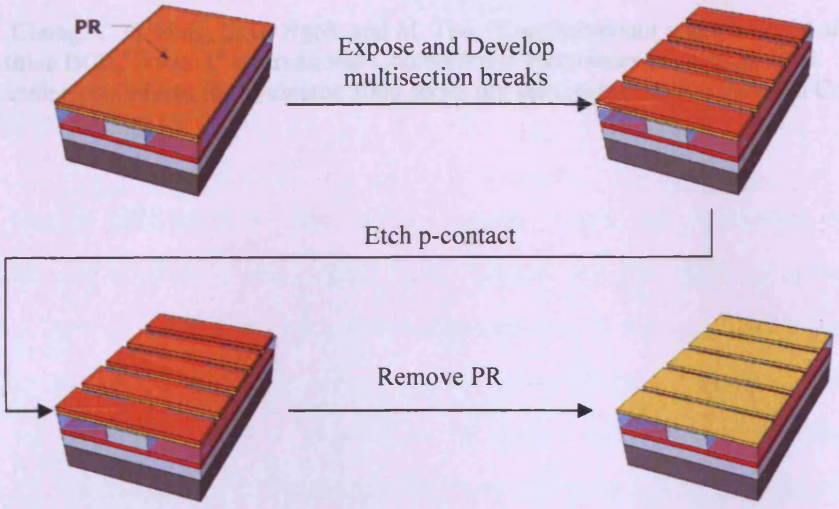

Figure 3-14. Process for patterning multisection contact breaks

3.2.8 Summary

In this chapter the fabrication procedures for making ridge waveguide lasers and multisection test-structures have been outlined. Aspects of key fabrication steps have been described in detail along with brief discussions of certain development issues. These included optimising the EBL process and etch protocol for fabricating vertical ridges, as well as a technique for insulating and planarizing the sidewalls and surface topography. Ridge waveguide test-structures are used throughout the investigations of this project to analyse various aspects of device performance by using the multisection characterisation technique.

[1] H. G. Craighead, R. E. Howard, L. D. Jackel, and P. M. Mankeiwich, "10-nm linewidth electron beam lithography on GaAs," Applied Physics Letters, 42, 38, 1983.
[2] W. Chen, H Ahmed, "Fabrication of sub-10 nm structures by lift-off and by etching after electron-beam, exposure of poly(methylmethacrylate) resist on solid substrates," Journal of Vacuum Science and Technology B, 11, 2519, 1993
[3] M. Khoury, D. K. Ferry, "Effect of molecular weight on poly(methylmethacrylate) resolution," Journal of Vacuum Science and Technology B, 14, 75, 1996
[4] C. G. Poulten, C. Koos, M. Fujii, A Pfrang, T. Schimmel, J. Leuthrod, W. Freude, "Radiation modes and roughness loss in high-index contrast waveguides," IEEE Journal of selected topics in quantum electronics, 12, 6, p 1306, 2006
[5] RAITH Lithography Course Notes September 2002
[6] M. Sugawara, "Plasma etching: fundamentals and applications," Oxford University Press, 1998

[7] G. T. Edwards, "The fabrication of deep-etched distributed Bragg reflectors in AlGaInP/GaAs laser structures," PhD Thesis, Cardiff University, 2007.
[8] M. K. Ghosh, K. L. Mittal, "Polyimides", CRC, edition 1, 1996
[9] P. Garrou, "Polymer Dielectrics for Multichip Module Packaging," Proceedings of the IEEE, 80, 12, 1992
[10] C. K. Chong, C. C. Peng, L. G. Ngoh, and M. Teo, "Cure behaviour and interfacial adhesion of photo-sensitive BCB," Proc. 1st International Conference in electronics Packaging, 2001
[11] "Processing procedures for Cyclotene 3000 series dry etch resins", Dow Chemical Company

Chapter 4: Lateral Carrier Out-Diffusion in InAs/InGaAs Quantum-Dot DWELL Shallow-Etched Ridges

4.1 Introduction

Lateral carrier diffusion in the active region plays an important role in the performance of shallow-etched ridge laser diodes. As the ridge is scaled down in width, the current associated with the recombination of carriers which have diffused out of the region beneath the ridge (lateral out-diffusion current), increases as a fraction of the total current. The effect increases the apparent threshold current density (J_d), decreases the differential efficiency and possibly affects the mode control. In the literature, the effects of lateral out-diffusion on the J_{th}-W characteristic have been accounted for by modelling the lateral carrier density profile using analytical solutions of the ambipolar diffusion equation [1-5, 16-19].

In the introduction, several studies were mentioned to have estimated the lateral ambipolar diffusion length in ridge waveguide devices by fitting the threshold current dependence on the ridge width. By fitting a model to real laser threshold data these studies offer the advantage of determining L_d under high-level injection conditions. This is preferred for the understanding and optimisation of the diffusion process under proper working conditions. However, these reports have relied on specific laser models and sets of assumptions to characterise unknown material characteristics such as the gain, optical mode, and recombination mechanisms. Moreover other key mechanisms which can potentially affect the threshold and hence fitting of the data – such as an increasing internal optical loss [7, 8] and deteriorating gain-mode overlap [13 - 15] – are not all taken into consideration. This is a potential shortcoming of any model that is fitted to real laser threshold data.

In this chapter I present a study which uses the multisection technique on shallow-etched ridge waveguide devices of various widths to characterise the effects of lateral out-diffusion on the performance of a quantum-dot material system. To gain a more complete and further understanding of the processes and resulting effects, I determine

the lateral ambipolar diffusion length by firstly characterising the changes in modal gain, internal optical loss, radiative and non-radiative recombination processes, and overall internal quantum efficiency as a function of ridge width and threshold condition. By this approach I am able to circumvent the problems of previous techniques by:

- separately evaluating the effects of internal optical loss, gain-mode overlap, and lateral out-diffusion on the threshold current characteristic with ridge width
- experimentally measuring parameters and under high-injection level conditions
- and by fitting a standard diffusion length model to data that is only affected by the lateral out-diffusion effect

An additional benefit of this approach is that all of the characteristics can be evaluated as a function of injection-level (i.e. threshold condition).

The mechanism of lateral carrier diffusion in S-K quantum-dot systems is still uncertain due to the coupled transport between the dots, wetting layer and barrier material. To further understand the lateral diffusion process, I also analyse the lateral ambipolar diffusion length as a function of carrier injection-level. By doing so I illustrate that the lateral ambipolar diffusion length is a strong function of Fermi-level separation i.e. population of higher energy states in the quantum-dot and wetting-layer. The observed dependence is an original result and highlights that recombination in either the 2-dimensional wetting layer or surrounding barrier structure can proceed to affect the ambipolar diffusion length with further carrier injection.

The chapter is split into two distinct parts. Part one presents the measured characteristics from which the key mechanisms involved in the J_{th}-W characteristic are analysed. The second part describes a lateral ambipolar diffusion model that is used to fit the data involving lateral out-diffusion. This model is then applied to the measured data at various carrier injection-levels to determine L_d as a function of carrier injection-level.

4.2 QD Material Details

The QD material used in this work has been optimised for 1.3μm operation and was grown by solid source molecular beam epitaxy at Sheffield University. The active region consisted of 5 Dot-in-a-Well (DWELL) repeats, where each DWELL was made up of 3.0 monolayers of InAs grown on 2 nm of $In_{0.15}Ga_{0.85}As$ and then capped by a further 6 nm of $In_{0.15}Ga_{0.85}As$, and these were then separated by 50 nm high growth temperature GaAs spacers. Figure 4-1 illustrates the DWELL repeat. The active region was incorporated into a GaAs-$Al_{0.4}Ga_{0.6}As$ waveguide structure. The entire layer structure is given in Table 1.

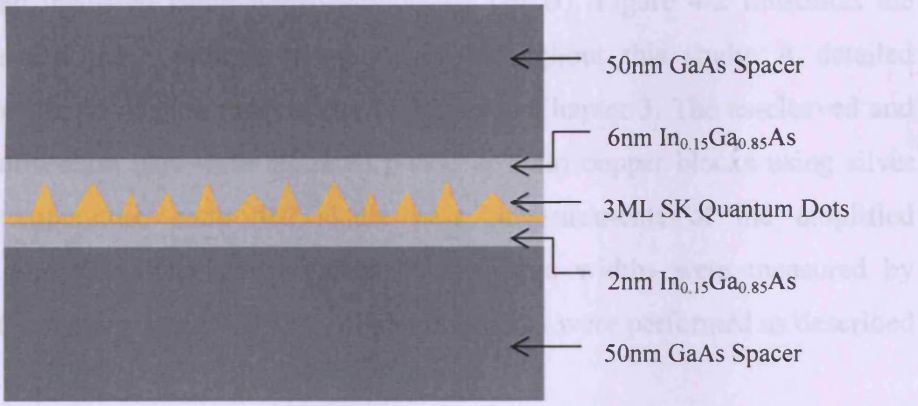

Figure 4-1. DWELL material structure used in this study.

Material	Thickness (A)	Repeats	Dopant	Concentration (cm^{-3})
p-GaAs	3000	1	Berylium	1E19
p-$Al_{0.4}Ga_{0.6}As$	12000	1	Berylium	5E17
AlGaAs/GaAs	250	1		
GaAs	150	1		
GaAs	350	5		
InGaAs	60	5		
InAs	9	5		
InGaAs	20	5		
GaAs	500	1		
AlGaAs/GaAs	250	1		
n-$Al_{0.4}Ga_{0.6}As$	12000	1	Silicon	2E18
n-GaAs	3000	1	Silicon	2E18

Table 1. Layer structure for quantum-dot sample used in this study.

4.3 Device Structure

The QD material was fabricated into multisection shallow-etch ridge devices of widths ranging from 20 to 4 μm in one process run. The lateral leakage current in a device consists of the spreading of current in the conductive upper cladding layer above the active region and the lateral diffusion of carriers in the active region [2]. In order to study only the effect of lateral diffusion current on device performance, current spreading in the conductive upper cladding layer was eliminated by etching the ridges down to the interface between the doped upper cladding layer and the undoped GaAs-$Al_{0.4}Ga_{0.6}As$ waveguide layer [3, 4, 5, 6]. The etched areas were planarised and insulated using Benzocyclobutene (BCB). Figure 4-2 illustrates the ridge profile and the coordinate system used throughout this study. A detailed description of the fabrication process can be found in Chapter 3. The as-cleaved and uncoated multisection bars were mounted p-side up onto copper blocks using silver epoxy for temperature controlled single pass measurements of the amplified spontaneous emission. The actual values of the ridge widths were measured by scanning electron microscopy (SEM). All measurements were performed as described in Chapter 2.

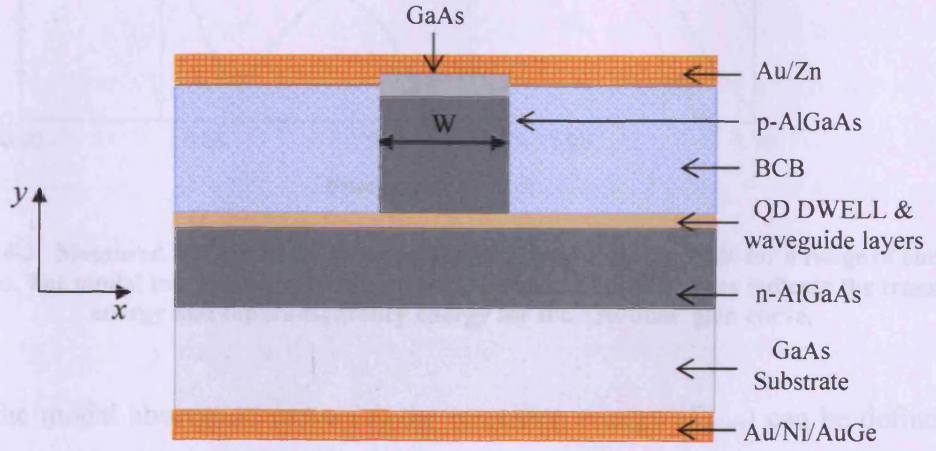

Figure 4-2. Schematic of the ridge structure.

4.4 Experimental Results

4.4.1 Modal Gain and Internal Optical Loss Dependence on Ridge Width

In Figure 4-3, an example of the TE net modal gain spectra obtained by a 6μm ridge at 350K is plotted as a function of photon energy for a range of current densities. The net modal loss spectrum ($A+\alpha_i$) is also included for comparison. There are two distinct energy transitions observed in the net modal gain spectra which correspond to the inhomogenously broadened ground state (centred at ~0.938eV) and first excited state (centred at ~1.012eV). The presence of a second excited state transition starts becoming apparent at the higher drive current densities.

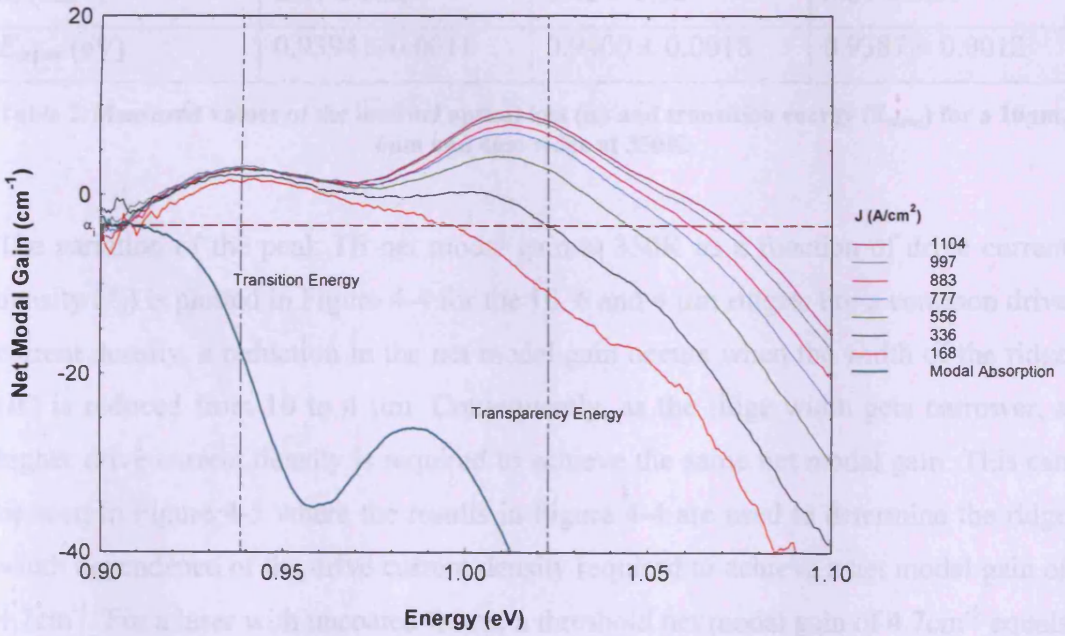

Figure 4-3. Measured TE net modal gain spectra for a 6μm ridge at 350K for a range of current densities. The modal loss spectrum is also shown. The vertical dashed lines indicate the transition energy and the transparency energy for the 336A/cm^2 gain curve.

From the modal absorption curve (A) the transition energy (E_{trans}) can be defined as the point where the absorption is half of the peak ground state absorption and the transparency energy is as defined in Chapter 2.

In Table 2 the measured parameters for α_i and E_{trans} are given for different ridge widths. Since α_i and E_{trans} do not show any systematic change with drive current and are not expected to vary with drive current, the values quoted are the mean of all the drive currents analysed for a particular ridge width. An error in α_i is obtained from the standard deviation and an error in E_{trans} from the standard deviation and α_i error. The table shows that as the ridge width narrows an increase in α_i occurs. We attribute this mainly to the interaction of the optical mode with the roughness of the etched ridge increasing the scattering loss [7, 8, 9]. There is no variation of E_{trans} with ridge width within the experimental error and this is expected because the material system is the same.

Ridge Width (μm)	**10**	**6**	**4**
α_i **(cm^{-1})**	2.57 ± 0.65	3.42 ± 0.92	5.87 ± 0.60
E_{trans} **(eV)**	0.9394 ± 0.0011	0.9400 ± 0.0018	0.9387 ± 0.0012

Table 2. Measured values of the internal optical loss (α_i) and transition energy (E_{trans}) for a 10μm, 6μm and 4μm ridge at 350K.

The variation of the peak TE net modal gain at 350K as a function of drive current density (J_d) is plotted in Figure 4-4 for the 10, 6 and 4 μm ridges. For a common drive current density, a reduction in the net modal gain occurs when the width of the ridge (W) is reduced from 10 to 4 μm. Consequently, as the ridge width gets narrower, a higher drive current density is required to achieve the same net modal gain. This can be seen in Figure 4-5 where the results in Figure 4-4 are used to determine the ridge width dependence of the drive current density required to achieve a net modal gain of 4.7cm^{-1}. For a laser with uncoated facets, a threshold net modal gain of 4.7cm^{-1} equals the mirror loss ($ln(1/R)/L$), of reflectivity 0.28 (as calculated using the effective index of the fundamental mode), when the cavity length is 2.7mm. Figure 4-5 therefore represents the J_{th}-W characteristic for 2.7mm long shallow-etched ridge lasers with uncoated facets.

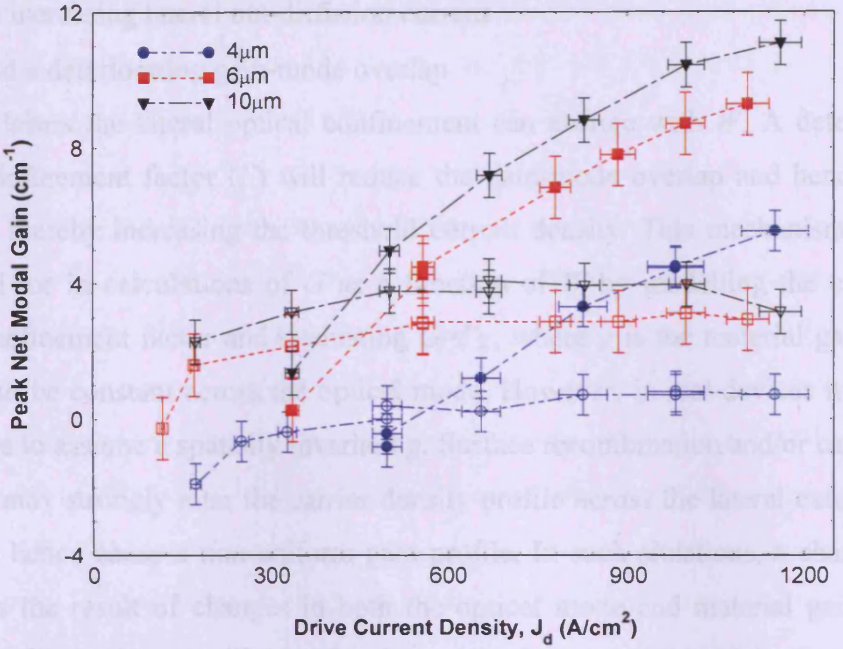

Figure 4-4. The peak net modal gain (G-α_i) as a function of drive current density for the ground (open symbols) and excited state (closed symbols) at 350K. The black triangles, red squares, and blue circles correspond to the 10, 6 and 4 μm ridge widths.

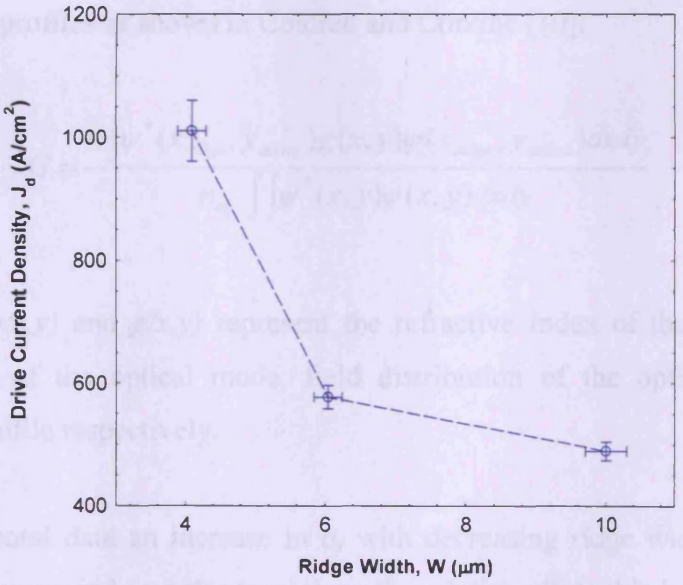

Figure 4-5. The drive current density required for each ridge width to achieve a net modal gain of 4.7cm^{-1} at 350K. The graph is representative of the J_{th}-W characteristic for 2.7mm shallow-etched ridge lasers with uncoated facets.

As mentioned in the introduction, the key mechanisms that can cause the increase in threshold current density with decreasing ridge width seen in Figure 4-5 are:

- an increasing α_i,

- an increasing lateral out-diffusion current
- and a deteriorating gain-mode overlap

In RWG lasers the lateral optical confinement can change with W. A deteriorating optical confinement factor (Γ) will reduce the gain-mode overlap and hence modal gain (G); thereby increasing the threshold current density. This mechanism is often accounted for in calculations of G as a function of W by modelling the change in optical confinement factor and evaluating $G=\Gamma g$, where g is the material gain and is assumed to be constant across the optical mode. However, in real devices it may not be suitable to assume a spatially invariant g. Surface recombination and/or carrier out-diffusion may strongly alter the carrier density profile across the lateral extent of the ridge and hence cause a non-uniform gain profile. In such situations, a change in G with W is the result of changes in both the optical mode and material gain profile [4][10]. In this study, we will describe changes to the measured modal gain with W in terms of changes in the gain-mode overlap integral, rather than trying to attribute the mechanism to a change in either profile. Modelling the modal gain in a situation of an optical mode profile and material gain profile can be done by evaluating the overlap integral of both profiles as shown in Coldren and Corzine [10]:

$$G = \frac{n \int \psi^*(x_{ridge}, y_{active}) g(x,y) \psi(x_{ridge}, y_{active}) dxdy}{n_{eff} \int\int \psi^*(x,y)\psi(x,y)dxdy} \tag{4.1}$$

where n, n_{eff}, $\psi(x,y)$ and $g(x,y)$ represent the refractive index of the active region, effective index of the optical mode, field distribution of the optical mode, and material gain profile respectively.

In the experimental data an increase in α_i with decreasing ridge width has already been shown to occur and in order to analyse the relative effect this has, a plot of the peak modal gain (G) produced by the different ridge widths as a function of drive current density is given in Figure 4-6. In evaluating the peak modal gain it is assumed that α_i is approximately invariant across the net modal gain spectra. This assumption is supported by lateral near-field measurements as a function of current density. As the current density is increased and emission from the higher energy states becomes more dominant the measured mode profile may perhaps significantly change and as

such so too might the optical scattering losses. However measurements of the normalised full-width-half-maximum of the near-field profile did not show any such significant change with current density.

In Figure 4-6 the excited state data shows that even with α_i taken into account, the modal gain - before gain saturation occurs - still gets progressively smaller with decreasing ridge width at a common drive current density. The ridge width dependence of the ground state modal gain shows little apparent variation because over this drive current density range the gain varies gradually. Had the increase in current density in Figure 4-5 been exclusively to do with the increase in α_i, then, at a given drive current density, the modal gain in each of the ridge widths would have been the same. This result shows that the change in α_i with ridge width is not the only mechanism having an impact on the J_{th}-W characteristic. The contribution from the other key mechanisms (i.e. increasing lateral out-diffusion current and deteriorating gain-mode overlap) must also be considered.

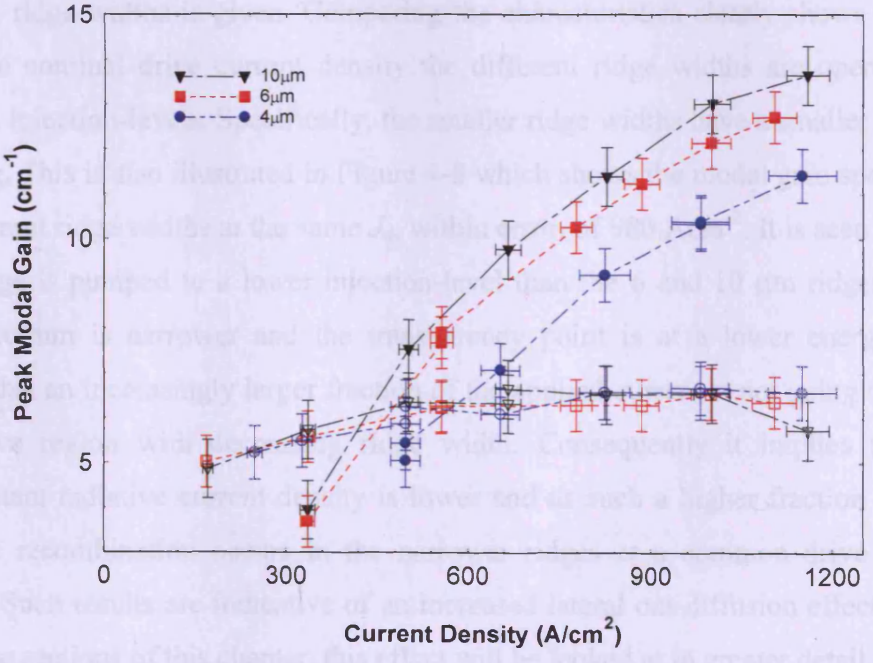

Figure 4-6. The peak modal gain (G) as a function of drive current density for the ground (open symbols) and excited state transitions (closed symbols) at 350K. The black triangles, red squares, and blue circles correspond to the 10, 6 and 4 μm ridge widths.

In order to assess the relative impact of the gain-mode overlap and lateral out-diffusion mechanisms, and to facilitate comparisons between different ridge widths at a common operating point, the difference between the transparency energy (ΔE_f) and transition energy (E_{trans}) will be used as a measure of the carrier injection, or rather inversion-level, in the device (i.e. how hard the device is being driven in the spirit of the Bernard and Durrafourg condition [11]). This difference will be termed as the carrier injection-level and because it defines an intrinsic measure of the quasi Fermi-level separation relative to a transition energy reference that is common to all of the devices (E_{trans}), it can be used as a valid common operating point to directly compare the performance of different ridge widths. This method of comparison is somewhat similar to that used by [12] where a matched transparency energy and spectral location of the peak modal gain (i.e. when the modal gain spectra matched) were used to imply equivalent pumping of the active region between different width mesas of the same material system.

In Figure 4-7 the carrier injection-level as a function of drive current density for different ridge widths is given. Comparing the characteristics clearly shows that for the same nominal drive current density the different ridge widths are operating at different injection-levels. Specifically, the smaller ridge widths have a smaller level of pumping. This is also illustrated in Figure 4-8 which shows the modal gain spectra for the different ridge widths at the same J_d, within error, of 980 Acm^{-2}. It is seen that the 4μm ridge is pumped to a lower injection-level than the 6 and 10 μm ridges as the gain spectrum is narrower and the transparency point is at a lower energy. This reveals that an increasingly larger fraction of the applied current is not going to pump the active region with decreasing ridge width. Consequently it implies that the concomitant radiative current density is lower and as such a higher fraction of non-radiative recombination occurs in the narrower ridges at a common drive current density. Such results are indicative of an increased lateral out-diffusion effect. In the following sections of this chapter, this effect will be looked at in greater detail.

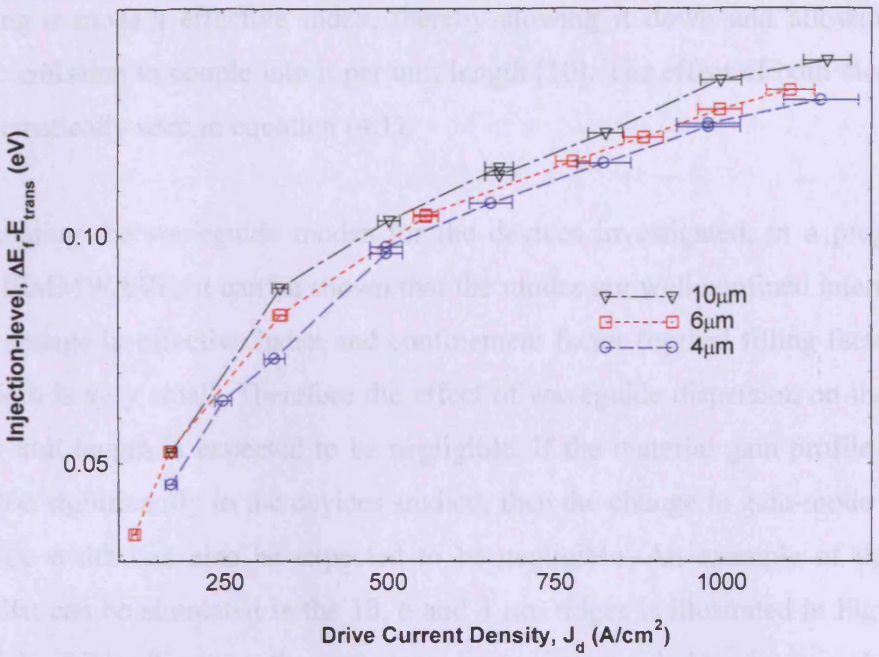

Figure 4-7. Carrier injection level (ΔE_f- E_{trans}) as a function of drive current density (J_d) for the 10μm (black triangles), 6μm (red squares), and 4μm (blue circles) at 350K.

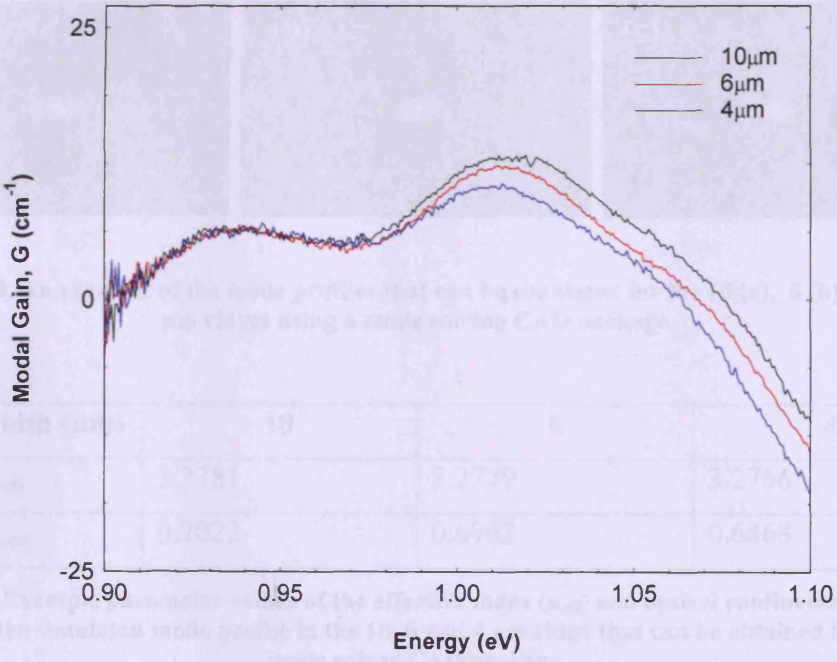

Figure 4-8. Modal gain (G) spectra for the 10 (black), 6 (red), and 4 (blue) μm S-RWG devices at a J_d, within error, of 980A/cm^2.

When each ridge device is driven to a common carrier injection-level, the modal gain per unit length must be the same provided a change doesn't occur in either the gain-mode overlap or waveguide dispersion. Waveguide dispersion has the effect of

wreducing a mode's effective index, thereby slowing it down and allowing more radiative emission to couple into it per unit length [10]. The effect of both factors can be mathematically seen in equation (4.1).

By simulating the waveguide modes for the devices investigated, in a programme such as FIMMWAVE, it can be shown that the modes are well confined laterally and that the change in effective index and confinement factor (optical filling factor) with ridge width is very small. Therefore the effect of waveguide dispersion on the modal gain per unit length is expected to be negligible. If the material gain profile doesn't change too significantly in the devices studied, then the change in gain-mode overlap with ridge width can also be expected to be negligible. An example of the mode profile that can be simulated in the 10, 6 and 4 μm ridges is illustrated in Figure 4-9, for which Table 3 gives the corresponding effective index (n_{eff}) and optical confinement factor values Γ_{opt}.

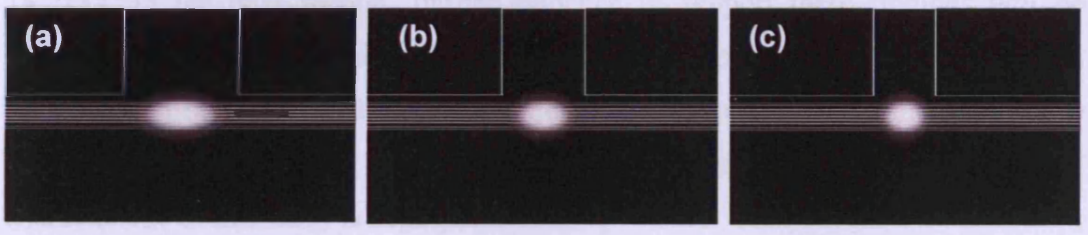

Figure 4-9. An example of the mode profiles that can be simulated for the 10 (a), 6 (b) and 4 (c) μm ridges using a mode solving CAD package.

Ridge Width (μm)	10	6	4
n_{eff}	3.2781	3.2779	3.2766
Γ_{opt}	0.7022	0.6962	0.6868

Table 3. Example parameter values of the effective index (n_{eff}) and optical confinement factor (Γ_{opt}) for the simulated mode profile in the 10, 6 and 4 μm ridge that can be obtained by using a mode solver CAD package.

In Figure 4-10, the modal gain characteristics as a function of carrier injection-level for different ridge widths are compared. The comparison clearly shows that for a given carrier injection-level, the different ridge width structures provide the same modal gain. This result reveals that the change in gain-mode overlap and waveguide

dispersion is negligible over the range of ridge widths studied – as indicated by waveguide simulations. Confirmation for the findings in Figure 4-10 can be seen by comparing the modal gain spectra of the different ridge widths at common carrier injection-levels. Figure 4-11 shows this for the data points with the closest matching injection-levels. Given that the injection-levels are not exactly the same and that each gain spectrum has some degree of uncertainty, the same modal gain spectrum is clearly exhibited by the different ridge widths.

When a ridge width is sufficiently small to cause a significant reduction in the gain-mode overlap, then in order to exhibit the same model gain as a broader ridge an elevated carrier injection-level and a larger concomitant radiative current density will be required to overcome the reduced net gain provided to the optical mode by the structure. In reality, gain saturation effects may prevent such a level being reached. The implications of a reduced gain-mode overlap on the J_{th}-W characteristic are qualitatively clear: threshold currents will be increased, and efficiencies reduced [13, 14, 15]. In the next section, further evidence to support these findings will be presented with results that show the same radiative current density is obtained at the same modal gain for the different ridges widths. In view of the results, the quantitative impact of the deteriorating gain-mode overlap mechanism on the measured J_{th}-W characteristic of this study is negligible.

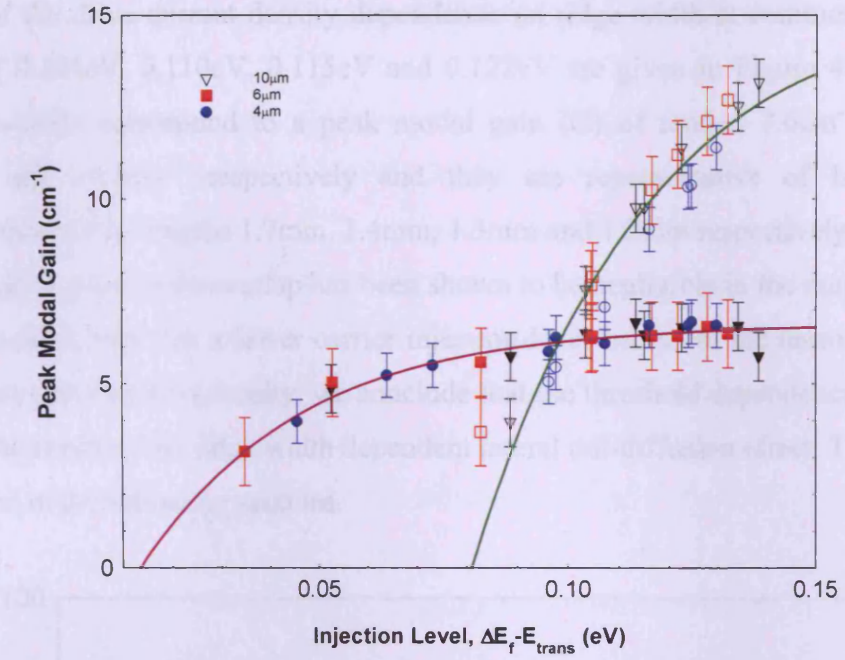

Figure 4-10. The peak modal gain as a function of carrier injection-level for the ground state (solid symbols) and excited state (open symbols) transitions at 350K. The black triangles, red squares, and blue circles correspond to the 10, 6 and 4 μm ridges.

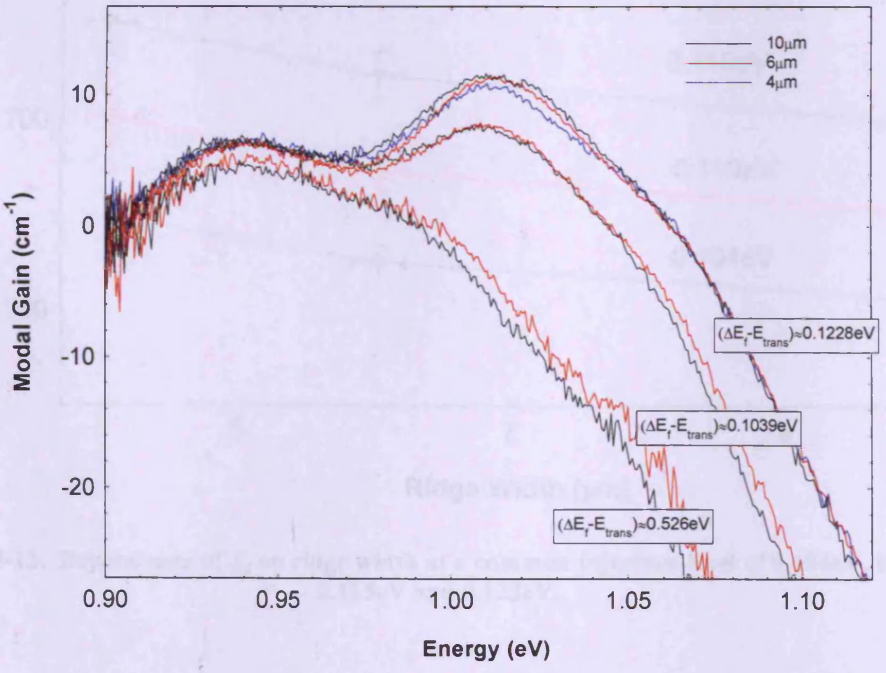

Figure 4-11. Modal gain spectra of the 10 (black) and 6 μm (red) ridges at injection-levels of approximately 0.5260, 0.1039 and 0.1228 eV. The 4μm (blue) ridge at approximately 0.1228eV is also shown.

A plot of the drive current density dependence on ridge width at common injection levels of 0.104eV, 0.110eV, 0.115eV and 0.122eV are given in Figure 4-12. These injection-levels correspond to a peak modal gain (G) of around 7.6cm^{-1}, 8.9cm^{-1}, 9.7cm^{-1} and 10.8cm^{-1} respectively and they are representative of lasers with approximate cavity lengths 1.7mm, 1.4mm, 1.3mm and 1.2mm respectively. Now that the change in gain-mode overlap has been shown to be negligible in the range of ridge widths studied, and that a lower carrier injection-level occurs in the narrower ridges for a given drive current density, we conclude that the threshold dependence in Figure 4-12 is the result of the ridge width dependent lateral out-diffusion effect. This will be confirmed in the following sections.

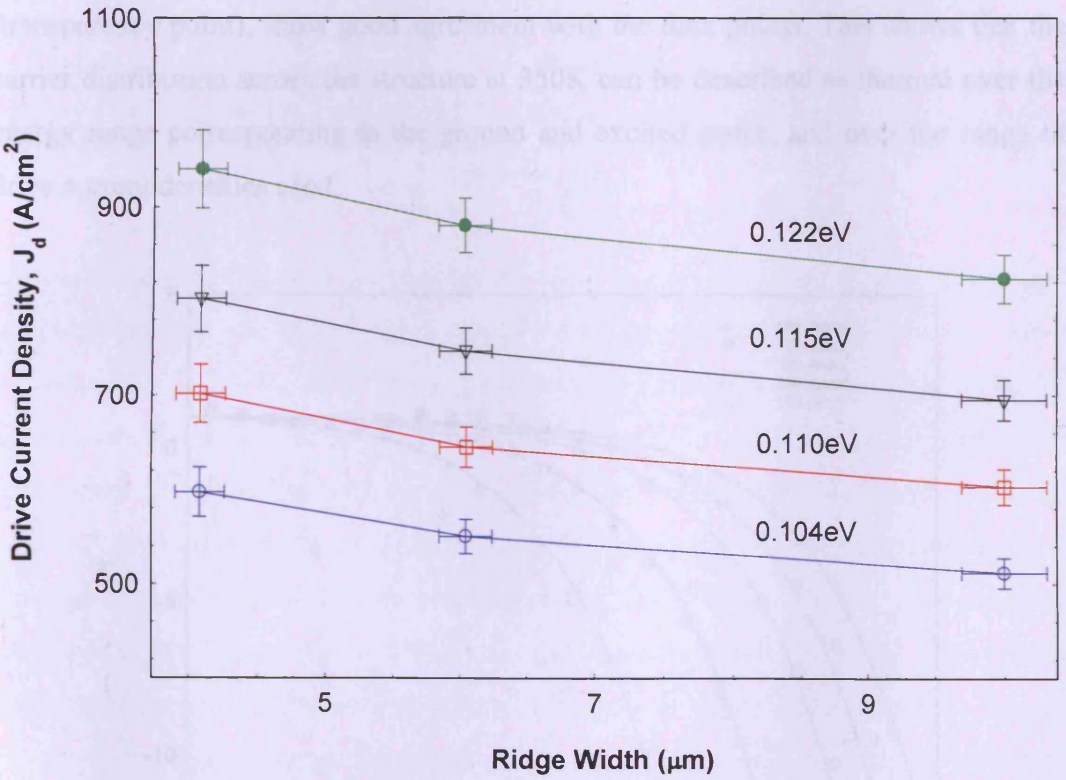

Figure 4-12. Dependence of J_d on ridge width at a common injection-level of 0.104eV, 0.110eV, 0.115eV and 0.122eV.

4.4.2 Radiative Current Density Dependence on Ridge Width

As detailed in Chapter 2, the measured spontaneous emission rate spectra of a ridge can be transformed from arbitrary units into real units by determining the calibration factor. The calibration factor (C') is found from the spectra of the population inversion factor (P*f*/C') which is the ratio of the measured gain and spontaneous emission. At low photon energies the P*f*/C' spectrum for each drive current converges to a common region where the P*f* equals 1; this enables C' to be found. Figure 4-13 and Figure 4-14 show the calibrated TE P*f* and spontaneous emission spectra for the 6μm ridge at 350K. In Figure 4-13 functions describing a Fermi-Dirac distribution obtained with the experimental values of the quasi-Fermi level separation (transparency point), show good agreement with the data points. This shows that the carrier distribution across the structure at 350K can be described as thermal over the energy range corresponding to the ground and excited states, and over the range of drive current densities used.

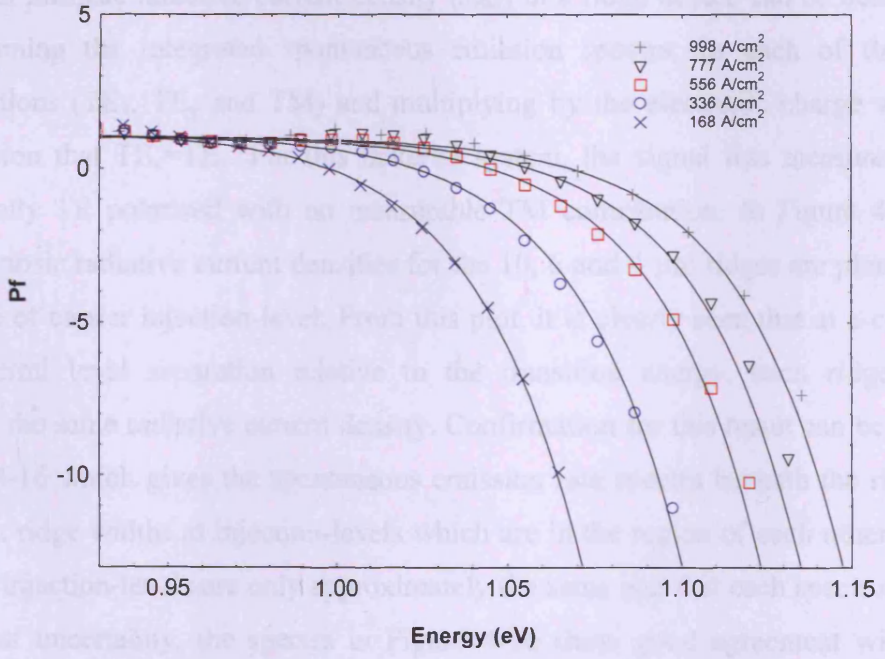

Figure 4-13. Measured spectra of the population inversion factor (P*f*) at various drive current densities (data points) for a 6μm ridge at 350K. The solid lines represent calculated Fermi-Dirac distributions obtained using the measured quasi-Fermi levels (transparency point) for each drive current density.

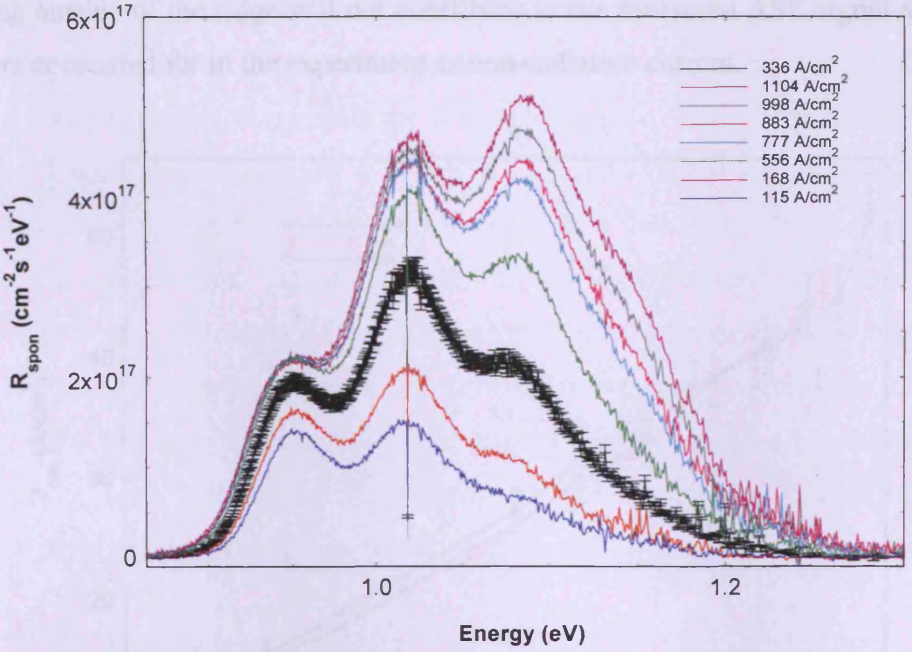

Figure 4-14. Calibrated spectra of the TE spontaneous emission rate for various drive current densities, for a 6μm ridge at 350K. For clarity, the error bars have only been included on the 336A/cm^2 plot.

The total intrinsic radiative current density (J_{rad}) in a ridge device can be determined by summing the integrated spontaneous emission spectra for each of the three polarisations (TE_x, TE_y and TM) and multiplying by the electronic charge with the assumption that TE_x=TE_y. For this material system, the signal was measured to be dominantly TE polarised with no measurable TM contribution. In Figure 4-15 the total intrinsic radiative current densities for the 10, 6 and 4 μm ridges are plotted as a function of carrier injection-level. From this plot, it is clearly seen that at a common quasi-Fermi level separation relative to the transition energy, each ridge width exhibits the same radiative current density. Confirmation for this result can be seen in Figure 4-16 which gives the spontaneous emission rate spectra beneath the ridge for different ridge widths at injection-levels which are in the region of each other. Given that the injection-levels are only approximately the same and that each spectrum has a degree of uncertainty, the spectra in Figure 4-16 show good agreement with each other.

Carriers diffusing outside of the ridge are not expected to contribute to the radiative current density. Simulating the optical modes in a commercial mode-solving package shows the modes to be well confined under the ridge. This means that all carriers

diffusing outside of the ridge will not contribute to the measured ASE signal and are therefore accounted for in the experiment as non-radiative current.

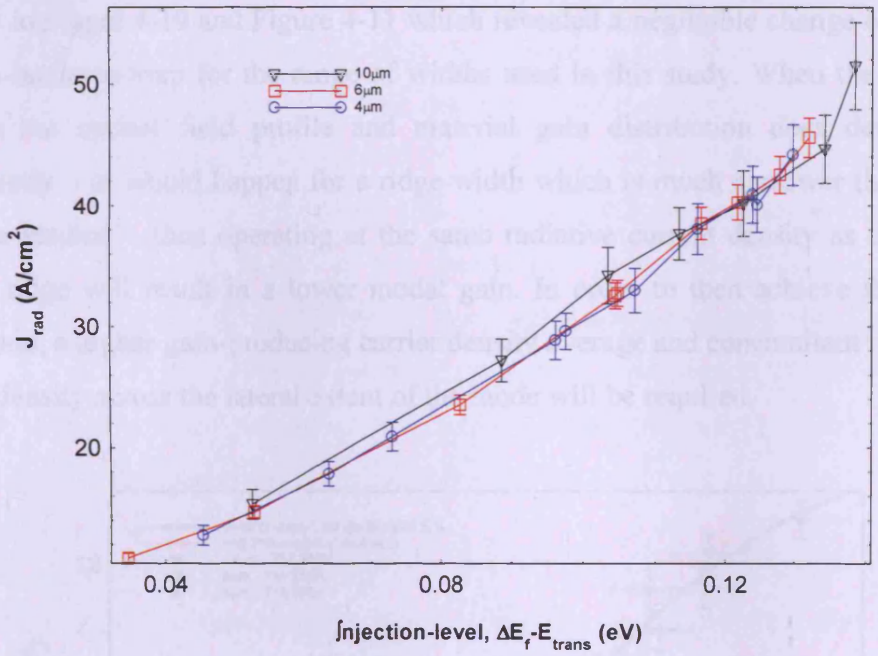

Figure 4-15. The total radiative current density (J_{rad}) as a function of injection-level (ΔE_f - E_{trans}) for the 10, 6 and 4 μm ridges at 350K.

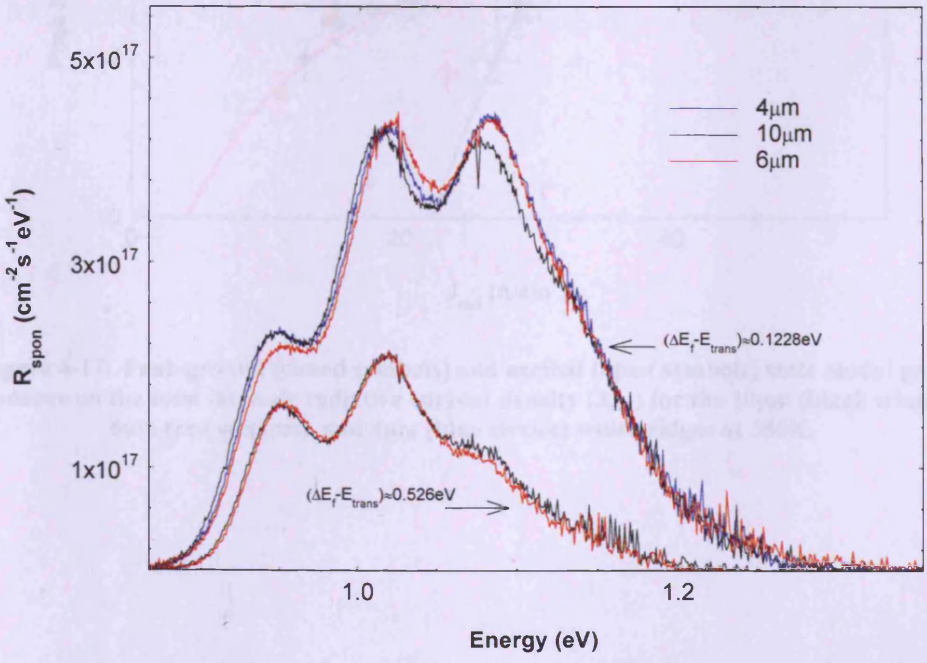

Figure 4-16. Spontaneous emission rate spectra of the 10, 6 and 4 μm ridges at injection-levels in the region of 0.526eV and 0.1228eV.

Figure 4-17 is plot of the peak modal gain achieved in the different ridge widths as a function of their radiative current density. It shows that each ridge requires the same radiative current density to produce the same modal gain. This is supportive of the findings in Figure 4-10 and Figure 4-11 which revealed a negligible change occurs in the gain-mode overlap for the range of widths used in this study. When the overlap between the optical field profile and material gain distribution does deteriorate significantly – as would happen for a ridge width which is much narrower than what has been studied – then operating at the same radiative current density as that of a broader ridge will result in a lower modal gain. In order to then achieve the same modal gain, a higher gain-producing carrier density average and concomitant radiative current density across the lateral extent of the mode will be required.

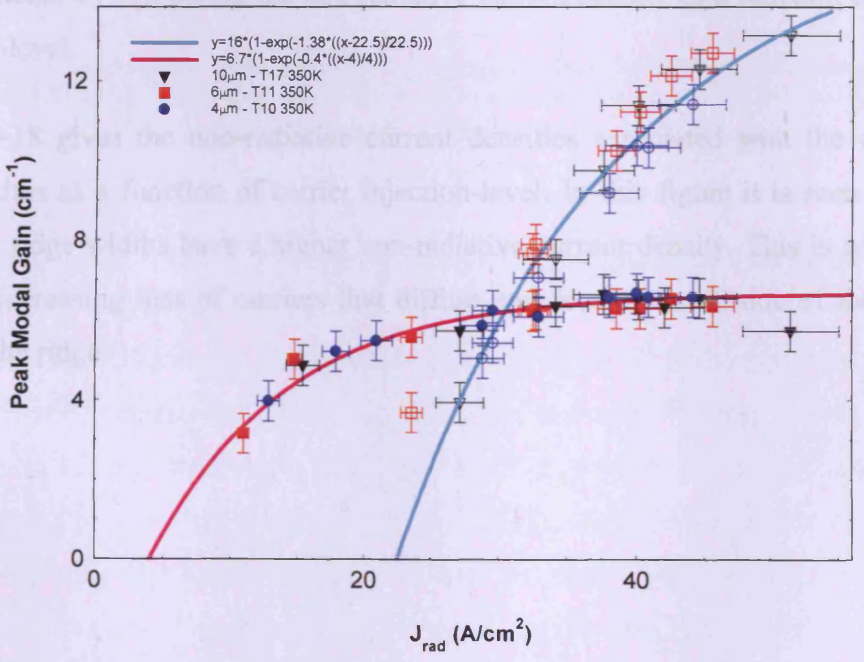

Figure 4-17. Peak ground (closed symbols) and excited (open symbols) state modal gain dependence on the total intrinsic radiative current density (J_{rad}) for the 10μm (black triangles), 6μm (red squares), and 4μm (blue circles) width ridges at 350K.

4.4.3 Non-Radiative Current Density Dependence on Ridge Width

Up to this point, the key mechanisms involving changes in the internal optical loss and gain-mode overlap with decreasing ridge width have been experimentally evaluated and the relative impact of each mechanism on the threshold characteristic with ridge width has been assessed. The analysis found the internal optical loss with respect to the 10μm ridge to increase by a factor of 1.3 and 2.3 for the 6 and 4 μm ridges respectively. The gain-mode overlap changed negligibly with ridge width and therefore the quantitative impact of this mechanism on the threshold characteristic with ridge width is negligible. The other key mechanism which involves the lateral out-diffusion of carriers has so far not been quantified, but it has, in Figure 4-7, been indicated to have a significant effect. The impact of this mechanism can be analysed in more detail by comparing the non-radiative current density as a function of carrier injection-level.

Figure 4-18 gives the non-radiative current densities associated with the different ridge widths as a function of carrier injection-level. In this figure it is seen that the narrower ridge widths have a higher non-radiative current density. This is consistent with an increasing loss of carriers that diffuse and recombine outside of the region beneath the ridge.

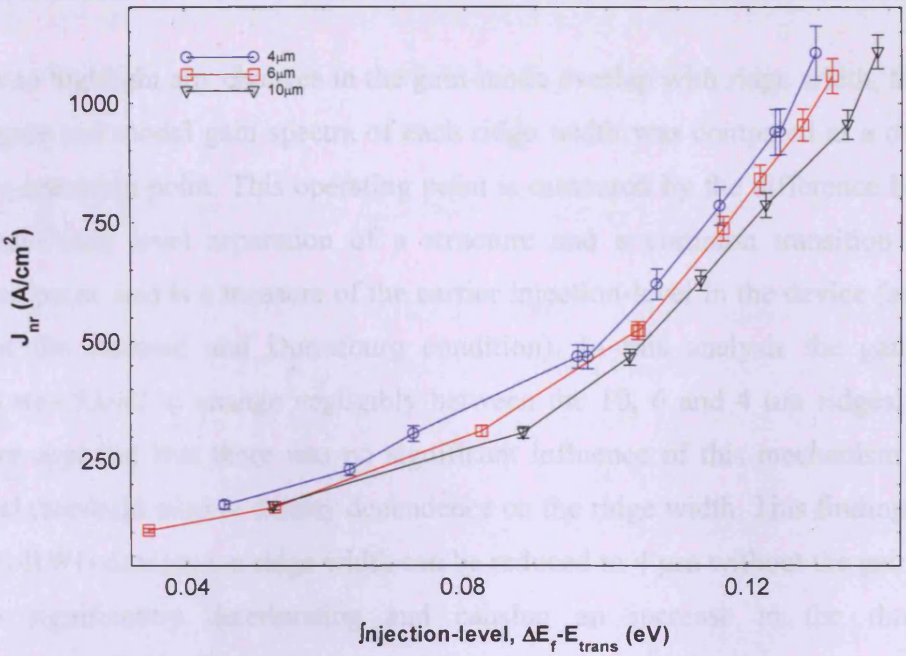

Figure 4-18. Non-radiative current density (J_{nr}) associated with the 10μm (black triangles), 6μm (red squares) and 4μm (blue circles) width ridges as a function of carrier injection-level ($\Delta E_f - E_{trans}$), at 350K.

4.4.4 Discussion and Summary of the Experimental Findings

The QD S-RWG devices have been characterised in terms of: internal optical loss (α_i), modal gain (G), radiative current density (J_{rad}), and non-radiative current density (J_{nr}). By analysing these characteristics as a function of ridge width (W) and comparing the differences at a common injection-level (ΔE_F-E_{trans}) the relative impact of the key mechanisms affecting the threshold dependence on ridge width have been evaluated. These key mechanisms include: (1) the internal optical loss, (2) gain-mode overlap, (3) loss of carriers to lateral out-diffusion.

In 4.4.1, α_i was measured to increase with decreasing ridge width. In comparison to the 10 μm ridge which had a α_i value of 2.75 ± 0.65 cm^{-1}, the increase in the 6 and 4 μm ridges was by a factor of 1.2 and 2.3 respectively. The implication of this was a significant increase in the threshold condition with decreasing ridge width. Consequently, the results show that the quantitative impact of a changing α_i with ridge width on the J_{th}-W characteristic can be significant and therefore ought to be considered in any evaluation of device performance with changing ridge width.

spirit of the Bernard and Durrafourg condition). In this analysis the gain-mo overlap was found to change negligibly between the 10, 6 and 4 μm ridges. It w therefore apparent that there was no significant influence of this mechanism on t observed threshold current density dependence on the ridge width. This finding sho that in S-RWG devices the ridge width can be reduced to 4 μm without the gain-mo overlap significantly deteriorating and causing an increase in the thresho Confirmation of this finding was found by showing that the same total radiati current density produced the same modal gain in all of the ridge widths. However, t impact of a deteriorating gain-mode overlap may possibly be significant for rid widths narrower than 4 μm [13, 15].

It was found in Figure 4-12 that in order for each device to operate at a comm carrier injection-level and therefore common modal gain, a higher drive curre density was required with decreasing ridge width. By comparing the non-radiati current density at common carrier injection-levels in Figure 4-18, it was clear that t cause of the increase in drive current density was a higher non-radiati recombination current density in the narrower ridges. This effect highlighted th lateral out-diffusion was having a significant impact on increasing the thresho current density dependence with decreasing ridge width. As an example, the fraction increase ($J_d(W)/J_d(10\mu m)$) in drive current density at an injection-level of 0.122e (this corresponds to a modal gain of 10.8cm^{-1}) for the 6 and 4 μm ridges with respe to the 10μm ridge is 1.07 and 1.14 respectively. Since this is a fairly small impact implies that the lateral ambipolar diffusion length will also be fairly small. In the ne section of this chapter a standard ambipolar diffusion model will be used to fit t increase in drive current density that is caused by lateral out-diffusion to determi the lateral ambipolar diffusion length. The results of the model will be shown to agr

very well with the measured results, thereby providing a convincing estimate of the lateral ambipolar diffusion length in the active region.

4.5 Modelling the Lateral Carrier Diffusion Effect

In this section, the lateral ambipolar diffusion length (L_d) for various carrier injection-levels will be estimated by fitting a standard diffusion length model to the measured increase in drive current density (J_d) that was caused by increasing lateral out-diffusion with decreasing ridge width (W) (c.f. Figure 4-12). The model involves analytically solving the ambipolar carrier diffusion equation to yield solutions for the lateral carrier density profile in the active region. Distributions for a common average carrier density beneath the different ridge widths and hence common radiative current density are then calculated and used to fit the measured J_d-W relation at various carrier injection-levels. In these calculations L_d is the only fitting parameter and also the only unmeasured parameter.

The section begins by formulating a solution of the lateral carrier density profile across the ridge from the ambipolar diffusion equations. Following this, a detailed methodology of determining the J_d-W relation from the carrier density profiles of the various ridge widths is formed. Some of the assumptions used in the method refer back to the experimental data for justification. Device modelling then takes place using the measured data from the earlier characterisation measurements.

4.5.1 Model of the Lateral Carrier Density Profile

For the ridge waveguide structure used in this study, the injected current (I_{in}) can be expressed by [16, 18]:

$$I_{in}(W) = J_r \cdot L \cdot W + I_{out}(W) \tag{4.2}$$

where J_r is the average recombination current density beneath the ridge, I_{out} is the lateral out-diffusion current that occurs from the recombination of carriers diffusing out of the active region beneath the ridge, W is the ridge width and L is the length of the cavity. Normally at a common operating point such as threshold, (4.2) would have a functional dependence on W and L but since L is kept constant throughout this investigation its dependence has been excluded from the equation. An illustration of these parameters is given in Figure 4-19.

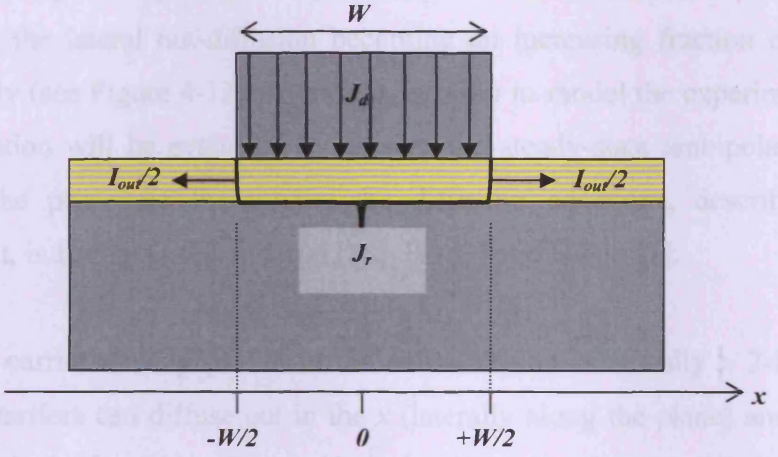

Figure 4-19. Illustration of the current paths used in Equation (4.2) and the coordinate system of the carrier diffusion model.

When W is much wider than the lateral carrier diffusion length (L_d), I_{out} will approximately be independent of W. In this case the carrier density profile will be uniform across most of the ridge width (as will be shown later) and a linear fit to the I_{in}-W relation will yield I_{out} and J_r from the intercept and slope respectively. The dependence of I_{out} on W starts becoming apparent when W is on the order of the lateral diffusion length. In this case the carrier density profile will no longer be uniform across most of the ridge width and the I_{in}-W relation will no longer be linear. For such situations, the I_{in}-W (or equivalently J_d-W) relation is commonly evaluated by analytically solving the steady-state ambipolar diffusion equation. Although such analytic solutions are not as accurate or detailed as numerical solutions, they do nevertheless illustrate the underlying physics of the I_{in}-W relation and help facilitate the estimation of parameters, such as the L_d, from fits to experimental data. As a result,

these solutions are considered to be more convenient for practical laboratory applications. The analytic solutions found in literature [3, 8, 15, 17, 18] essentially use the same approximations to obtain an expression for the lateral carrier density profile. Note in some of these studies the J_d-W relation was determined instead, and some of them had to include the effect of current spreading because they were working with stripe geometry devices.

Earlier in this chapter, the current density required to reach a common operating point (as determined by the injection-level) was seen to increase with decreasing ridge width due to the lateral out-diffusion becoming an increasing fraction of the total current density (see Figure 4-12). Therefore, in order to model the experimental data, the J_d-W relation will be evaluated by solving the steady-state ambipolar diffusion equations. The procedure for solving the diffusion equations, described in the following text, is similar to that of Letal [18], Hu [3] and Hakki [1].

The injected carrier density profile in the active region is actually a 2-D problem because the carriers can diffuse out in the x (laterally along the plane) and y (across the active region) directions. The problem, however, can be simplified into a 1-D diffusion problem by noting that the thickness of the active region (d) is much smaller than the ridge width (W) and lateral ambipolar diffusion length (L_d). Consequently the time taken for carriers to diffuse across the active region is comparatively instantaneous to the time taken for them to diffuse laterally across the active region. The carrier density profile across d can then be assumed to be constant, and the problem therefore reduces to 1-D problem which is along the lateral direction.

In the single pass, multisection experiment where stimulated emission is negligible, the diffusion of carriers in the lateral direction is governed by the equation:

$$D_a \frac{\partial^2 n(x)}{\partial x^2} + \frac{J_d}{d \cdot q} - \frac{n(x)}{\tau} = 0 \qquad \textbf{(4.3)}$$

where $n(x)$, τ, J_d and D_a denote the carrier density, average carrier lifetime, drive current density and effective ambipolar diffusion coefficient respectively. For the device structure used, the boundaries of ridge width at $x=\pm W/2$ limit the area of current injection. This injected drive current density J_d is assumed to be uniform across W and zero elsewhere (i.e. a step function):

By taking the carrier lifetime (τ) to be spatially invariant, (4.3) is then solved by matching the continuity of current ($dn(x)/dx$) and carrier concentration ($n(x)$) at the ridge boundary to yield the lateral carrier density profile both inside (4.4) and outside (4.5) of the ridge:

$$n(x)=\frac{J_d\cdot\tau}{q\cdot d}\left(1-e^{-\frac{W}{2L_d}}\cdot\cosh\left(\frac{x}{L_d}\right)\right), \qquad |x|\le\frac{W}{2} \tag{4.4}$$

$$n(x)=\frac{J_d\cdot\tau}{q\cdot d}e^{-\frac{|x|}{L_d}}\cdot\sinh\left(\frac{W}{2L_d}\right), \qquad |x|\ge\frac{W}{2} \tag{4.5}$$

where L_d is given by $\sqrt{D_a\tau}$. The average recombination current density beneath the ridge is given by the integral

$$J_r=\frac{d\cdot q}{W}\int_{-W/2}^{W/2}\frac{n(x)}{\tau}dx \tag{4.6}$$

which when solved yields

$$J_r=J_d\left(1-\frac{L_d}{W}\left(1-e^{-\frac{W}{L_d}}\right)\right) \tag{4.7}$$

The injected current can be expressed as $I_{in}=L\cdot W\cdot J_d$. By rearranging equation (4.7) to obtain J_d the injected current can then be expressed in terms of J_r and L_d:

$$I_{in} = \frac{L \cdot W \cdot J_r}{1 - \frac{L_d}{W}\left(1 - e^{-W/L_d}\right)} \tag{4.8}$$

An expression for the lateral out-diffusion current can then be found by substituting equation (4.8) into equation (4.2):

$$I_{out}(W) = \frac{J_r \cdot L \cdot L_d\left(1 - e^{-W/L_d}\right)}{1 - \frac{L_d}{W}\left(1 - e^{-W/L_d}\right)} \tag{4.9}$$

Equation (4.9) reveals certain characteristics of the I_{in}-W relation which were discussed at the beginning of this section. When W becomes much greater than L_d, I_{out} approaches a constant equal to $J_r.L.L_d$. Therefore, $\cdot J_d$ also approaches a constant and becomes independent of W while W remains much greater than L_d.

4.5.2 Modeling J_d-W at an injection-level of 0.122eV

In the study by Letal [18], the average recombination beneath the ridge was assumed to be independent of ridge width at a common operation point such as threshold. In this model we will make the same assumption but at a more restrictively defined common operating point i.e. common injection-level. Earlier in the chapter we proved this assumption is good using experimental results on the spontaneous emission and radiative recombination current density. Together these measurements showed that the radiative recombination current density (which is assumed to be an average beneath the ridge because it is derived from the ASE emanating from the ridge and is by definition the light which has experienced gain i.e. from light which has been guided and amplified beneath the ridge) was independent of ridge width for a given injection-level. It is therefore reasonable to assume that the total recombination beneath the ridge is the same i.e. J_r is the same in all ridge widths at a common injection-level.

The fitting routine for determining J_r and L_d involves solving equation (4.7) using the measured drive current density for a particular injection-level. In solving (4.7), a graphical plot of the J_r-L_d relation for each ridge width is used to determine an ambipolar diffusion length that satisfies the condition of a common J_r (and hence J_{rad}). Such a plot is given in Figure 4-20 for an injection-level of 0.122eV. It is clearly seen in Figure 4-20 that only one solution for L_d exists for a common J_r, for which $L_d \approx$ 0.84μm and $J_r \approx 759 A/cm^2$. In Table 4, the calculated parameters of J_r and I_{out} for a L_d of 0.84μm are given along with the measured parameters for W, J_d, J_{rad}, and J_{nr} at an injection-level of 0.122eV.

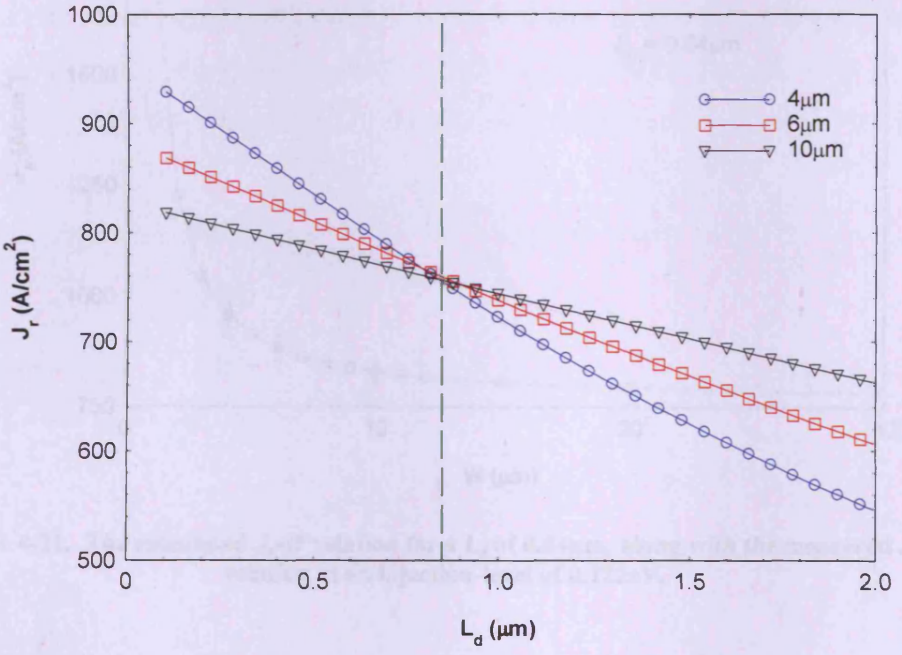

Figure 4-20. The J_r-L_d relation for the 10 (black triangles), 6 (red squares), and 4 μm (blue circles) ridges at an injection-level of 0.122eV and temperatures of 350K. The intercept of all three relations gives the lateral ambipolar diffusion length to be 0.84μm.

W (μm)	J_d (A/cm^2)	J_{rad} (A/cm^2)	J_{nr} (A/cm^2)	J_r (A/cm^2)	I_{out} (mA)
4.08	952.00	40.38	912.00	757.52	2.37
6.04	883.00	40.26	842.74	760.29	2.20
10.00	826.67	40.16	786.51	757.23	2.07

Table 4. Values for the measured W, J_d, J_{rad}, J_{nr} at an injection-level of 0.122eV and the calculated J_r and I_{out} using a L_d of 0.84μm.

In Figure 4-21, the modelled J_d-W relation for a 0.84μm L_d and J_r of $759 A/cm^2$ is given, along with the measured J_d-W relation at an injection-level of 0.122eV. It is

clearly evident from this comparison that the carrier diffusion model accurately explains the measured increase in threshold current density with decreasing ridge width and in doing so yields a good assessment of the lateral ambipolar diffusion length. Also from the modelled data, it can be seen that for very wide ridge widths, the carrier out-diffusion is approximately a constant and therefore does not influence the threshold current density behaviour with scaling of the ridge width.

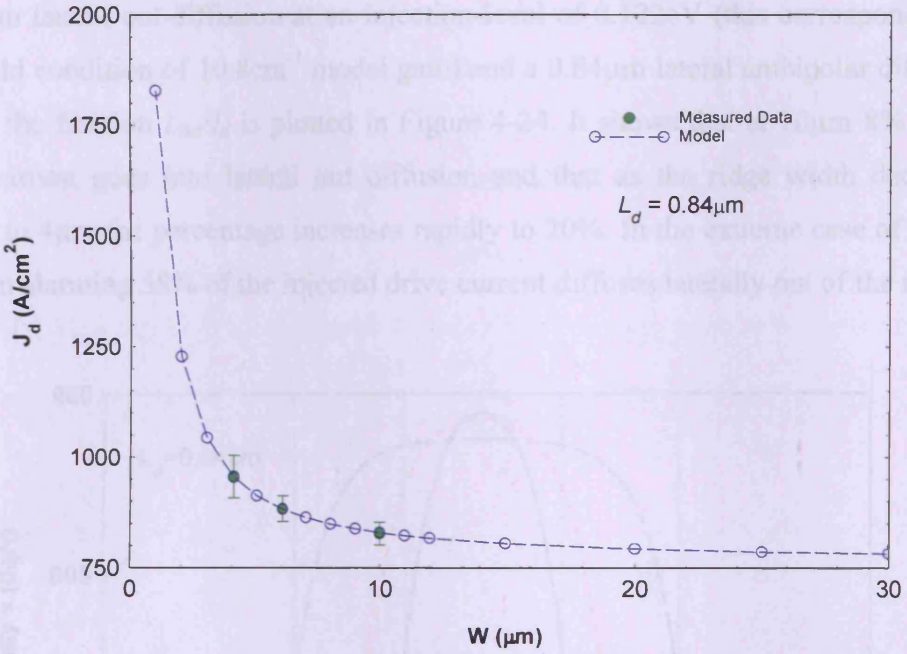

Figure 4-21. The calculated J_d-W relation for a L_d of 0.84μm, along with the measured J_d-W relation at an injection-level of 0.122eV.

In Figure 4-22, the lateral carrier density profile of the fitted model for the 4, 6 and 10 μm ridges are illustrated as normalised functions. The 10μm ridge has a carrier density profile that is fairly uniform across most of its width. However, as the ridge width gets narrower, the non-uniformity of carrier density profile increases. This effect is illustrated in the distributions of the 4 and 6 μm ridges. The overall result of this change with decreasing ridge width is that the fraction of carriers outside of the ridge compared to that inside of the ridge increases. Therefore a higher drive current density is required to achieve the same current density average beneath the ridge and, hence, concomitant radiative current density. Conversely however, for ridge widths which are much greater than L_d, the carrier density distribution is mainly uniform across the lateral extent of the ridge, and the out-diffusion distribution is

approximately the same. In this case, there is approximately no threshold dependence on ridge width as a result of an increasing carrier out-diffusion effect. To illustrate this explanation, equation (4.9) has been solved as a function of ridge width and is plotted in Figure 4-23. The figure clearly has two distinct regions: one covers a range of ridge widths roughly wider than 10μm in which I_{out} is approximately invariant of ridge width; and the other covers a range roughly below 10μm in which I_{out} increases rapidly with decreasing ridge width. To demonstrate the fraction of drive current that is lost to lateral out-diffusion at an injection-level of 0.122eV (this corresponds to a threshold condition of 10.8cm^{-1} modal gain) and a 0.84μm lateral ambipolar diffusion length, the fraction I_{out}/I_d is plotted in Figure 4-24. It shows that at 10μm 8% of the drive current goes into lateral out diffusion and that as the ridge width decreases further to 4μm the percentage increases rapidly to 20%. In the extreme case of a 1μm ridge an alarming 58% of the injected drive current diffuses laterally out of the ridge.

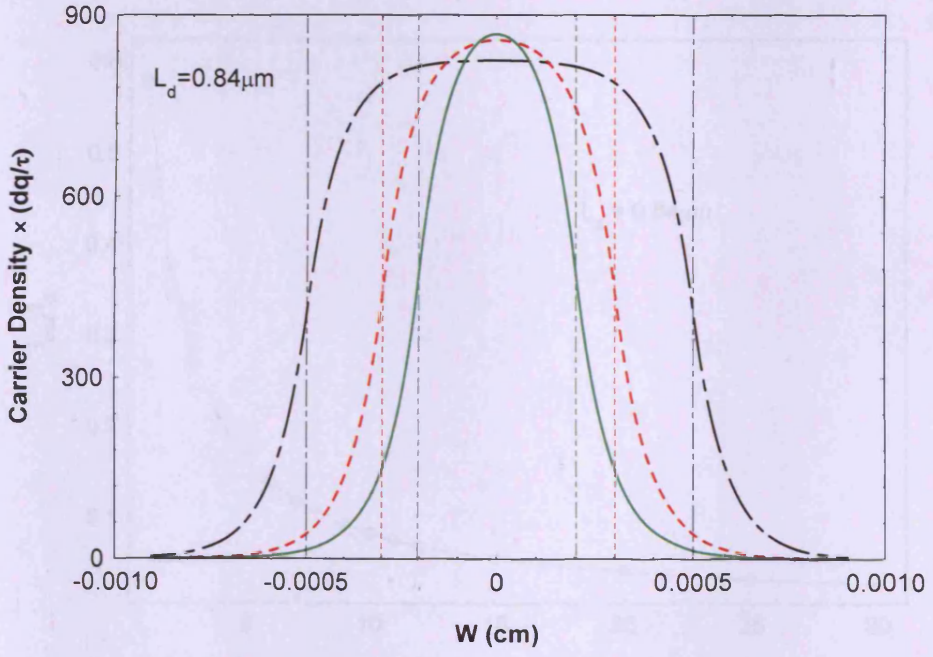

Figure 4-22. Calculated lateral carrier density profiles of the 4μm (solid green), 6μm (dashed red), and 10μm (dot-dashed black) ridge devices at a carrier injection-level of 0.122eV and an ambipolar diffusion length of 0.84μm.

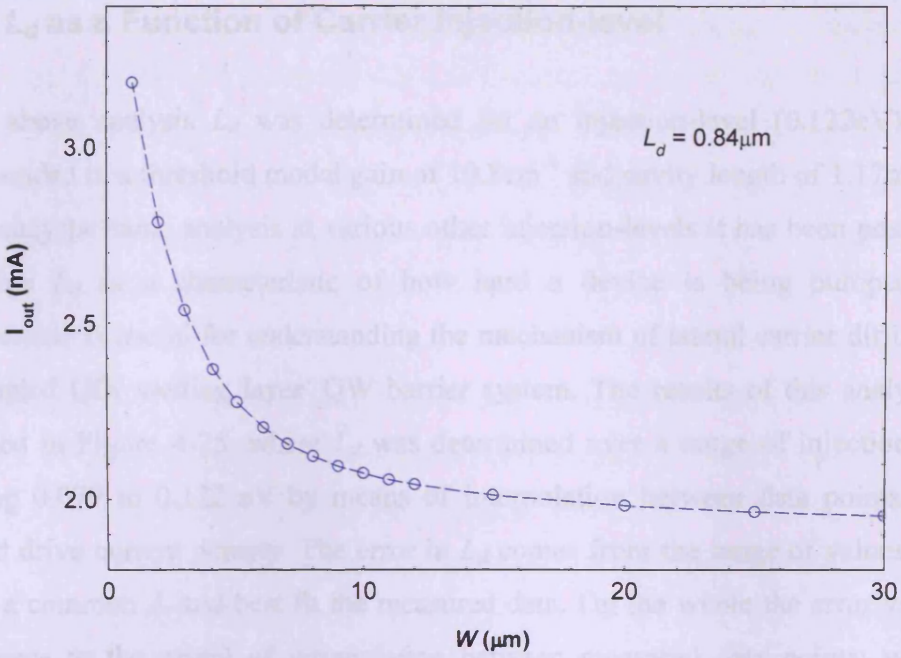

Figure 4-23. Lateral out-diffusion current, I_{out} dependence on ridge width, W for an L_d of 0.84μm

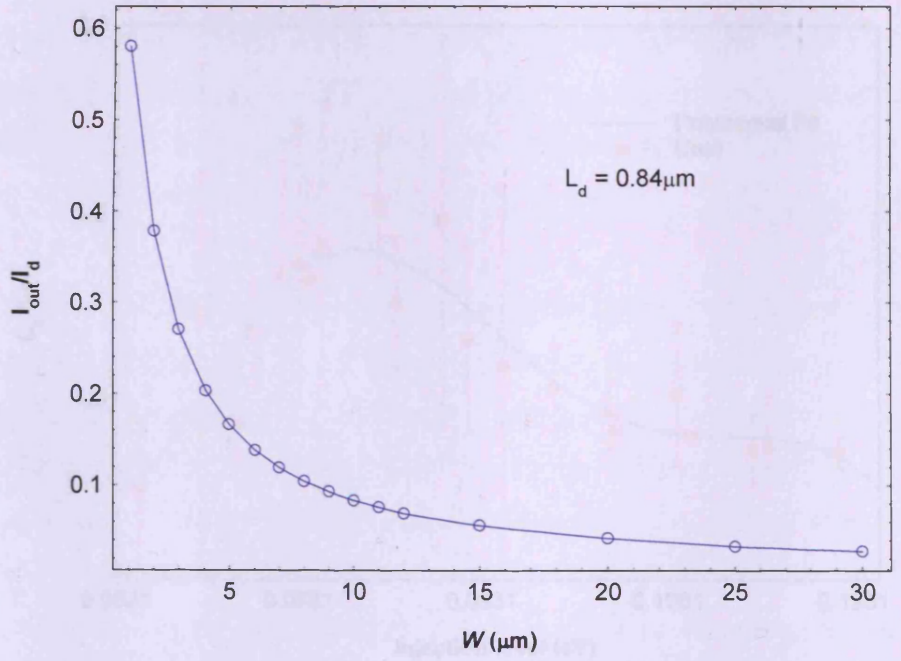

Figure 4-24. Fraction of the drive current (I_d) which goes into lateral out-diffusion current (I_{out}), I_{out}/I_d, as a function of ridge width (W) for a lateral ambipolar diffusion length (L_d) of 0.84μm.

4.5.3 L_d as a Function of Carrier Injection-level

In the above analysis L_d was determined for an injection-level (0.122eV) which corresponded to a threshold modal gain of 10.8cm^{-1} and cavity length of 1.17mm. By performing the same analysis at various other injection-levels it has been possible to determine L_d as a characteristic of how hard a device is being pumped. This characteristic is useful for understanding the mechanism of lateral carrier diffusion in the coupled QD/ wetting layer/ QW barrier system. The results of this analysis are presented in Figure 4-25, where L_d was determined over a range of injection-levels covering 0.079 to 0.122 eV by means of interpolation between data points of the injected drive current density. The error in L_d comes from the range of values which satisfy a common J_r and best fit the measured data. On the whole the error varies in accordance to the extent of interpolation between measured data points; with the smallest errors coinciding with closely matched data points.

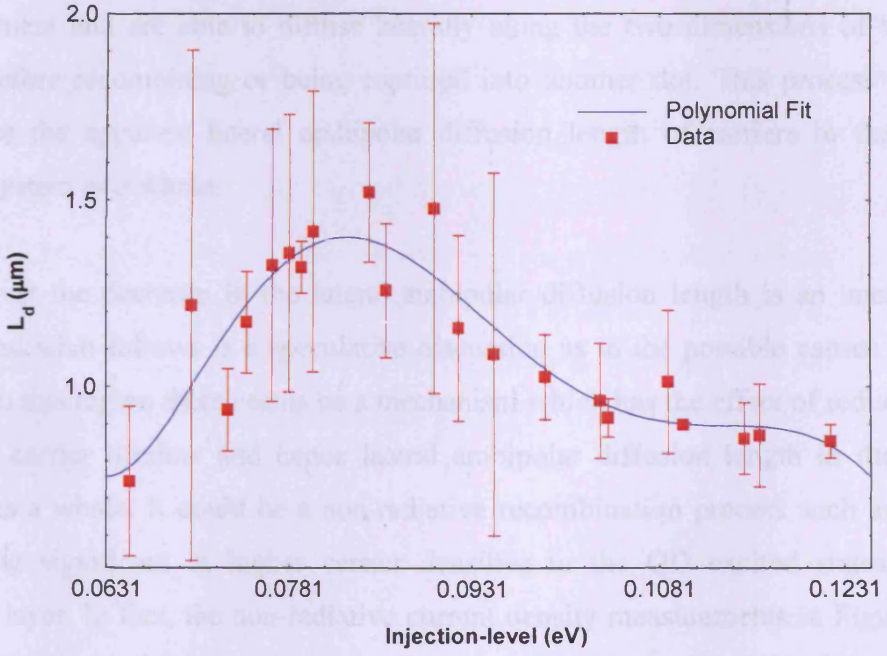

Figure 4-25. Estimated lateral ambipolar diffusion length (L_d) as a function of injection-level (ΔE_f-E_{trans}) in the quantum-dot active region at 350K.

The general trend of the L_d– *injection-level* characteristic seen in Figure 4-25 has two distinct regions:

- The first region is at low injection-levels where L_d appears to be increasing with increasing injection-level. The increase in L_d is approximately from 0.75μm to 1.5μm over an injection-level range 0.065eV to 0.084eV.
- At higher injection-levels there is an apparent decrease in the lateral ambipolar diffusion length. The decrease is approximately from 1.5μm to 0.85μm over the injection-level range 0.084eV to 0.122eV.

The increase in L_d with carrier injection-level is somewhat intuitive and can be explained as follows. As the device is driven harder, the quasi Fermi-level separation increases and the higher energy states of the quantum-dots get increasingly populated. Carriers in the excited states of the quantum-dots experience a smaller confining potential than those in lower states (carriers in the ground state will experience the highest confining potential) and when this confining potential is comparable to the thermal energy of the system, thermally assisted excitation into the wetting-layer can more readily occur. Once in the wetting-layer, carriers no longer experience a lateral confinement and are able to diffuse laterally along the two dimensions of the QW plane before recombining or being captured into another dot. This process thereby increases the apparent lateral ambipolar diffusion length of carriers in the active region system as a whole.

In contrast the decrease in the lateral ambipolar diffusion length is an unexpected result and what follows is a speculative discussion as to the possible causes for this effect. In this region there seems be a mechanism which has the effect of reducing the average carrier lifetime and hence lateral ambipolar diffusion length in the active region as a whole. It could be a non-radiative recombination process such as Auger becoming significant at higher carrier densities in the QD excited states and/or wetting layer. In fact, the non-radiative current density measurements in Figure 4-18 does show signs of this happening as J_{nr} has a higher order increase after a carrier injection-level of 0.084eV. Moreover, by determining the internal radiative efficiency (J_{rad}/J_d) as a function of carrier injection-level, as illustrated in Figure 4-26, it can be seen that below about 0.084eV the internal radiative efficiency gradually decreases for all of the ridge widths. And in this region the 10μm ridge is the most efficient which is not surprising since it has the least lateral out-diffusion current of the three

ridge widths. Beyond a carrier injection-level of 0.084eV there is a sharp decrease in the internal radiative efficiency with carrier injection-level for all of the ridge widths. In this region, the internal efficiencies of the three ridge widths converge closer together. Presumably the gradual decrease and relatively larger separation between the different ridge widths of their internal radiative efficiency is because of an increasing number of carriers thermally escaping out of the QD and contributing to the lateral diffusion of carrier out of the ridge boundaries. This process continues at higher injection-levels, but the increasing number of carrier in the QW like wetting-layer gives rise to a higher non-radiative recombination rate and therefore the average carrier lifetime in the wetting layer decreases and concomitantly the ambipolar diffusion length decreases. Consequently, although more carriers are thermally escaping out of the QD and into the wetting-layer, the reduced ambipolar diffusion length reduces the relative effect of carrier out-diffusion on ridge width.

In a QW, Auger recombination has an approximate cubic relation to the carrier density and therefore as the population in the wetting-layer increases, the rate of Auger recombination may also increase and cause the average carrier lifetime to decrease. This will thereby reduce the lateral ambipolar diffusion length which is given by $\sqrt{D_a \tau}$. Previous reports on the lateral ambipolar diffusion length in a InP-InGaAsP QW system found a strong reduction in L_d with increasing current injection. This recognition could imply that the observed reduction of L_d in this study is because the population of carriers in the QW wetting-layer has reached a point where any further increase in population results in a decrease of the average carrier lifetime and hence diffusion length.

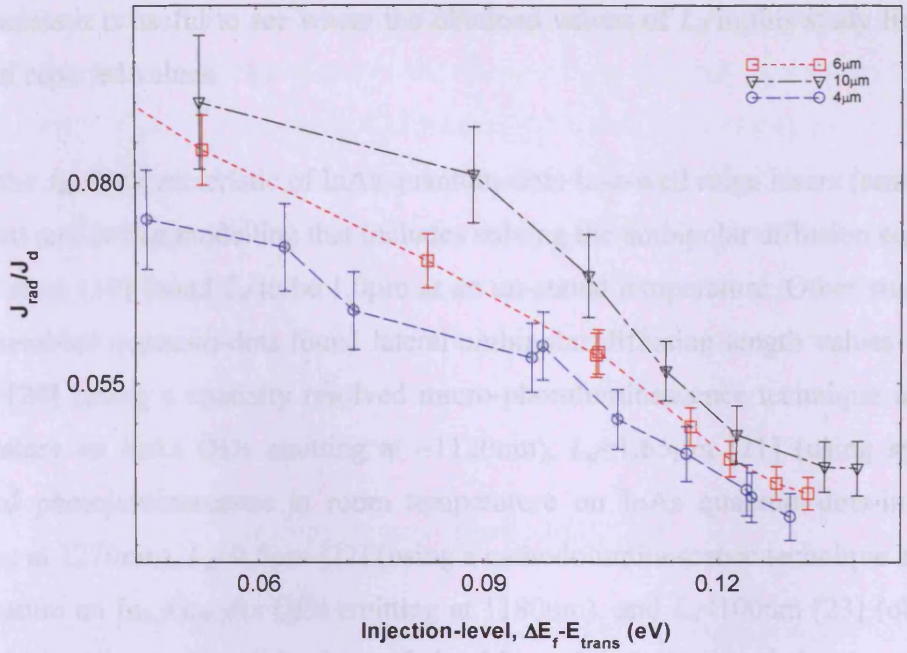

Figure 4-26. Internal radiative efficiency as a function of carrier-injection-level for the 10 (black triangles), 6 (red squares) and 4 (blue circles) μm ridges at 350K.

If the above interpretation is true, then it can be concluded that the expected reduction in L_d as a result of three-dimensional carrier confinement in quantum-dot material systems only occurs at low carrier injection-levels. At higher carrier injection-levels it is the increased non-radiative recombination rate that predominantly reduces L_d.

4.5.4 Comparisons with Other Studies

There are several reasons why it is difficult to relate the estimated values of L_d in the InAs quantum-dot-in-a-well material system obtained in this investigation at various carrier injection-levels (0.7μm – 1.5μm) to those reported in the literature:

- firstly the material system is not exactly the same
- secondly the measurements are not necessarily at the same temperature
- thirdly the measurements would have almost certainly been taken at different injected carrier densities
- and lastly changes in α_i and gain-mode overlap were not both taken into account in the previous studies

Nonetheless it is useful to see where the obtained values of L_d in this study lie in the range of reported values.

Using the J_{th}-W characteristic of InAs quantum-dots-in-a-well ridge lasers (emitting at 1280nm) and device modelling that includes solving the ambipolar diffusion equation, Moore *et al.* [19] found L_d to be 1.0μm at an un-stated temperature. Other studies on self-assembled quantum-dots found lateral ambipolar diffusion length values of $L_d \approx$ 6.5μm [20] (using a spatially resolved micro-photoluminescence technique at room temperature on InAs QDs emitting at ~1120nm), $L_d \approx$1.65μm [21] (using spatially resolved photoluminescence at room temperature on InAs quantum-dots-in-a-well emitting at 1270nm), $L_d \approx$0.5μm [22] (using a cathodoluminescence technique at room temperature on $In_{0.3}Ga_{0.7}As$ QDs emitting at 1180nm), and L_d<100nm [23] (obtained by analysing the scaling behaviour of the I-V and L-I characteristics in an InAs quantum-dot system emitting around 1300nm at room temperature under low injection-levels). In general the obtained values of L_d in this study are not that dissimilar to the previously reported values of similar structures. However, in this investigation we have ensured that the mechanisms of an increasing internal optical loss and deteriorating gain-mode overlap are not influencing the estimate.

In all of the reports, there is in general agreement that the lateral ambipolar diffusion length in material systems containing self-assembled quantum-dots is lower than in quantum-well systems. For example, Shaw *et al.* measured a factor of 1.46 reduction in ambipolar diffusion length for InAs quantum-dots (L_d = 6.5 μm) compared to InGaAs quantum-wells (L_d = 9.5 μm) at room temperature [20]. Fiore *et al.* measured a much greater reduction of at least a factor 27 for InAs quantum-dots (L_d < 100 nm) compared to InGaAs quantum-wells (L_d = 2.7 μm) [15]. Moore *et al.* measured a more intermediate reduction of a factor 5 for InAs quantum-dots (L_d = 1 μm) compared InGaAs quantum-wells (L_d = 5 μm) [21]. This suppressed diffusion is attributed to the three-dimensional carrier confinement in the low bandgap quantum-dot islands. The mechanism of lateral diffusion in such systems requires thermal escape out of the quantum-dot and into the quantum-well like wetting-layer where carriers can diffuse laterally along the 2D wetting-layer plane before either recombining or being captured into a neighbouring dot. However, in reference [21] it

has been suggested that the observed diffusion in quantum-dot systems occurs in the GaAs barrier prior to carrier capture into the quantum-dot. But in working devices, diffusion prior to capture is expected to be negligible due to the capture time from the barrier to the quantum-dots being smaller than 10ps [24]. The results of this study are in favour with the description of thermally-assisted diffusion via the wetting-layer. But in addition it suggests at high enough carrier injection-levels the observed lateral ambipolar diffusion length is mainly reduced because of a higher-order non-radiative recombination rate and hence reduced average carrier lifetime.

4.5.5 Limitation in the Model and Methodology

In the carrier diffusion model, it was necessary to assume a spatially invariant carrier lifetime (τ) across the width of the ridges. This is a common simplification often applied to the diffusion equation in order to obtain an analytical expression of the carrier density profile. Strictly speaking the carrier lifetime will vary across the lateral extent of the ridge because it is dependent on the local carrier density. Nevertheless, the resulting analytical solutions are still useful for clarifying the physical issues involved in the device performance and for facilitating the estimation of certain parameters despite not always being quantitatively exact. Given this recognition, the obtained diffusion length should be regarded as a measurable estimate describing the extent of the out-diffusion process in the active region of the sample rather than an exact value.

Another assumption of the model was that the injected drive current density is uniform within the boundaries of the ridge and zero elsewhere. This is partly justified because current spreading in the conductive upper cladding layers has been eliminated by etching the ridges to the interface of the waveguide. Lateral current spreading in the waveguide is expected to be negligible because it is undoped and therefore highly resistive, and also because the capture rate is fast and concomitantly the carrier lifetime is short in the waveguide.

It is possible that part of the threshold dependence on ridge width seen in Figure 4-12 is the result of a higher-order dependence of non-radiative recombination on the local

carrier density profile. However, for this to be significant the average non-radiative current density across the whole profile would have to show an increase. Moreover, highly non-uniform carrier density profiles are, in any case, the result of a significant fraction of drive current being lost to lateral out-diffusion. This was illustrated in Figure 4-22 and Figure 4-24. Therefore, the dominant cause of the threshold dependence with ridge width seen in Figure 4-12 will nevertheless be due to the lateral out-diffusion mechanism. If though, a quantitatively significant part of the threshold dependence did originate from the higher-order non-radiative recombination dependence on the local carrier density, then L_d in the analysis will be slightly overestimated.

4.6 Lateral Diffusion at 300K

Given that thermal re-emission from the quantum-dot to the wetting-energy ought to increase with increasing temperature, it would be reasonable to assume that decreasing the temperature will reduce the thermal re-emission. In this case fewer carriers will be escaping into the wetting layer and/or surrounding QW barrier material where lateral diffusion can occur. To see if this presumption is true, we performed the above experiment at 300 K. In Figure 4-27 we show the result for the non-radiative current density as a function of injection-level for the various ridge widths at 300 K.

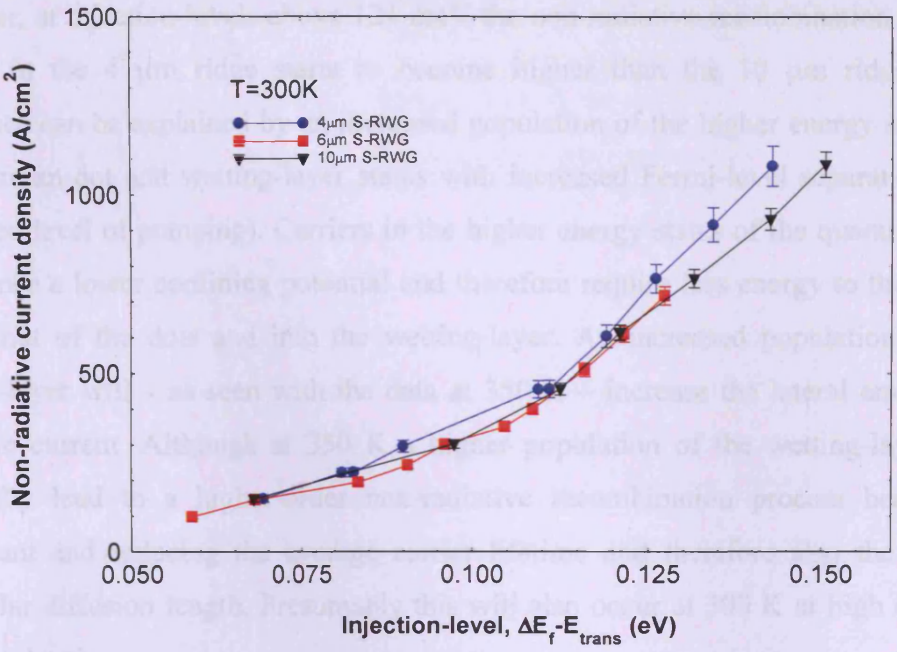

Figure 4-27. Non-radiative current density for the 10, 6, and 4 μm ridges as a function of injection-level, at 300K

Within the experimental uncertainty the difference between the non-radiative current density in the different ridge widths is negligible at given injection-levels below 121 meV. This implies that the loss of carriers to lateral out-diffusion is approximately the same in the different widths at 300 K. From the discussions in the previous sections, this behaviour is seen when the lateral ambipolar diffusion length is much smaller than the ridge width. Given that at 350 K a difference in non-radiative current density in the different ridge widths was observable for an ambipolar diffusion length of 0.75 μm, it therefore seems that the lateral ambipolar diffusion length must be less than 0.75 μm at 300 K at injection-levels below 121 meV. This result reveals that at lower temperatures the lateral carrier diffusion process is better inhibited by the three-dimensional confinement of the quantum-dots due to a reduced possibility of thermal escape out of the quantum-dots and into the wetting-layer where carriers can laterally diffuse. What is apparent from these results is that the lateral ambipolar diffusion length is significantly reduced by the zero-dimensionality of the material system. As such the quantum-dot material system can help further reduce the size of lasers for OEIC.

However, at injection-levels above 121 meV the non-radiative recombination current density in the 4 μm ridge starts to become higher than the 10 μm ridge. This difference can be explained by an increased population of the higher energy states of the quantum-dot and wetting-layer states with increased Fermi-level separation (i.e. increased level of pumping). Carriers in the higher energy states of the quantum dots experience a lower confining potential and therefore require less energy to thermally escape out of the dots and into the wetting-layer. An increased population of the wetting-layer will – as seen with the data at 350 K – increase the lateral ambipolar diffusion current. Although at 350 K a higher population of the wetting-layer did eventually lead to a higher-order non-radiative recombination process becoming significant and reducing the average carrier lifetime and therefore also the lateral ambipolar diffusion length. Presumably this will also occur at 300 K at high enough injection-levels.

4.7 Evaluation of Quantum-Dot Material Systems for Inhibiting Lateral Carrier Out-Diffusion

From the measurements in this study we have found that in S-K quantum-dot systems the lateral diffusion mechanism can be inhibited in one of two ways. Both these different ways are best illustrated by looking at the measurements of the lateral ambipolar diffusion length as a function of injection-level; shown in Figure 4-28.

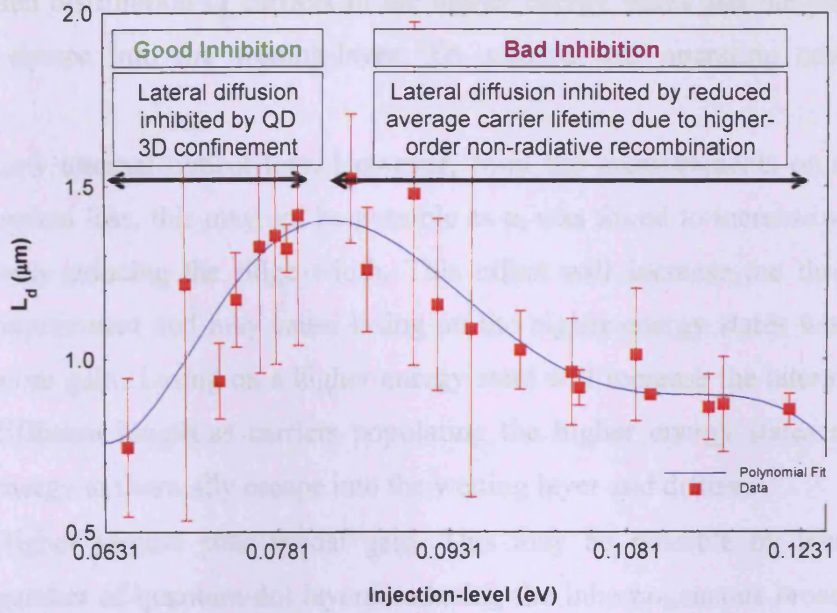

Figure 4-28. Lateral ambipolar diffusion length (L_d) as a function of injection-level (ΔE_f-E_{trans}) in the quantum-dot active region at 350K.

The good way of inhibiting lateral ambipolar diffusion and thus reducing the lateral out-diffusion mechanism, is by operating the device at low injection-levels where the carriers are injected into the lowest states of the quantum-dots. The three-dimensional carrier confinement in the quantum-dots will then restrict carriers from laterally diffusing.

The second way, which is a bad way, is to operate the device at high injection-levels where the higher-energy states of the quantum-dot and wetting-layer are significantly populated. In this region, the increased population of the wetting-layer leads to a higher non-radiative recombination rate which reduces the average carrier lifetime and therefore the ambipolar diffusion length. This method of reducing the lateral out-diffusion mechanism is at the expense of losing a higher fraction of carriers to other non-radiative recombination processes. Therefore the performance of the device will still degrade with further size reduction.

The best possible way of reducing the lateral out-diffusion mechanism and allowing further miniaturisation of S-RWG lasers, is to design the laser device to lase on the ground state and at low temperatures. Carriers in the ground state of the quantum-dot experience the greatest confining potential and operation at low temperatures reduces

the thermal distribution of carriers in the higher energy states and the probability of thermal escape into the wetting-layer. To achieve this operating condition will require:

- Low internal optical loss. However, from the measurements on the internal optical loss, this may not be possible as α_i was found to increase significantly with reducing the ridge width. This effect will increase the threshold gain requirement and may cause lasing on the higher-energy states where there is more gain. Lasing on a higher energy state will increase the lateral ambipolar diffusion length as carriers populating the higher energy states require less energy to thermally escape into the wetting layer and diffuse.
- Higher ground state modal gain. This may be possible by increasing the number of quantum-dot layers, reducing the inhomogeneous broadening, and reducing the non-radiative recombination.
- Reducing the mirror loss. But this then requires increasing the length of the S-RWG laser with reducing ridge width, which therefore defeats the aim of overall size reduction.

4.8 Conclusions

In the study presented in this chapter, the relative impact of the key mechanisms that influence the J_{th}-W characteristic of a S-RWG InAs quantum-dot structure have been quantitatively evaluated as a function of injection-level. These mechanisms involve an increasing internal optical loss and lateral out-diffusion current, and a deteriorating gain-mode overlap. Of particular merit is the estimation of the lateral ambipolar diffusion length as a function of injection-level from data that is only influenced by the lateral out-diffusion mechanism under high-level injection conditions (desirable for evaluating the diffusion process in a device under real working conditions), and therefore a more reliable result.

The conclusions are:

- The mechanism of an increasing internal optical loss changed significantly with ridge width and therefore its effect on the J_{th}-W characteristic has to be considered before attempting to model the threshold increase with the lateral

out-diffusion model. The quantitative increase with respect to the 10μm ridge was by a factor of 1.3 and 2.3 for the 6 and 4 μm ridges respectively.

- A negligible deterioration occurred in the gain-mode overlap over the range of ridge widths analysed. This result is not necessarily to say, however, that the impact of a deteriorating gain-mode overlap will not be significant for much narrower ridges. At some point beyond the experimental range of this investigation (i.e. < 4 μm) there ought to be a significant increase in threshold as a result of this effect [13, 15].
- By directly comparing the different ridge widths at a common operating point, the mechanism of carrier out-diffusion was found to have a significant impact of the threshold dependence with ridge width. As an example, the drive current density required to operate at an injection-level of 0.122eV with respect to the 10μm ridge was found to increase by a factor of 1.07 and 1.14 for the 6 and 4 μm ridges respectively.

Additionally, by determining the drive current density dependence with ridge width at a common operating point as a result of the out-diffusion mechanism only, it was possible to estimate the lateral ambipolar diffusion length by fitting a lateral carrier diffusion model to the data. Importantly this estimate is not influenced by the other key mechanisms. Depending on the carrier injection-level, the values of L_d at 350 K ranged from (0.75μm – 1.5μm).

Evaluating L_d as a function of carrier injection-level at 350 K revealed two distinct regions of operation: One was at carrier injection-levels below about 0.08eV where L_d was observed to increase with carrier injection-level. This was attributed to an increase in the number of carriers thermally escaping out of the dot and into the wetting-layer where they can laterally diffuse along the wetting-layer plane. The other region was at carrier injection-levels above about 0.08 eV where L_d decreased with increasing carrier injection-level. This region coincided with a higher-order non-radiative recombination current density occurring with increasing injection-level, and also a sharp decrease in the internal efficiency. As such, the decrease in L_d in this region was attributed to an apparent increase of the non-radiative recombination rate

in the wetting-layer with increasing carrier density and as a result an average carrier lifetime and concomitant lateral ambipolar diffusion length decrease.

Measurements at 300 K revealed an improvement in the carrier localisation such that no increase in the non-radiative current density was observed between the 10, 6 and 4 μm ridges at injection-levels below 121 meV. This effect was attributed to the reduced thermal re-emission of carriers from the quantum-dot to the wetting-layer where they can laterally diffuse.

These findings illustrated the significant effect three-dimensional carrier confinement in quantum-dots can have in inhibiting lateral out-diffusion and as such how quantum-dot material systems are suitable candidates for facilitating further miniaturisation of laser devices for use in OEIC.

[1] B. W. Hakki, "Carrier and gain spatial profiles in GaAs stripe geometry lasers," Journal of Applied Physics, 44, 11 p5021-5028, 1973.
[2] W. Joyce, "Carrier transport in double-heterostructure active layers," Journal of Applied Physics, 53, p 7235-7239. 1982.
[3] S. Y. Hu, S. W. Corzine, K.-K. Law, D. B. Young, A. C. Gossard, L. A. Coldren, and J. L. Merz, "Lateral carrier diffusion and surface recombination in InGaAs/AlGaAs quantum-well ridge-waveguide lasers," Journal of Applied Physics, 76, 8, p4479-4487. 1994.
[4] G. Adolfsson, S. Wang, M. Sadeghi,, J. Bengtsson, A. Larsson, J. J. Lim, V. Vilokkinen, P. Melanen, " Effects of lateral diffusion on the temperature sensitivity of the threshold current for 1.3μm double quantum-well GaInNAs-GaAs lasers," IEEE Journal of Quantum Electronics, 44, 7, p607-616. 2008
[5] H. Wenzel, G. Erbert, A. Knauer, A Oster, K. Vogel and G. Trankle, "Influence of current spreading on the transparency current density of quantum-well lasers," IOP Semiconductor Science and Technology, 15, p557-560, 2000.
[6] C. Y. Liu, Y. Qu, S. Yuan and S. F. Yoon, "Optimization of ridge height for the fabrication of high performance InGaAsN ridge waveguide lasers with pulsed anodic oxidation," Applied Physics Letters, 85, 20, p4594. 2004.
[7] K. K. Lee, D. R. Lim, H.-C. Luan, A. Agarwal, J. Foresi, and L. C. Kimerling, "Effect of size and roughness on light transmission in a Si/SiO_2 waveguide: Experiments and Model," Applied Physics Letters, 77, p1617-1619, 2000.
[8] D. Liang, J. Wang, J. –T. Huang, J. Yeh, L. Mawst and D. Hall, "Deep-etched native-oxide-confined high-index-contrast AlGaAs heterostructure lasers with 1.3μm dilute-nitride quantum wells," IEEE Journal of Selected Topics in Quantum Electronics, 13, 5, p1324-1331, 2007.
[9] R. K. Price, V. B. Verma, V. C. Elarde, and J. J. Coleman, "Internal loss, modal characteristics, and bend loss of asymmetric cladding ridge waveguide lasers at 850nm," Journal of Applied Physics, 103, 013108, 2008.
[10] L. A. Coldren and S. W. Corzine, "Diode lasers and photonic integrated circuits," Wiley Series in Microwave and Optical Engineering, 1995.
[11] M. G. A. Bernard and G. Duraffourg, "Laser conditions in semiconducors," Phys. Status Solidi, 1, p 669-703, 1961.
[12] G. Belenky, L. Shterengas, C. Lewis Reynolds, Jr., M. W. Focht, M. S. Hybertsen, B. Witzigmann, "Direct Measurement of Lateral Carrier Leakage in 1.3-μm InGaAsP Multiple-Quantum-Well Capped Mesa Buried Heterostructure Lasers," IEEE Journal of Quantum Electronics, 39, 9, p1276, 2002.
[13] E. Kapon, "Threshold current of extremely narrow semiconductor quantum-well lasers," Optics Letter, Vol. 15, No. 14, 1990.
[14] J. S. Osinski, , K. M. Dzurko, S. G. Hummel, and P. D. Dapkus, "Optimization of stripe width for low-threshold operation of quantum well laser diodes," Applied Physics Letters, 56, 25, p2487, 1990.
[15] U. T. Schwartz, M. Pindl, E. Strum, M. Furitsch, A. Leber, S. Miller, A. Lell, and V. Harle, "Influence of ridge geometry on lateral mode stability of (Al,In)GaN laser diodes," Phys. Status Solidi (a), 202, No. 2, p261-270, 2005.
[16] S. Y. Hu, D. B. Young, A. C. Gossard, and L. A. Coldren, "The effects of lateral leakage current on the experimental gain/current-density curve in quantum-well ridge waveguide lasers," IEEE Journal of Quantum Electronics, 30, 10, p2245-2250, 1994.
[17] W. T. Tsang, "The effects of lateral current spreading, carrier out-diffusion, and optical mode losses on the threshold current density of GaAs-$Al_xGa_{1-x}As$ stripe geometry DH lasers," Journal of Applied Physics, 49, 3, p1031-1044, 1978.
[18] G. J. Letal, J. G. Simmons, J. D. Evans and G. P. Li, "Determination of active-region leakage currents in ridge-waveguide strained-layer quantum-well lasers by varying the ridge width," IEEE Journal of Quantum Electronics, 34, 3, p512-517, 1998.
[19] S. A. Moore, L. O'Faolain, M. A. Cataluna, M. B. Flynn, M. V. Kotlyar and T. F. Krauss, "Reduced surface sidewall recombination and diffusion in quantum-dot lasers," IEEE Photonics Technology Letters, 18, 17, p1861-1863, 2006.
[20] A. Shaw,.H. Folliot, and J. F. Donegan, "Carrier diffusion in InAs/GaAs quantum dot layers and its impact on light emission from etched microstructures," IOP Nanotechnology, 14, p571-577, 2003.
[21] D. P. Popescu, P. G. Eliseev, A. Stintz, and K. J. Malloy, "Carrier migration in structures with InAs quantum dots," Journal of Applied Physics, 94, 4, p2454-2458, 2003.

[22] J. K. Kim, T. A. Strand, R. L. Naone, and L. A. Coldren, "Design parameters for lateral carrier confinement in quantum-dot lasers," Applied Physics Letters, 74, 19, p2752-2754, 1999.
[23] A. Fiore, M. Rossetti, B. Alloing, C. Paranthoen, and J. X. Chen, "Carrier diffusion in low-dimensional semiconductors: A comparison of quantum wells, disordered quantum wells, and quantum dots," Physical Review B, 70, 205311, 2004.
[24] A. Fiore, P. Borri, W. Langbein, J. M. Hvam, U. Oesterle, R. Houdre, R. P. Stanley, and M. Ilegems, "Time-resolved optical characterisation of InAs/InGaAs quantum dots emitting at 1.3μm", Applied Physics Letters, 76, p3430, 2000.

Chapter 5: Characterisation of Surface Recombination in Deep-Etched InGaAs Quantum-Well Ridges

5.1 Introduction

As devices such as deep-etched ridge waveguide lasers (D-RWG) and vertical-cavity-surface-emitting lasers (VCSELs) are scaled down in size (desired for such things as lowering the threshold current, increasing the modulation speed and for mode control), their threshold performance becomes severely limited by non-radiative surface recombination at the exposed sidewalls of the active region. At the exposed surface, unmatched bonds in the crystal lattice give rise to energy states in the bandgap of the active region (surface-states). Such surface-states are undesirable in semiconductor light emitting devices as they provide a non-radiative carrier recombination path. The recombination mechanism is analogous to the monomolecular defect recombination process. However the surface recombination mechanism is usually parameterised by a surface recombination velocity (v_s) rather than a lifetime.

In the literature, studies of surface recombination have mainly focussed on quantifying v_s and the lateral ambipolar diffusion length for a given material system. The techniques used to do this have varied from; spatially-resolved photoluminescence [1], cathodoluminescence, and device modelling of threshold dependence with ridge width (this was discussed in Chapter 4). Based on such studies (which are not necessarily under high-level injection conditions), reports have often attributed an increase in threshold current density with device size reduction in D-RWG and VCSELs to an increase in non-radiative surface recombination current. However, to the best of our knowledge, the increase in non-radiative recombination which should arise from this process has not yet been measured or quantified under high injection-level conditions. Nor for that matter has the increase in non-radiative current actually been confirmed to originate from surface recombination. Furthermore, the effect surface recombination has on the lateral non-uniformity of the gain producing carrier density distribution and consequentially gain-mode overlap has not been experimentally studied. This effect may be important as it can contribute to the

observed threshold increase. In addition, studies on the surface recombination velocity (although useful) lack insight into the overall effect surface recombination has on the internal quantum efficiency.

In this study, the multisection technique is utilised on quantum-well D-RWG structures of varying widths to fully characterise the increasing effect surface recombination has with decreasing ridge width. This is done by determining the non-radiative current density, radiative current density, modal gain and internal quantum efficiency as a function of ridge-width and carrier injection-level. By analysing these trends the study looks into: the causes of the J_{th}-W characteristic; the possible deterioration in the gain-mode overlap; the dependence of radiative current density at threshold on ridge width. It also quantifies the increase in non-radiative current density with decreasing ridge width; provides evidence that the increase in non-radiative current density originates from surface recombination; quantifies the change in internal quantum efficiency; and illustrates the change in these characteristics as a function of laser length.

The chapter begins by detailing the material system and device structure before presenting the laser threshold current and current density characteristics as a function of ridge width for 1.5 mm length lasers. Characterisation of the gain in the various ridge widths then follows and the effects of the internal optical loss and gain-mode overlap are analysed as a function of ridge width. This is followed by a detailed characterisation of radiative and non-radiative recombination mechanisms. In that section the increase in non-radiative current as a result of surface recombination is quantified and also shown to follow the expected power law dependence with carrier density. Furthermore the recombination process is also shown to follow the expected surface to volume ratio dependence. After this the internal quantum efficiency is measured and quantified as a function of ridge width. Finally the measured data is used to determine the characteristics of all these parameters as a function of laser length.

5.2 QW Material & Device Structure

The sample used in this investigation is a multiple quantum-well (MQW) heterostructure grown by solid source molecular beam epitaxy. It essentially has the same layer sequence as the InAs/$In_{0.15}Ga_{0.85}As$ quantum-dot DWELL sample studied in Chapter 4 apart from the active region which consists of three 8nm $In_{0.15}Ga_{0.85}As$ quantum-well layers without InAs quantum-dots: The three quantum-well layers are separated by 50nm GaAs spacer layers, and are embedded in a GaAs/AlGaAs waveguide core. The p-type and n-type cladding layers are 1.5μm of $Al_{0.4}Ga_{0.6}As$ doped with 5E17 cm^{-3} with Be and 2E18 cm^{-3} with Si, respectively. The layer sequence is capped with a 300nm *p*+ GaAs layer.

In order to study the performance limiting mechanism of lateral carrier diffusion to surface-states in structures with exposed QW surfaces, a series of different ridge width D-RWG lasers and multisection test-structures were fabricated in a single process run. The ridge widths ranged from 29 to 1.86 μm. The fabrication procedure is the same as that described in Chapter 3 with the only tailored specification being: the ridges are etched through the active region to an etch depth of 200 nm into the lower cladding layer. Etching through the active region exposes the QW surface and thereby creates surface-states through which some fraction of injected carriers will recombine non-radiatively. However since the etched areas are planarised and insulated with BCB, the extent of the non-radiative surface recombination may be reduced. This is because BCB is said to passivate the sidewalls and thereby reduce the surface-states. As such the effect of surface recombination in devices with no passivation may then be even worse than that reported here. Figure 5-1 illustrates the ridge profile and the coordinate system used throughout this study. The as-cleaved and uncoated bars were mounted p-side up onto copper blocks using silver epoxy for temperature controlled measurements at 300K. The actual values of the ridge widths were measured by scanning electron microscopy (SEM).

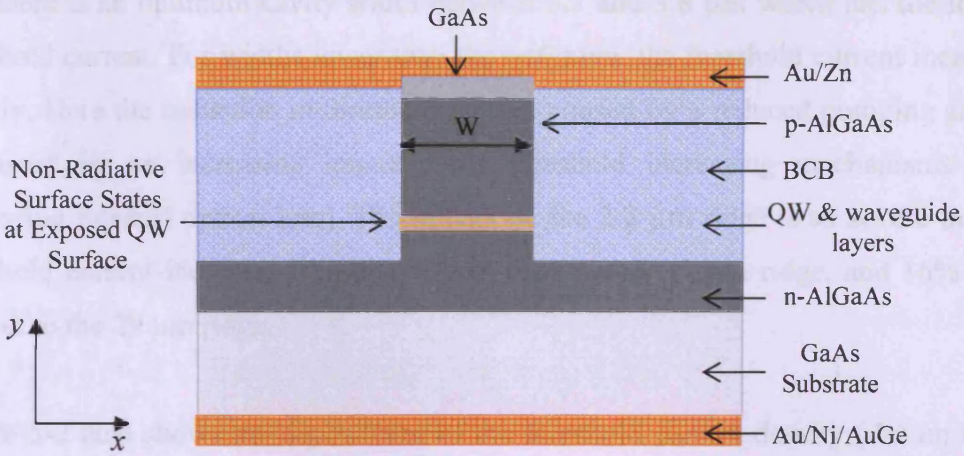

Figure 5-1. Schematic of the D-RWG QW profile

5.3 Experimental Results

5.3.1 Laser Threshold Dependence on Ridge Cavity Width

The measured dependence of the threshold current (I_{th}) on ridge width (W) for uncoated facet D-RWG lasers is shown in Figure 5-2. The cavity length of the lasers is 1.5 mm. All of the ridge cavity widths were found to be lasing with TE polarised light. From the mirror loss of the cavity ($\alpha_m = ln(1/R)/L$) the threshold net modal gain (G-α_i) is calculated to be 8.5 cm^{-1}. For this calculation a facet reflectivity (R) of 0.28 was determined from the effective index of the fundamental mode. From waveguide simulations of the modes in these devices it can be shown that the change in effective index with ridge width is very small and the resulting change in reflectivity is negligible. In this study it will therefore be assumed that the change in facet reflectivity with W is negligible.

The I_{th}-W characteristic shows that in reducing W from 29 to 5.7 μm the threshold current drops by approximately 22%. This drop is consistent with a reduced pumping area requiring less current for a given transparency current density [2, 3]. Further reduction of W to 3.8 μm results in no change of the threshold current. This implies

that there is an optimum cavity width between 5.7 and 3.8 μm which has the lowest threshold current. For widths lower than the optimum, the threshold current increases rapidly. Here the reduction in threshold current caused by a reduced pumping area is surpassed by an increasing impact from threshold increasing mechanisms (e.g. increasing internal optical loss). The impact on the 2.8 μm ridge is so severe that its threshold current increases by 48% with respect to the 5.7 μm ridge, and 16% with respect to the 29 μm ridge.

Figure 5-2 also shows the dependence of the threshold current density (J_{th}) on ridge width. Over the range where the threshold current decreased, the threshold current density increases by a factor of approximately 3.9 with respect to the 29 μm ridge. Therefore it can be said that threshold increasing mechanisms are having some impact in this range; however their overall threshold current increasing effect does not exceed the threshold current reduction experienced by a reduced pumping area. Had there been no effect from threshold increasing mechanisms, then J_{th} would have remained the same and I_{th} would have decreased even further. Over the region where the threshold current increases rapidly with decreasing ridge width, J_{th} also increases rapidly. Increase for the 3.8 and 2.8 μm ridges are a severe ×5.7 and ×12.0 with respect to the 29 μm ridge.

In Chapter 4 it was discussed that the key mechanisms that can cause an increase in threshold with decreasing ridge width are: an increasing internal optical loss (α_i), deteriorating gain-mode overlap, and an increasing lateral carrier out-diffusion current.

In the QW D-RWG devices, the mechanism of lateral out-diffusion is prevented by etching through the active region. This however causes the problem of non-radiative carrier recombination via surface-states at the exposed QW surface (surface recombination). The current associated with this might be as bad as or even worse than the loss of carriers due to an out-diffusion current. The implications of an increasing surface recombination current on device performance are clear: threshold currents will be increased, and efficiencies reduced.

From the analysis of the threshold data alone, it is not possible to attribute the cause of the threshold increase to any one of the key mechanisms. However, the lasing wavelength data presented in Table 5 does indicate that the optical losses in the system might not be changing significantly with W as the lasing wavelength is approximately the same (974 ± 1 nm). The actual lasing wavelength depends on the quasi Fermi-level separation which in turn depends on the carrier density at threshold. As the threshold condition and hence carrier density at threshold is increased, the quasi Fermi-level separation increases with band filling and the lasing wavelength shifts to higher photon energies [4]. Since the lasing wavelength is not observed to decrease with decreasing W, it is indicated that the losses in system might not be changing. To order to confirm this, further analysis is required to assess the relative impact of each key mechanism on the J_{th}-W characteristic. This will be done in the following sections through utilising the multisection characterisation technique as was done in Chapter 4.

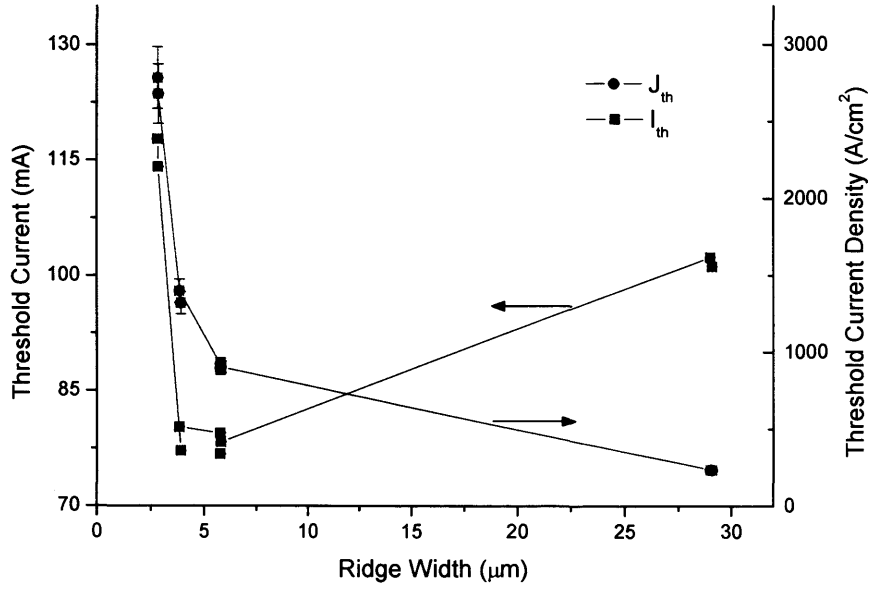

Figure 5-2. Measured laser threshold current dependence on ridge width, I_h-W (black squares) and laser threshold current density dependence on ridge width, J_{th}-W (blue circles).

Table 5. Measured lasing wavelength of the different ridge cavity width 1.5mm D-RWG lasers at 300K

Ridge Cavity Width (μm)	Lasing Wavelength (nm)
29.1	973
29.2	974
5.8	975
5.8	972
5.7	974
3.9	974
3.8	974
2.8	975
2.8	975

5.3.2 Gain Measurements

In this section, gain spectra measurements on each ridge width are used to quantify the impact a changing α_i and gain-mode overlap mechanism have on the laser threshold behaviour with ridge width (W).

Measurements of gain were done by analysing the ASE from the D-RWG multisection test structures as a function of pumped amplification length. The details of the technique are described in Chapter 2. An example of the TE net modal gain spectra (G - α_i) obtained from the 29 μm D-RWG at 300K is plotted in Figure 5-3 for a range of injected drive current densities (J_d). The net modal loss spectrum is also included for comparison.

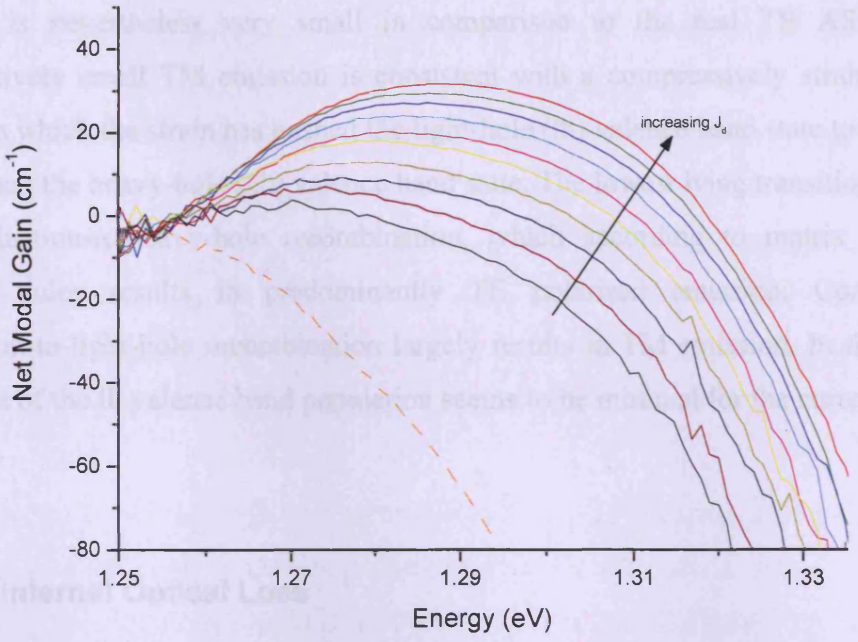

Figure 5-3. Measured TE net modal gain spectra for the 29μm ridge at 300K for injected drive current densities ranging from 229.1 (black) - 435.3 (red) A/cm^2. The modal loss spectrum is also shown (dashed line).

Over the analysed range of J_d, the region of gain is centred around a gain peak of approximately 1.29eV. This value is also approximately where the transition energy is - as determined by the point where the absorption is half of the first subband peak absorption. The lack of prominent features from higher energy subband transitions indicates that the region of gain is produced from transitions in the first subband of the quantum-well and that higher subbands are not significantly populated over the experimental range of injected drive current densities. It is also apparent that the gain over this range has not saturated and therefore the subband has not been fully inverted.

Measurements of the TM ASE consisted of light that corresponded in wavelength to the peak TE ASE and this had a peak intensity of at least a factor 180 less than the measured peak TE. Such observations of a TM measurement at the same wavelength as the TE signal can occur with leakage through the polariser. Some leakage is expected in the experiment because of the finite extinction ratio of the polariser (which is >100,000:1) and also because in practise it is difficult to obtain an ideal collection geometery where the extinction axis of the polariser is precisely orthogonal

to the TM light. If any real TM emission is measured it is obscured by the leakage of TE and is nevertheless very small in comparison to the real TE ASE. Such comparatively small TM emission is consistent with a compressively strained QW sample in which the strain has pushed the light-hole (lh) valence band state to a higher energy than the heavy-hole (hh) valence band state. The lowest lying transition is then the conduction-to-heavy-hole recombination, which according to matrix element selection rules results in predominantly TE polarised emission. Conversely, conduction-to-light-hole recombination largely results in TM emission. In this case, the extent of the lh valence band population seems to be minimal for the current range studied.

5.3.2.1 Internal Optical Loss

At low photon energies, where there is zero gain and zero absorption, the net gain ($G - \alpha_i$) and loss spectra ($A + \alpha_i$) tend to the value of the internal optical loss (α_i). The internal optical loss dependence on the ridge width of the D-RWG devices is shown in Figure 5-4. Since α_i does not exhibit a systematic change with J_d and is not expected to, the plotted α_i values are the mean of all the current densities analysed for a particular ridge width and the error is given by the standard deviation.

In Chapter 4 the internal optical loss of the S-RWG structures was found to increase with reducing the ridge width from 10 to 4 μm. This is clearly not the case for the D-RWG structures. Over the same range of ridge widths, Figure 5-4 shows α_i changes negligibly within the experimental error. This invariance continues until the ridge width is reduced to 2.8 μm and as such the apparent threshold dependence on ridge width seen in Figure 5-2 is not the result of an increase in the internal optical loss. This was suggested previously with the invariance of the lasing wavelength with ridge width (c.f. Table 5); but those measurements alone were not conclusive since the change in wavelength with modal gain may not have been large.

However, had the range of threshold measurements been extended to 1.9 μm, then an increase in α_i (by a factor of 3.8 with respect to the 2.8 μm) would have contributed towards an increase in J_{th}. The large increase in α_i for the 1.9 μm width is attributed to

a significant increase of the wave amplitude at the rough sidewalls of the ridge which consequently increases the scattering losses [5] [6] [7]. Roughness in the sidewall is caused by imperfect fabrication processes in the lithography (due to the finite resolution), lift-off (serrated mask transferral) and dry etching (etch damage). The lack of a change in α_i for widths greater than 2.8 μm indicates very small wave amplitude at the sidewall occurs. Consequently it can be said that the internal optical loss in this region is mainly limited by the other causes of optical loss: free carrier absorption within the active region, absorption outside the active region and the scattering off rough interfaces in the material system [8].

The difference between the internal optical loss dependence on ridge width in the S-RWG and D-RWG type structures is attributed to the stronger optical confinement from the higher index-contrast in the D-RWG [5]. The implication of this is that the ridge width can be made much narrower in the D-RWG structure before scattering losses from the interaction of the wave amplitude with the rough sidewalls significantly increases. However, once a significant interaction of the wave amplitude and rough sidewalls does occur, the scattering loss in D-RWG structures is much more strongly affected. This is apparent by the large jump in the optical loss seen in the 1.9 μm width D-RWG. Since the behaviour of the internal optical loss dependence on ridge width is different between the S-RWG and D-RWG structures, the relative impact of only this mechanism on their threshold current density dependence with ridge width will be different: the threshold of the D-RWG will be affected at much narrower widths than the S-RWG, but when it is affected the threshold will increase with decreasing ridge width at a much faster rate. From this result, D-RWG can be scaled-down further in size before the threshold current density increases. However, other mechanisms can affect this advantage. In the analysis that follows I will look into the effects of the gain-mode overlap mechanism and surface recombination mechanism on the threshold behaviour with ridge width reduction for this D-RWG structure.

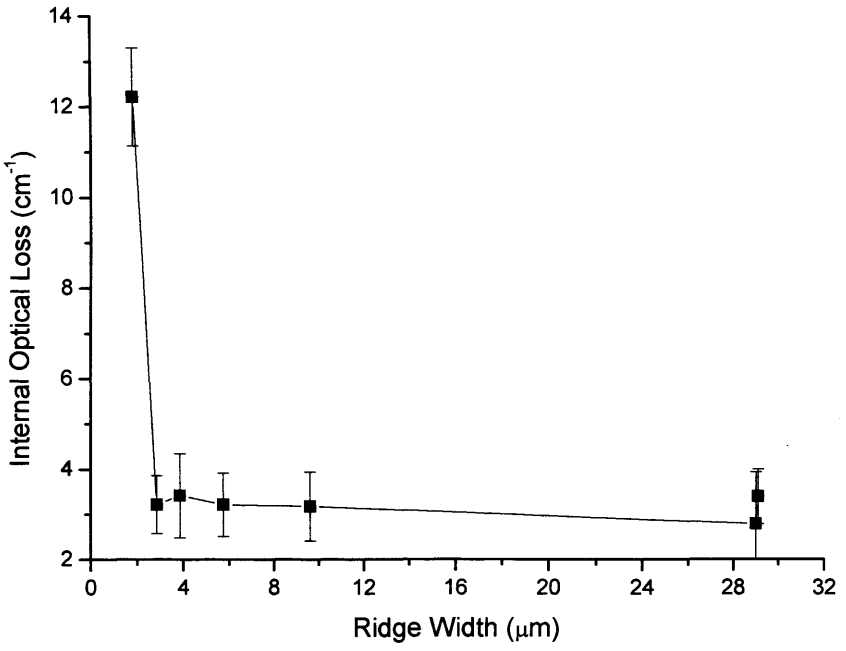

Figure 5-4. The dependence of the internal optical loss (α_i) on ridge cavity width (W)

5.3.2.2 Modal Gain Dependence on W

Measurements of the peak net modal gain as a function of current density for the various ridge widths are given in Figure 5-5. It reveals that if the ridge width is reduced a higher current density will be required to generate a given net modal gain. To help interpret this, Figure 5-6 compares the modal gain spectra for the 9.6, 5.8 and 3.9 μm ridges at the same J_d within error of 1180 A/cm^2. It shows that the wider widths are pumped more strongly as the gain bandwidth is wider, and the peak gain maximum and transparency point are shifted to higher energies. This reveals that as the ridge widths get narrower an increasing fraction of current is not going to pump the active region. In the latter sections of this chapter this increasing fraction of 'ineffective' current will be investigated further and be shown as an increase in non-radiative surface recombination.

The outcome of Figure 5-5 was also implied by the laser threshold measurements in the previous section. Those measurements were of 1.5mm lasers with uncoated facets and a threshold net modal gain requirement of 8.5 cm^{-1}. We can compare the laser

threshold data to the multisection data by using Figure 5-5 to determine the current density of the various ridge widths at the same net modal gain of 8.5 cm^{-1}. This comparison is given in Figure 5-7 and it reveals that the multisection gain data accurately matches the laser threshold data, thereby providing confidence in the measuring technique and measured data.

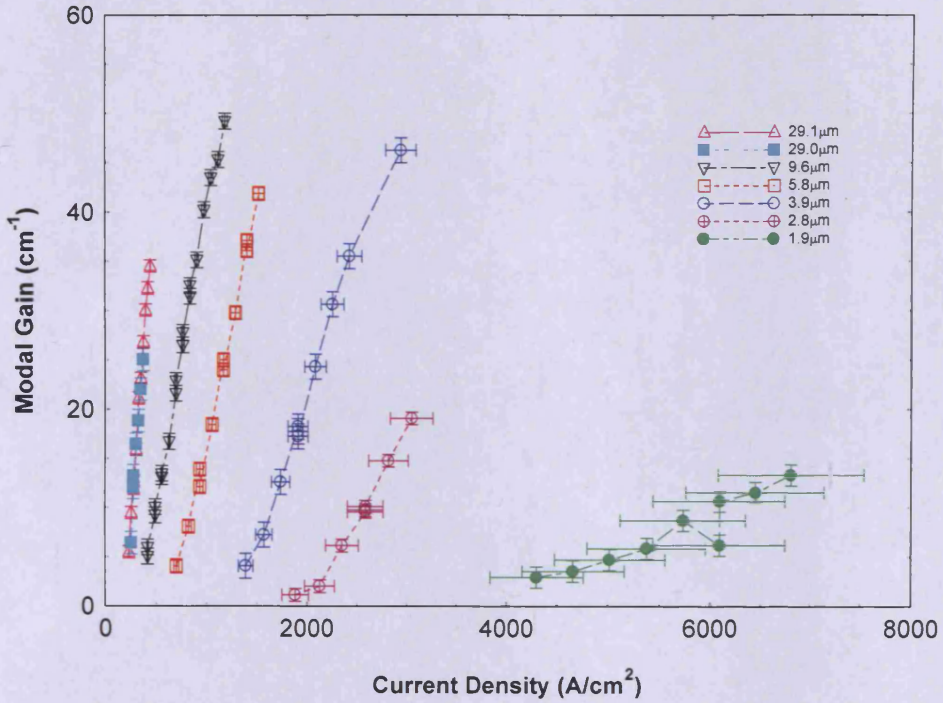

Figure 5-5. Peak net modal gain (G-α_i) characteristic as a function of current density (J_d) for the various ridge widths (W).

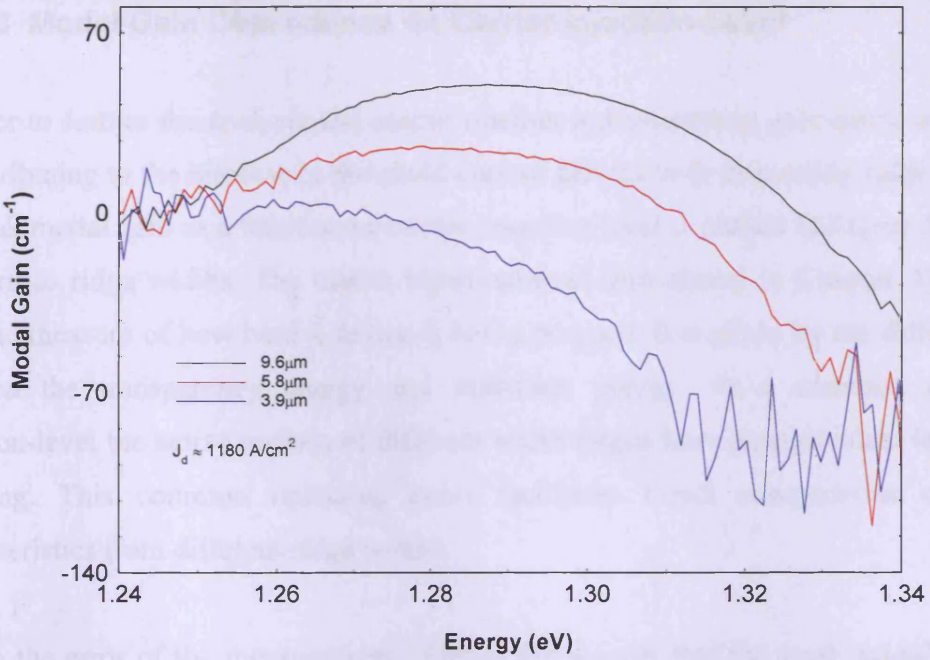

Figure 5-6. Modal gain spectra (G) for the 9.6, 5.8, and 3.9 μm ridge widths at the same J_d within error of 1180 A/cm^2.

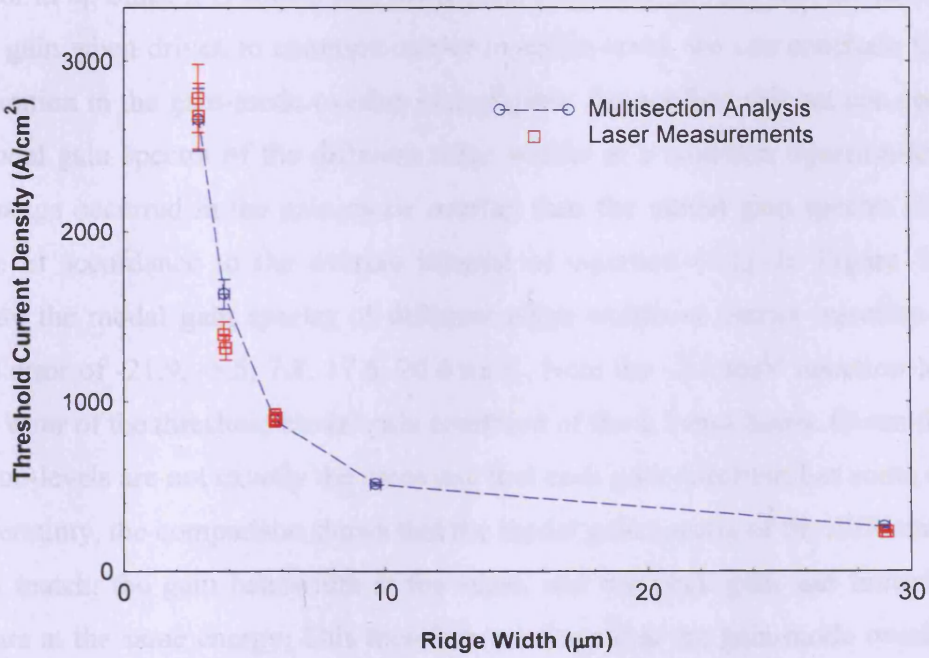

Figure 5-7. Threshold current density dependence with ridge width for 1.5mm D-RWG lasers with uncoated facets as measured from laser measurements and multisection gain analysis. The two sets of measurements agree well, thereby providing confidence in the multisection analysis and measured data.

5.3.2.3 Modal Gain Dependence on Carrier Injection-Level

In order to further the analysis and assess whether a deteriorating gain-mode overlap is contributing to the increase in threshold current density with decreasing ridge width, the peak modal gain as a function of carrier injection-level is plotted in Figure 5-8 for the various ridge widths. The carrier injection-level (introduced in Chapter 4) is an intrinsic measure of how hard a device is being pumped. It is given by the difference between the transparency energy and transition energy. At a common carrier injection-level the active regions of different width ridges have an equivalent level of pumping. This common operating point facilitates direct comparisons of the characteristics from different ridge widths.

Within the error of the measurements, Figure 5-8 reveals that the *peak modal gain-carrier injection-level* characteristic is approximately the same in all of the different ridge widths. The errors in the modal gain and carrier injection-level both arise from the error in α_i. Since it is shown that the different width ridges provide the same peak modal gain when driven to common carrier injection-level, we can conclude that the deterioration in the gain-mode overlap is negligible. To confirm this we can compare the modal gain spectra of the different ridge widths at a common injection-level. If any change occurred in the gain-mode overlap then the modal gain spectra (G) will change in accordance to the overlap integral of equation (4.1). In Figure 5-9 we compare the modal gain spectra of different ridge widths at carrier injection-levels within error of -21.9, -5.5, 7.8, 17.6, 26.6 meV. Note the -5.5 meV injection-level is within error of the threshold modal gain condition of the 1.5 mm lasers. Given that the injection-levels are not exactly the same and that each gain spectrum has some degree of uncertainty, the comparison shows that the modal gain spectra of the different ridge widths match: the gain bandwidth is the same, and the peak gain and transparency point are at the same energy. This therefore confirms that the gain-mode overlap has not significantly changed and moreover at the threshold condition the different ridge widths are pumped to an equivalent level. We conclude that the mechanism of a deteriorating gain-mode overlap has a negligible contribution to the threshold current density increase with decreasing W. This mechanism can only be significant for ridge widths much narrower than this study's experimental range i.e. < 1.9 μm.

In the *peak modal gain–carrier injection-level* characteristic a band-tail feature can be seen in the region below 0 eV. Band-tails in the QW can result from local structural defects, QW thickness variations, compositional variations, impurities, phonons, and stress variations. These factors cause local bandgap variations which when averaged over the sample, extend the energy bands into the energy gap. As a result the absorption and hence gain spectra do not have an abrupt increase at the bandgap, but rather a smooth extension into the bandgap. The band-tail extension typically has an exponential behaviour [9][10][11].

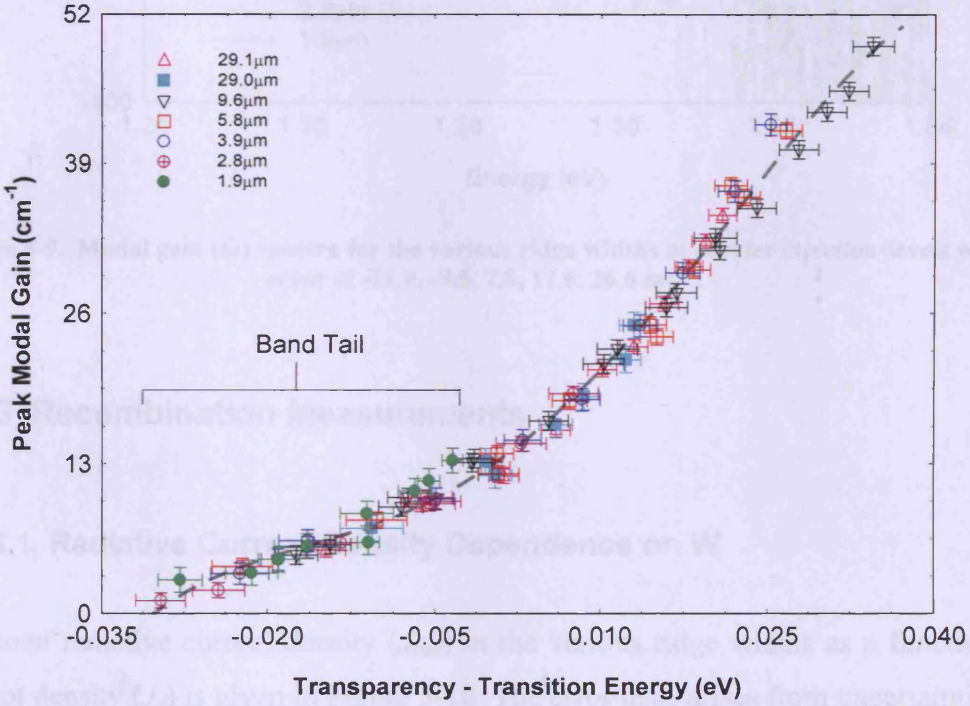

Figure 5-8. Peak modal gain characteristic as a function of carrier injection-level (transparency energy – transition energy) for the various ridge widths. The dashed line is a 4th order polynomial fit which is used to describe the shape of the characteristic and highlight the presence of a band-tail in the band structure.

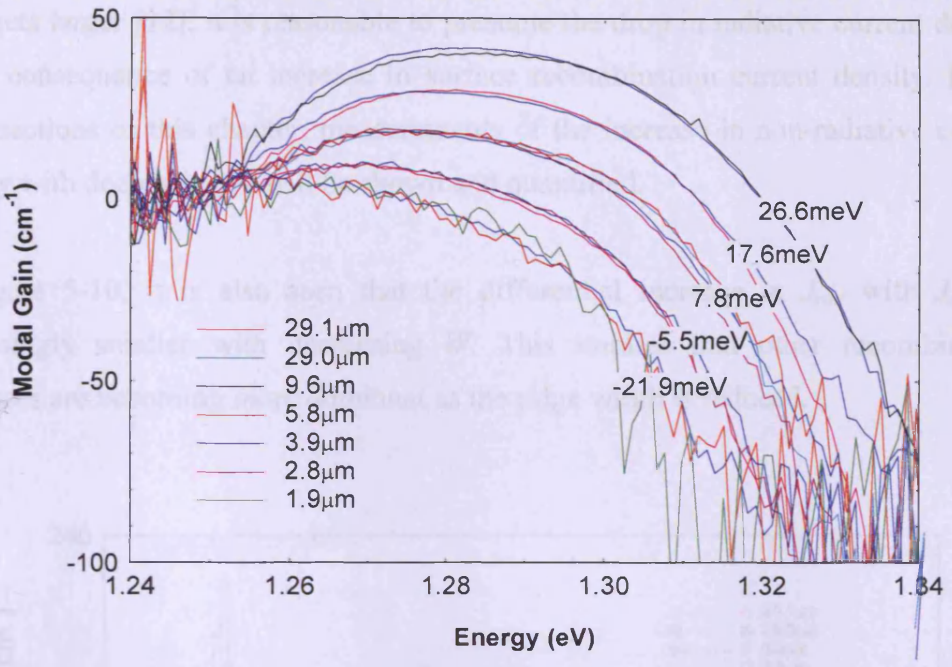

Figure 5-9. Modal gain (G) spectra for the various ridge widths at carrier injection-levels within error of -21.9, -5.5, 7.8, 17.6, 26.6 meV.

5.3.3 Recombination Measurements

5.3.3.1 Radiative Current Density Dependence on W

The total radiative current density (J_{rad}) in the various ridge widths as a function of current density (J_d) is given in Figure 5-10. The error in J_d arises from uncertainties in the ridge width and applied current, and the error in J_{rad} arises from the uncertainty in the calibration factor. Comparing the J_{rad}-J_d characteristic of each ridge width shows that as W decreases an increasingly lower fraction of the applied current density recombines radiatively. This is further illustrated in Figure 5-11 where the spontaneous emission rate spectra of the 3.9 and 2.8 μm ridge widths are compared at the same nominal current density of 1900 A/cm^2. It is clear that the 2.8 μm ridge has less radiative recombination. Consequently in order for the smaller ridge widths to produce the same radiative current density and also the same gain, a larger current density is required. This characteristic illustrates why the threshold current density increases with decreasing W in the 1.5 mm lasers. On the basis that the effects of non-radiative surface recombination are more severe when the exposed surface-to-volume

ratio gets larger [12], it is reasonable to presume the drop in radiative current density is the consequence of an increase in surface recombination current density. In the latter sections of this chapter, measurements of the increase in non-radiative current density with decreasing W will be shown and quantified.

In Figure 5-10, it is also seen that the differential increase in J_{rad} with J_d gets increasingly smaller with decreasing W. This implies that other recombination processes are becoming more dominant as the ridge width is reduced.

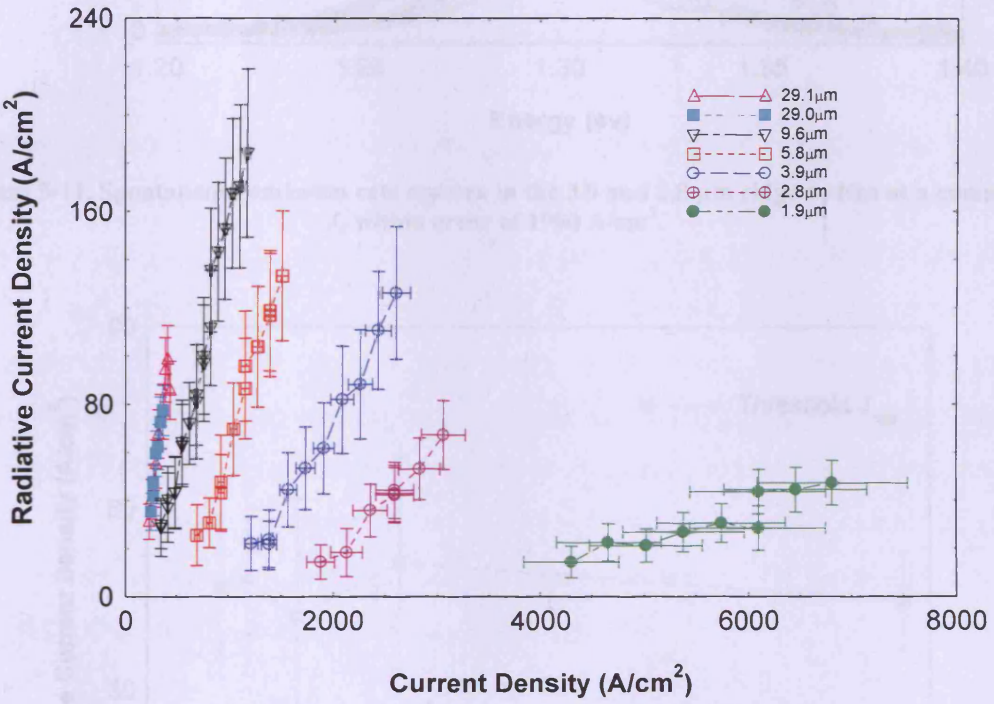

Figure 5-10. Radiative current density (J_{rad}) characteristic as a function of applied current density (J_d) in the various ridge widths.

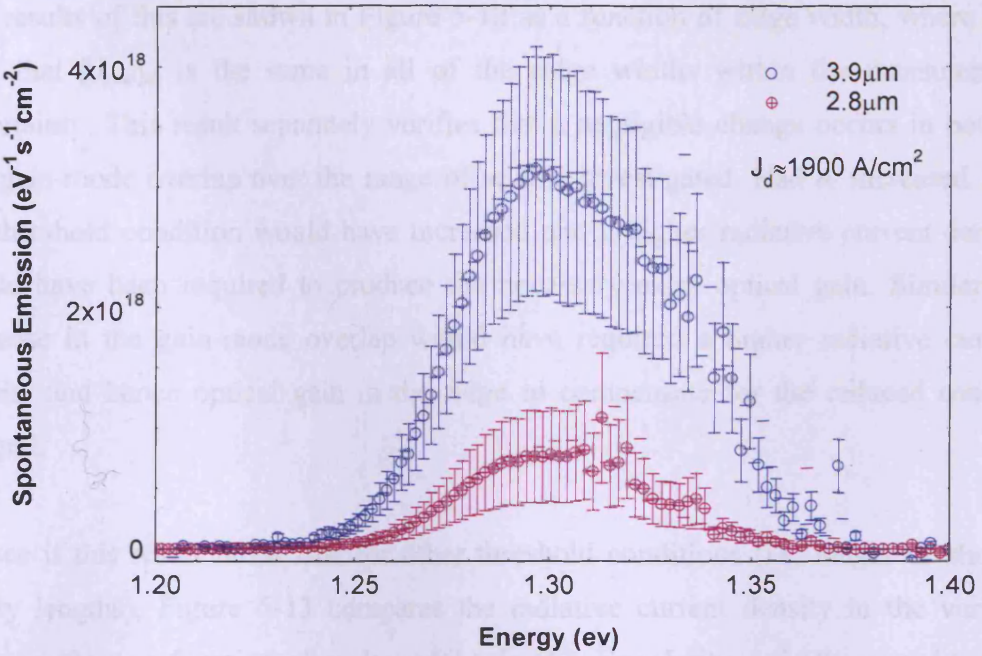

Figure 5-11. Spontaneous emission rate spectra in the 3.9 and 2.8 μm ridge widths at a common J_d within error of 1900 A/cm^2.

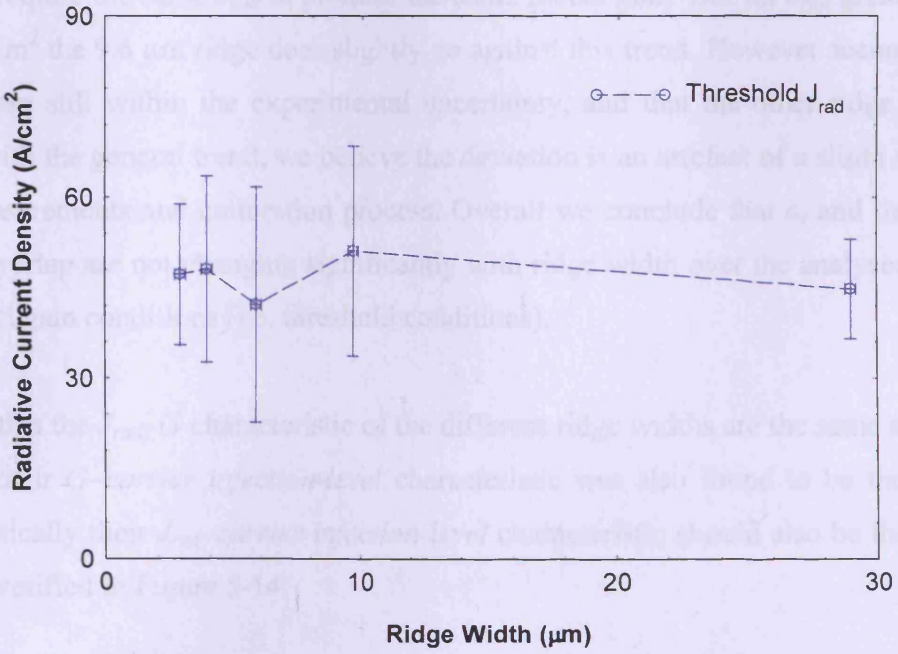

Figure 5-12. Measured radiative current density (J_{rad}) at the laser threshold condition of the 1.5mm lasers (c.f. Figure 5-2). The different ridge widths are seen to exhibit the same J_{rad}, thereby by showing that the threshold condition has not changed with ridge width.

The threshold radiative current density $[J_{rad}]_{th}$ for the 1.5 mm lasers can be determined from the J_{rad}-J_d characteristic in Figure 5-10 at the threshold current density, $[J_d]_{th}$.

The results of this are shown in Figure 5-12 as a function of ridge width, where it is seen that $[J_{rad}]_{th}$ is the same in all of the ridge widths within the measurement uncertainty. This result separately verifies that a negligible change occurs in both α_i and gain-mode overlap over the range of widths investigated. Had α_i increased then the threshold condition would have increased and a higher radiative current density would have been required to produce the necessary extra optical gain. Similarly a decrease in the gain-mode overlap would have required a higher radiative current density and hence optical gain in the ridge to compensate for the reduced overlap integral.

To see if this result holds true for other threshold conditions (i.e. longer or shorter cavity lengths), Figure 5-13 compares the radiative current density in the various ridge widths as a function of peak modal gain (G). For clarity, only the error bars for the 5.9 μm ridge are shown. The error bars for the other ridge widths are approximately of the same order. In general the comparison reveals the different ridge widths require the same J_{rad} to produce the same modal gain. But for J_{rad} greater than 100 A/cm^2 the 9.6 μm ridge does slightly go against this trend. However seeing as the values are still within the experimental uncertainty, and that the other ridge widths agree with the general trend, we believe the deviation is an artefact of a slight error in the measurements and calibration process. Overall we conclude that α_i and the *gain-mode* overlap are not changing significantly with ridge width over the analysed range of modal gain conditions (i.e. threshold conditions).

Seeing that the J_{rad}–G characteristic of the different ridge widths are the same and that earlier their *G–carrier injection-level* characteristic was also found to be the same, syllogistically their J_{rad}–*carrier injection-level* characteristic should also be the same. This is verified in Figure 5-14.

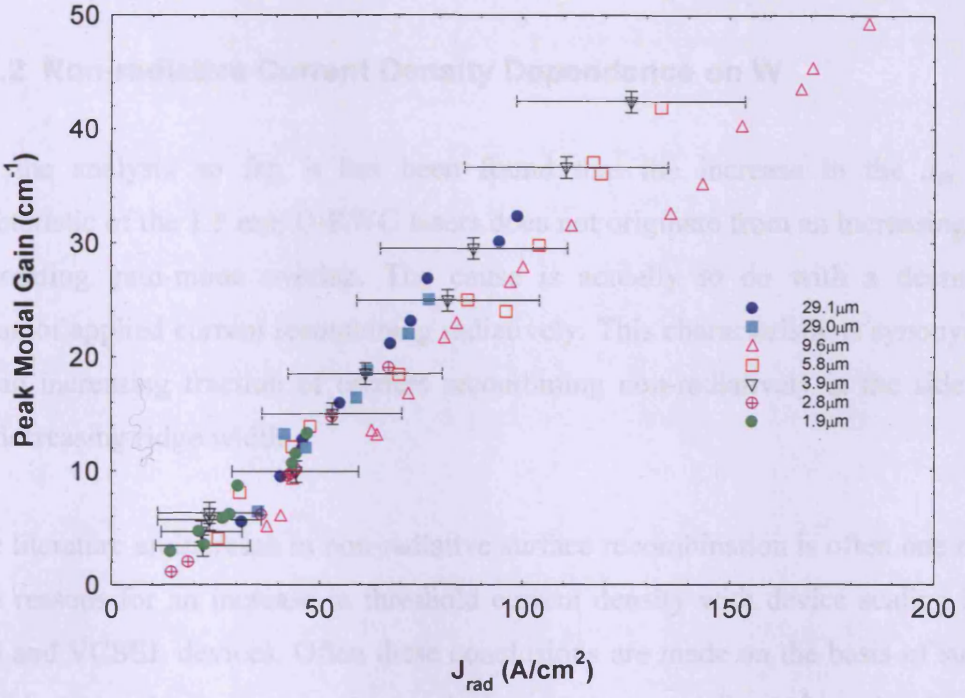

Figure 5-13. Peak modal gain (G) as a function of radiative current density (J_{rad}) for the various ridge widths. For clarity only the error bars for the 3.9 μm ridge are shown.

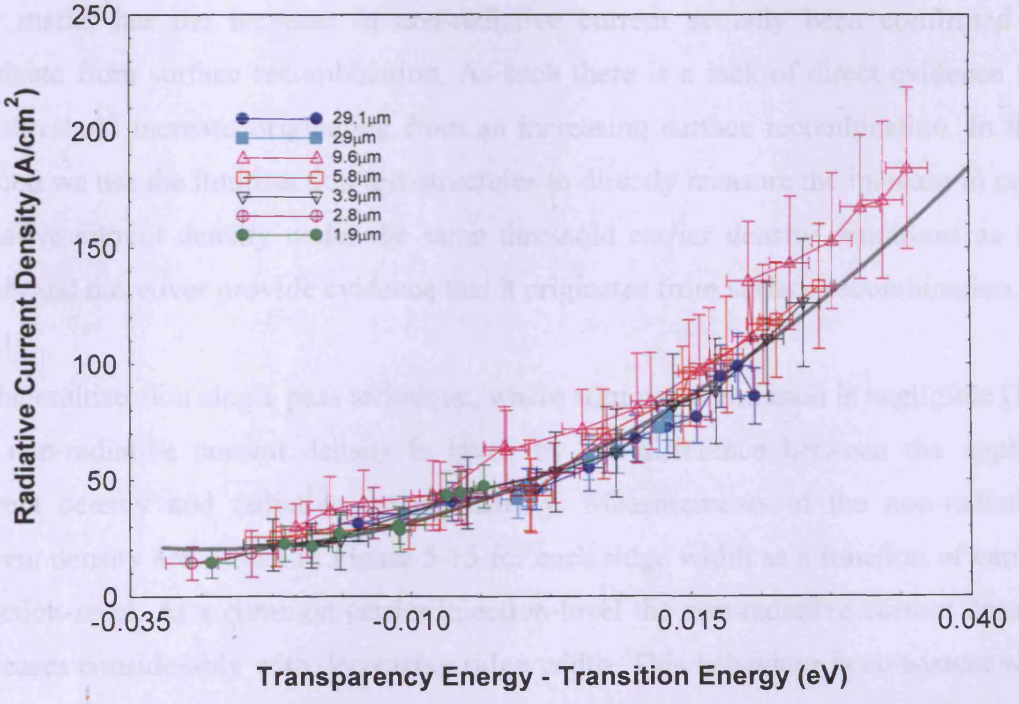

Figure 5-14. The characteristic of the radiative current density as a function of carrier injection-level for the various ridge widths. The solid grey line is a quadratic fit used to illustrate the general trend.

5.3.3.2 Non-radiative Current Density Dependence on W

From the analysis so far, it has been found that the increase in the $J_{th} - W$ characteristic of the 1.5 mm D-RWG lasers does not originate from an increasing α_i or deteriorating gain-mode overlap. The cause is actually to do with a decreasing fraction of applied current recombining radiatively. This characteristic is synonymous with an increasing fraction of carriers recombining non-radiatively at the sidewalls with decreasing ridge width.

In the literature an increase in non-radiative surface recombination is often one of the stated reasons for an increase in threshold current density with device scaling in D-RWG and VCSEL devices. Often these conclusions are made on the basis of surface recombination velocity measurements which are not necessarily made under the same working conditions. To the best of our knowledge the increase in non-radiative recombination which should arise from an increasing surface recombination process has not yet been measured or quantified under high injection-level conditions. Nor for that matter has the increase in non-radiative current actually been confirmed to originate from surface recombination. As such there is a lack of direct evidence for the threshold increase originating from an increasing surface recombination. In this section we use the multisection test-structures to directly measure the increase in non-radiative current density under the same threshold carrier density conditions as the lasers and moreover provide evidence that it originates from surface recombination.

In the multisection single pass technique, where stimulated emission is negligible [13], the non-radiative current density is given by the difference between the applied current density and radiative current density. Measurements of the non-radiative current density are shown in Figure 5-15 for each ridge width as a function of carrier injection-level. At a common carrier injection-level the non-radiative current density increases considerably with decreasing ridge width. This behaviour is consistent with a suspected increase in surface recombination. The rate of increase in J_{nr} with carrier injection-level increases as the ridge width is reduced; this implies that the increasing non-radiative recombination process is becoming more dominant.

In 5.3.2 a carrier injection-level of -5.5 meV was found to correspond to the threshold modal gain of the 1.5 mm lasers. The threshold non-radiative current density, $[J_{nr}]_{th}$, in the 1.5 mm lasers can therefore be determined by evaluating Figure 5-15 at that carrier injection-level. The results of this evaluation are given in Figure 5-16. This figure clearly shows an exponential type increase in $[J_{nr}]_{th}$ as the ridge width is reduced. The increase is so severe that from 29.1 to 9.6 μm $[J_{nr}]_{th}$ increases by a factor of 2 to a value of 462 A/cm^2, and from 29.1 to 2.8 μm by a factor of 11 to 2612 A/cm^2. In terms of percentage, non-radiative recombination makes up 84 % of the applied current density in the 29.1 μm ridge and 98 % in the 2.8 μm ridge. In contrast radiative recombination makes up 17 % and 2 % in the 29.1 μm and 2.8 μm ridges respectively. It is clear that non-radiative recombination is the dominant current path in the ridges, even for a width of 29.1 μm, and that there is a functional dependence in one of the non-radiative mechanisms as the percentage of J_{nr} increases with decreasing W. Non-radiative surface recombination is expected to have a functional dependence on cavity size as its recombination rate is proportional to the ratio of exposed surface area of the active region to volume of the active region [12].

In order to verify that the increasing fraction of non-radiative current density with decreasing W is the dominant mechanism causing the apparent increase in threshold current density in the 1.5 mm D-RWG lasers, a comparison of the fractional increase in J_{nr} and J_{th} with respect to the 29.1 μm ridge is performed in Figure 5-17. Since the fractional increase in J_{nr} agrees well with the fractional increase in J_{th}, it is clear that the increasing non-radiative mechanism is the principal cause of the J_{th}-W phenomenon. It should be noted that in Figure 5-17 we have included the relative ratio the 1.9 μm ridge in order to help illustrate the rapid increase in J_{nr}. This fractional increase however only shows the increase that would occur in laser threshold by the mechanism of an increasing J_{nr}. In reality the actual fractional increase for a 1.9 μm D-RWG laser would be much higher than this because α_i was found to increase for this width.

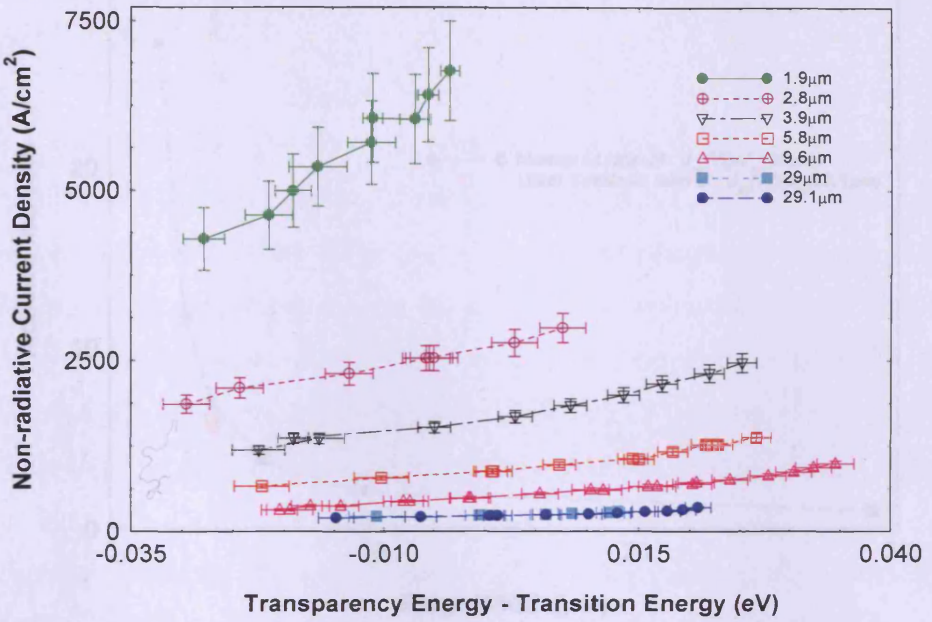

Figure 5-15. Measured non-radiative current density (J_{nr}) in the different ridge widths as a function of carrier injection-level (transition energy – transition energy)

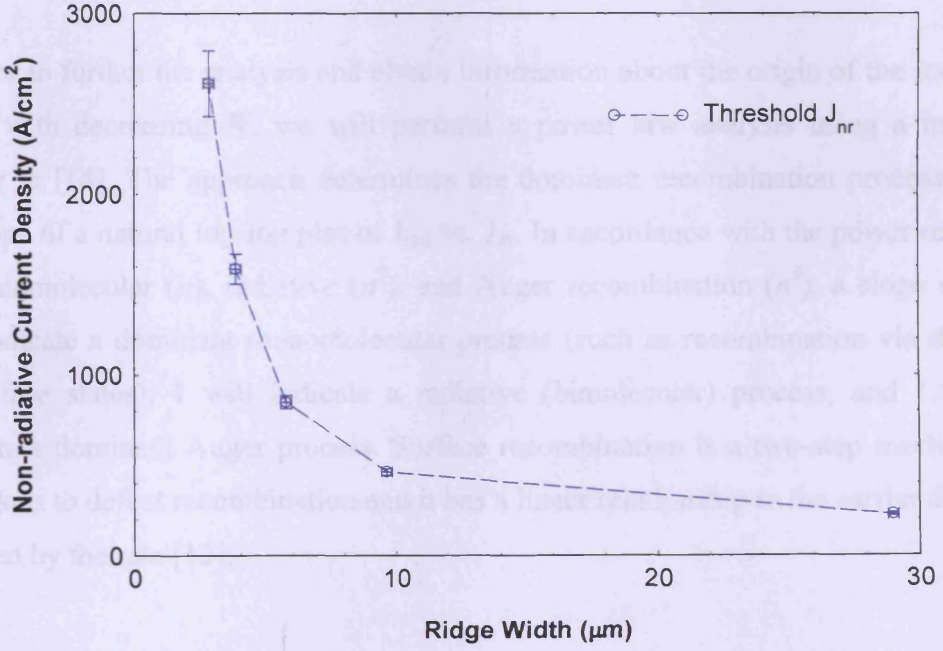

Figure 5-16. Threshold non-radiative current density $[J_{nr}]_{th}$ in the various ridge width 1.5 mm lasers.

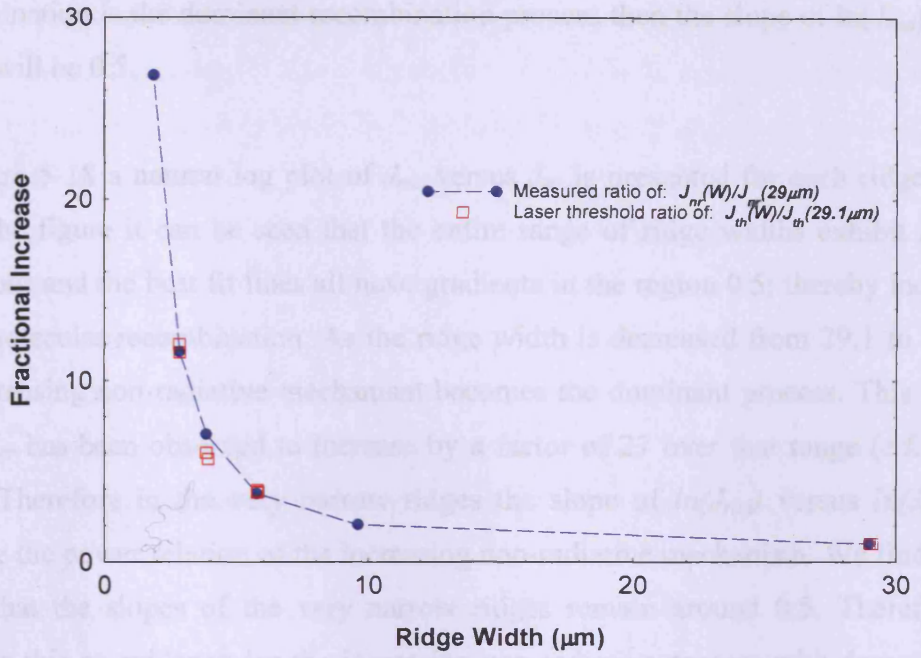

Figure 5-17. Comparison of the fractional increase in $[J_{nr}]_{th}$ and J_{th} of the 1.5 mm D-RWG lasers with respect to the 29.1 μm ridge. The good agreement reveals that the fractional increase in non-radiative processes is the dominant cause of the apparent increase in threshold with decreasing ridge width.

In order to further the analysis and obtain information about the origin of the increase in J_{nr} with decreasing W, we will perform a power law analysis using a method similar to [14]. The approach determines the dominant recombination process from the slope of a natural log-log plot of J_{rad} vs. J_{nr}. In accordance with the power relation of monomolecular (n), radiative (n^2), and Auger recombination (n^3), a slope of 0.5 will indicate a dominant monomolecular process (such as recombination via defects or surface states); 1 will indicate a radiative (bimolecular) process; and 1.5 will indicate a dominant Auger process. Surface recombination is a two-step mechanism analogous to defect recombination and it has a linear relationship to the carrier density as given by the rate [12]:

$$R_{sr} = \frac{a_s}{V} \cdot \upsilon_s \cdot n \qquad (5.1)$$

where a_s, V and υ_s are the exposed area of the active region, volume of the active region and surface recombination velocity respectively. Therefore if surface

recombination is the dominant recombination process then the slope of $\ln(J_{rad})$ versus $\ln(J_{nr})$ will be 0.5.

In Figure 5-18 a natural log plot of J_{rad} versus J_{nr} is presented for each ridge width. From the figure it can be seen that the entire range of ridge widths exhibit a linear behaviour and the best fit lines all have gradients in the region 0.5; thereby indicating monomolecular recombination. As the ridge width is decreased from 29.1 to 1.9 μm the increasing non-radiative mechanism becomes the dominant process. This is clear since J_{nr} has been observed to increase by a factor of 27 over that range (c.f. Figure 5-17). Therefore in the very narrow ridges the slope of $ln(J_{rad})$ versus $ln(J_{nr})$ will indicate the power relation of the increasing non-radiative mechanism. We find in this study that the slopes of the very narrow ridges remain around 0.5. Therefore we attribute this as evidence for the increasing non-radiative process with decreasing W being the monomolecular surface recombination mechanism.

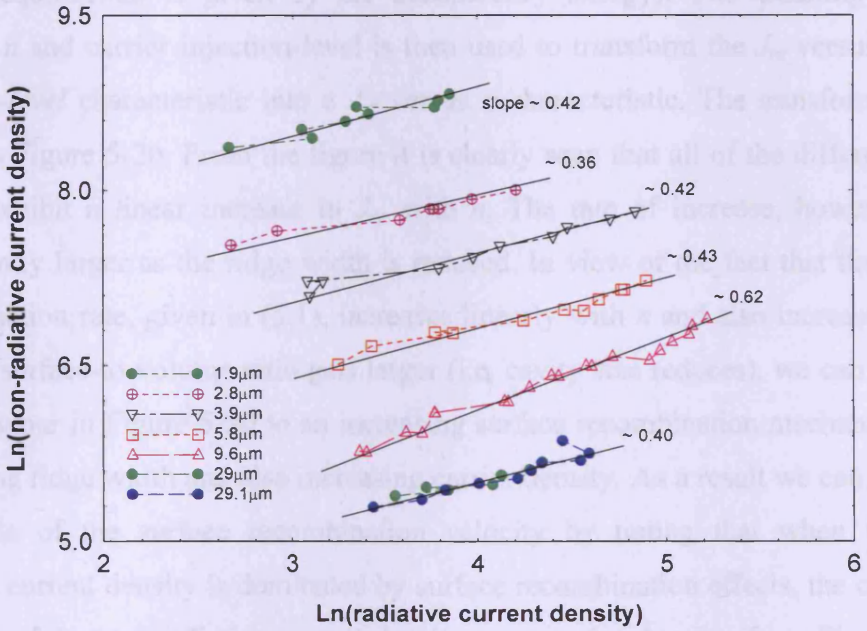

Figure 5-18. Natural log plot of J_{rad} versus J_{nr} for the various ridge widths. The gradient of the linear lines of best fit are used to describe the power relation of the dominant recombination process.

In order to provide further support for the above analysis we transform the J_{nr}–*carrier injection-level* characteristic into a relationship between J_{nr} and carrier density (n). To do this we use the SimWindows CAD package [15] to firstly model the dependence between quasi Fermi-level separation (transparency energy) and carrier density. SimWindows is a one-dimensional semiconductor device simulator which includes Fermi statistics, it has previously been successfully used to analyse VCSELs [16] and InGaN LED structures [17]. Since the simulator is only a 1-D solver of the current injection in the transverse direction, variations in the lateral direction are not considered and are assumed constant in the simulation. Furthermore, the simulator does not take into account of any band-tail effects in the energy band structure.

Figure 5-19 shows the simulated relationship between the quasi Fermi-level separation (ΔE_f) and bound carrier density in the active region (n). To obtain the relation in terms of carrier injection-level, the experimentally measured transition energy is simply subtracted from the quasi Fermi-level separation (which in quasi thermal equilibrium is given by the transparency energy). The resulting relation between n and carrier injection-level is then used to transform the J_{nr} versus *carrier injection-level* characteristic into a J_{nr} versus n characteristic. The transformation is shown in Figure 5-20. From the figure it is clearly seen that all of the different ridge widths exhibit a linear increase in J_{nr} with n. The rate of increase, however, gets significantly larger as the ridge width is reduced. In view of the fact that the surface recombination rate, given in (5.1), increases linearly with n and also increases as the exposed surface-to-volume ratio gets larger (i.e. cavity size reduces), we can attribute the behaviour in Figure 5-20 to an increasing surface recombination mechanism with decreasing ridge width and also increasing carrier density. As a result we can make an estimation of the surface recombination velocity by noting that when the non-radiative current density is dominated by surface recombination effects, the change in the slope of the non-radiative current density over carrier density (from Figure 5-20) with decreasing ridge width should approximately change in the same ratio as the surface-area-to-volume-ratio $\left({}^{a_s}\!/_{V}\right)$, in accordance with:

$$\frac{J_{nr}}{e \cdot n} \approx \frac{R_{sr}}{n} = \frac{a_s}{V} \cdot \upsilon_s \tag{5.2}$$

The surface recombination velocity can then be extracted from the slope of $\frac{J_{nr}}{e \cdot n}$ vs. $\frac{a_s}{V}$. From the results we perform this analysis over the range 10 μm and below. Table 6 gives the values of the two ratios and also shows that the change in $\frac{J_{nr}}{e \cdot n}$ does approximately increase in the same ratio as $\frac{a_s}{V}$ - as it should do if surface recombination is the dominating non-radiative recombination mechanism. Figure 5-21 gives the plot of $\frac{J_{nr}}{e \cdot n}$ vs. $\frac{a_s}{V}$ from which the slope gives a value of 1.87×10^5 cm/s for the surface recombination velocity. This value is in the reported range of surface recombination velocity measurements on strained InGaAs quantum-well material ($1\text{-}2 \times 10^5$ cm/s) [18].

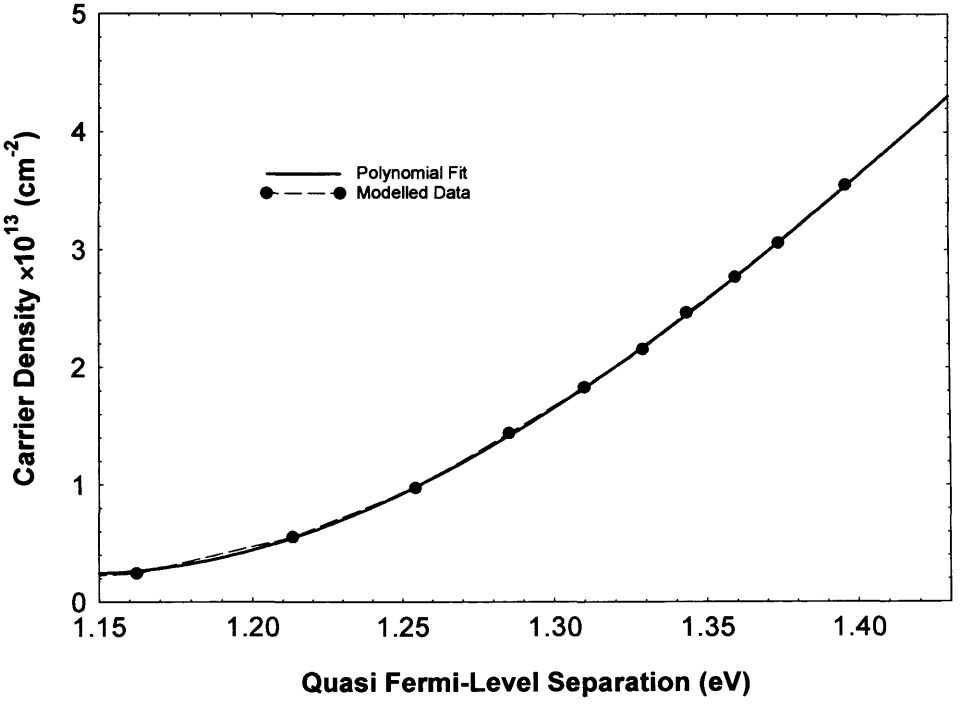

Figure 5-19. SimWindows simulation of the carrier density dependence on quasi Fermi-level separation.

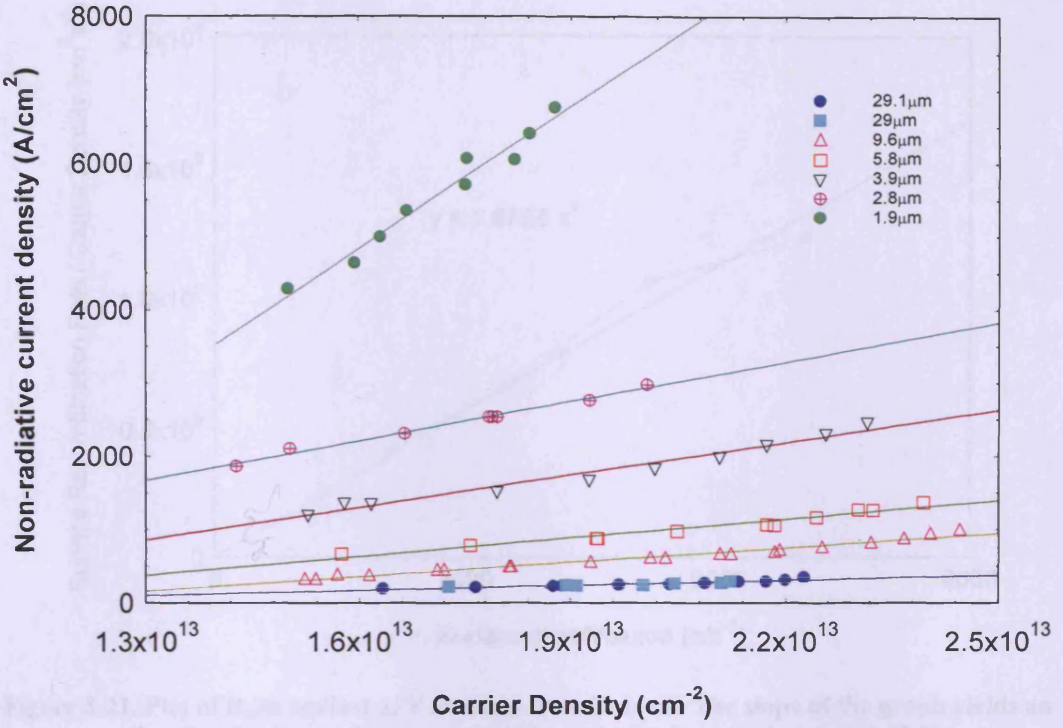

Figure 5-20. Modelled non-radiative current density dependence on carrier density (as determined from SimWindows) for the various ridge widths.

W (μm)	*slope J_{nr}/n*	*slope R_{sr}/n ($cm^2\ s^{-1}$)*	*a/V (cm^1)*	*Fractional change in J_{nr}/n with respect to 9.62 μm*	*Fractional change in a_s/V with respect to 9.62 μm*
9.62	6.54E-11	4.09E+08	2079.00	1.00	1.00
5.75	1.05E-10	6.56E+08	3478.26	1.61	1.67
3.85	1.69E-10	1.06E+09	5194.81	2.58	2.50
2.84	1.97E-10	1.23E+09	7042.25	3.01	3.39

Table 6. Parameters for slope of J_{nr}/n taken from Figure 5-20 and the corresponding parameters for R_{sr}/n, a_s/V, and the fractional change in J_{nr}/n and a_s/V with respect to the 9.62 μm ridge for various ridge widths.

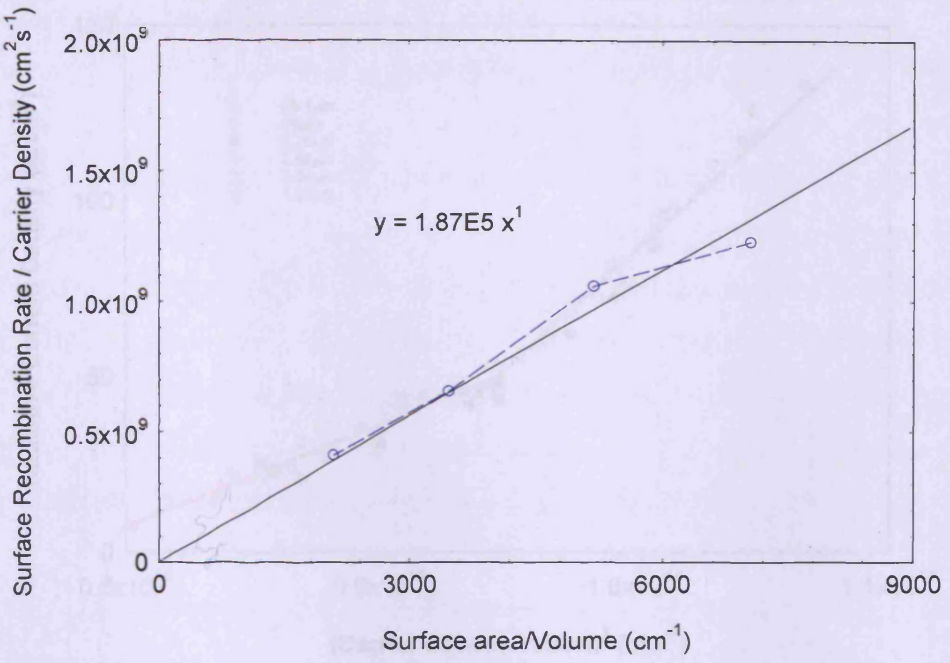

Figure 5-21. Plot of R_{sr}/n against a_s/V as taken from Table 6. The slope of the graph yields an estimation for the surface recombination velocity in accordance with (5.2).

In order to illustrate the reliability of using SimWindows to simulate the carrier density dependence on the measured recombination rates, we show in Figure 5-22 that the transformed radiative current density dependence on simulated carrier density is described by the expected square law dependence (i.e. bimolecular recombination). The only irregular feature in this plot is due to the band tail feature giving rise to two square relationships: one which describes the band tail region at low carrier densities; and another which describes the normal energy band structure at higher carrier densities.

In conclusion, the analysis in this section has provided experimental evidence to show that the dominant origin of the increasing J_{th} with decreasing W in the laser measurements is an increasing non-radiative surface recombination current. From the measurements we have also – for what we believe to be the first time – quantified the increase under high-level injection conditions and have shown it to accurately describe the apparent threshold increase in the 1.5 mm laser with decreasing ridge width.

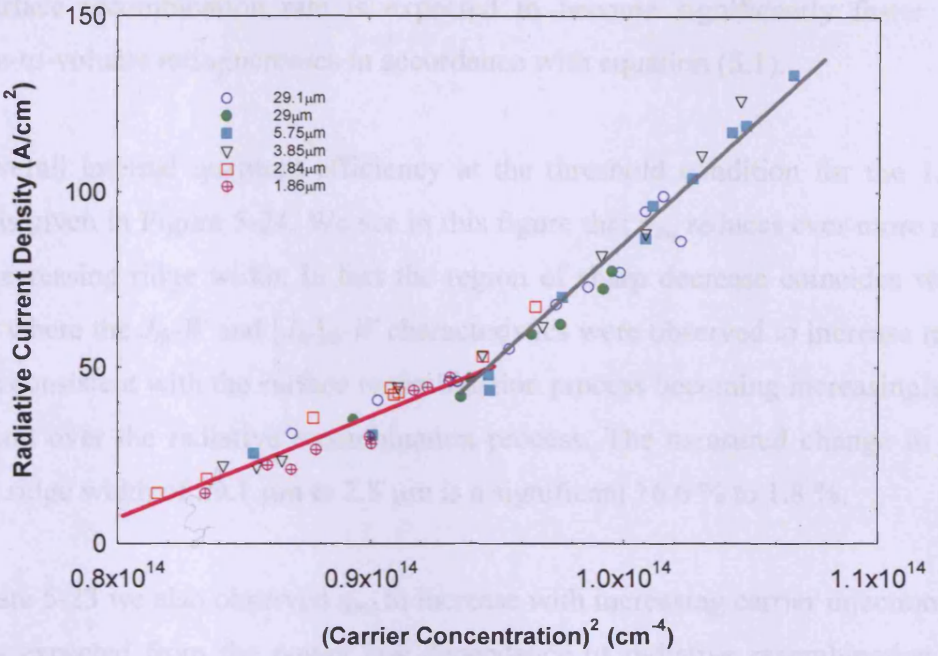

Figure 5-22. Modelled radiative current density dependence on the squared carrier density (as determined from SimWindows) for the various ridge widths. The linear fits show the expected dependence of the radiative recombination rate on the squared carrier density (i.e. bimolecular recombination)

5.3.3.3 Overall Internal Quantum Efficiency

In this section we now look at the affect surface recombination has on the overall internal quantum efficiency (η_{int}). The overall quantum efficiency is often used as a parameter to relate the total current density at threshold J_{th} to the spontaneous current density $[J_{spon}]_{th}$ by writing [19]:

$$[J_{spon}]_{th} = \eta_{\text{int}} \cdot J_{th} \tag{5.3}$$

It is defined as the fraction of applied drive current density that recombines radiatively i.e. J_{rad}/J_d. In Figure 5-23 η_{int} is plotted as a function of carrier injection-level for the various ridge widths. At a common carrier injection-level it is clear that as the ridge width is reduced η_{int} decreases. From the previous analysis of the radiative and non-radiative recombination currents, we can attribute this drop in η_{int} to the increasing loss of carriers to surface recombination at the exposed sidewalls. Indeed

the surface recombination rate is expected to become significantly faster as the surface-to-volume ratio increases in accordance with equation (5.1).

The overall internal quantum efficiency at the threshold condition for the 1.5 mm lasers is given in Figure 5-24. We see in this figure that η_{int} reduces ever more rapidly with decreasing ridge width. In fact the region of sharp decrease coincides with the region where the J_{th}-W and $[J_{nr}]_{th}$-W characteristics were observed to increase rapidly. This is consistent with the surface recombination process becoming increasingly more dominant over the radiative recombination process. The measured change in $[\eta_{int}]_{th}$ from a ridge width of 29.1 μm to 2.8 μm is a significant 16.6 % to 1.8 %.

In Figure 5-23 we also observed η_{int} to increase with increasing carrier injection-level. This is expected from the power law dependence of radiative recombination being proportional to the square of the carrier density (bimolecular) and surface/defect related recombination being linearly proportional the carrier density (monomolecular). As a result the radiative recombination rate increases faster with carrier injection-level and in doing so increases η_{int}. This differential increase in the η_{int} vs. carrier injection-level characteristic is seen to decrease with decreasing ridge width because the surface recombination rate increases with device size reduction and becomes more dominant. It should be noted that η_{int} will not indefinitely increase with injection-level because at some point other loss mechanisms such as Auger (which has a cubic relation to the carrier density) and carrier leakage will have a significant current contribution.

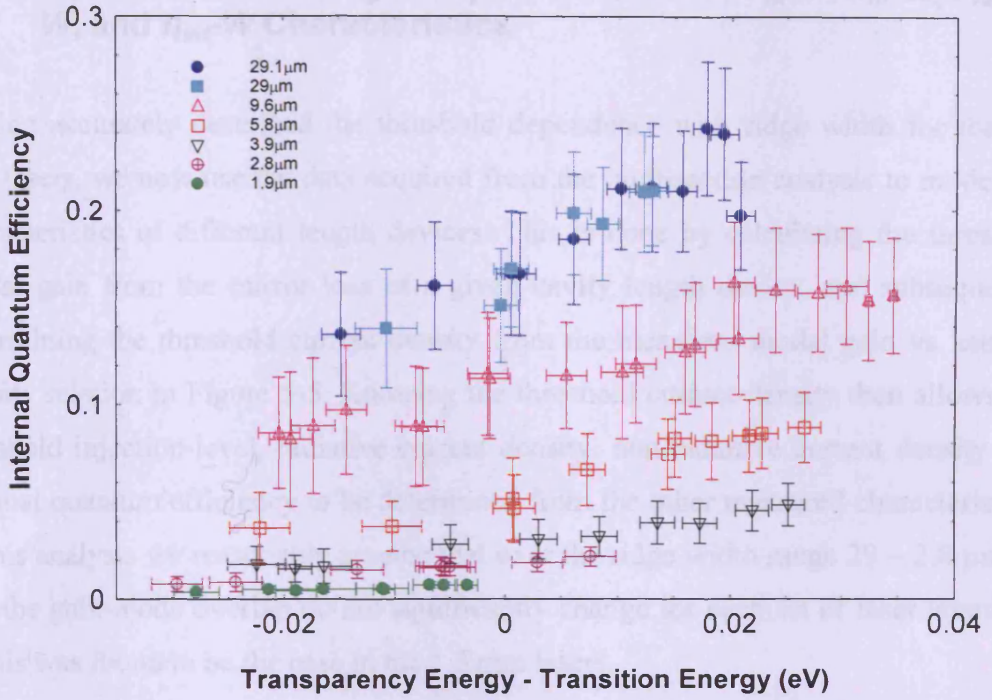

Figure 5-23. Measured internal quantum efficiency as a function of carrier injection-level for the various ridge widths.

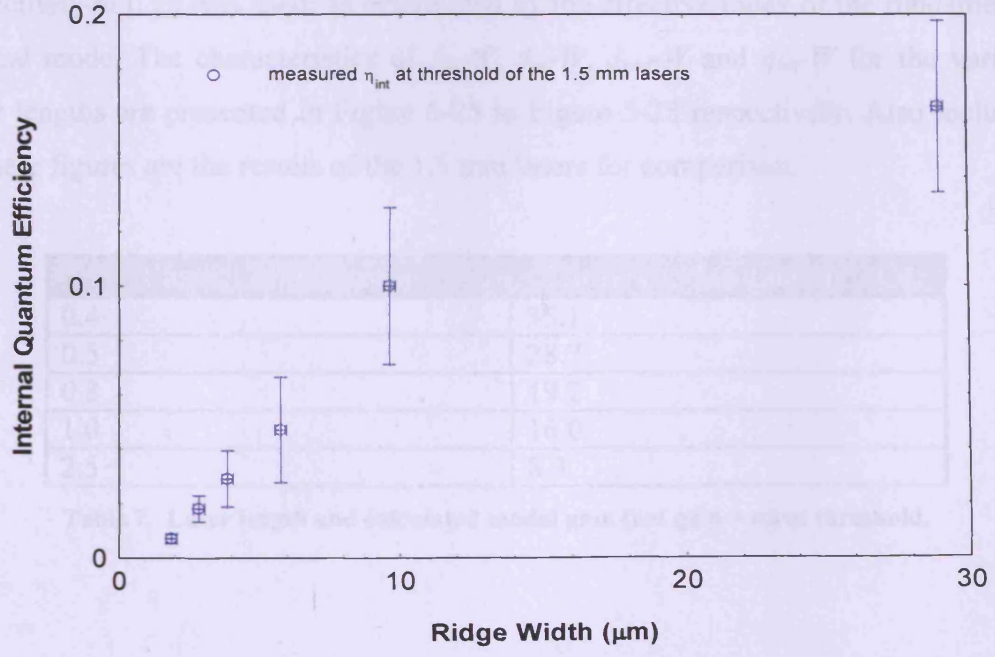

Figure 5-24. The overall internal quantum efficiency at the threshold condition for the various width 1.5 mm length D-RWG lasers.

5.3.4 Modelled Laser Length Dependence of the J_{th}-W, J_{nr}-W, J_{rad}-W, and η_{int}-W Characteristics

Having accurately described the threshold dependence with ridge width for the 1.5 mm lasers, we now use the data acquired from the multisection analysis to model the characteristics of different length devices. This is done by calculating the threshold modal gain from the mirror loss of a given cavity length device, and subsequently determining the threshold current density from the measured modal gain vs. current density relation in Figure 5-5. Knowing the threshold current density then allows the threshold injection-level, radiative current density, non-radiative current density and internal quantum efficiency to be determined from the other measured characteristics. In this analysis we reasonably assume that over the ridge width range 29 – 2.8 μm, α_i and the gain-mode overlap do not significantly change for each set of laser lengths – as this was found to be the case in the 1.5 mm lasers.

In Table 7 we summarise the various cavity lengths and corresponding threshold modal gain conditions that are used in the analysis. In these calculations a mirror reflectivity of 0.28 was used; as determined by the effective index of the fundamental optical mode. The characteristics of J_{th}-W, J_{nr}-W, J_{rad}-W and η_{int}-W for the various laser lengths are presented in Figure 5-25 to Figure 5-28 respectively. Also included in these figures are the results of the 1.5 mm lasers for comparison.

Laser Length (mm)	Threshold Modal Gain (G)
0.4	35.1
0.5	28.7
0.8	19.2
1.0	16.0
2.5	8.3

Table 7. Laser length and calculated modal gain (net gain + α_i) at threshold.

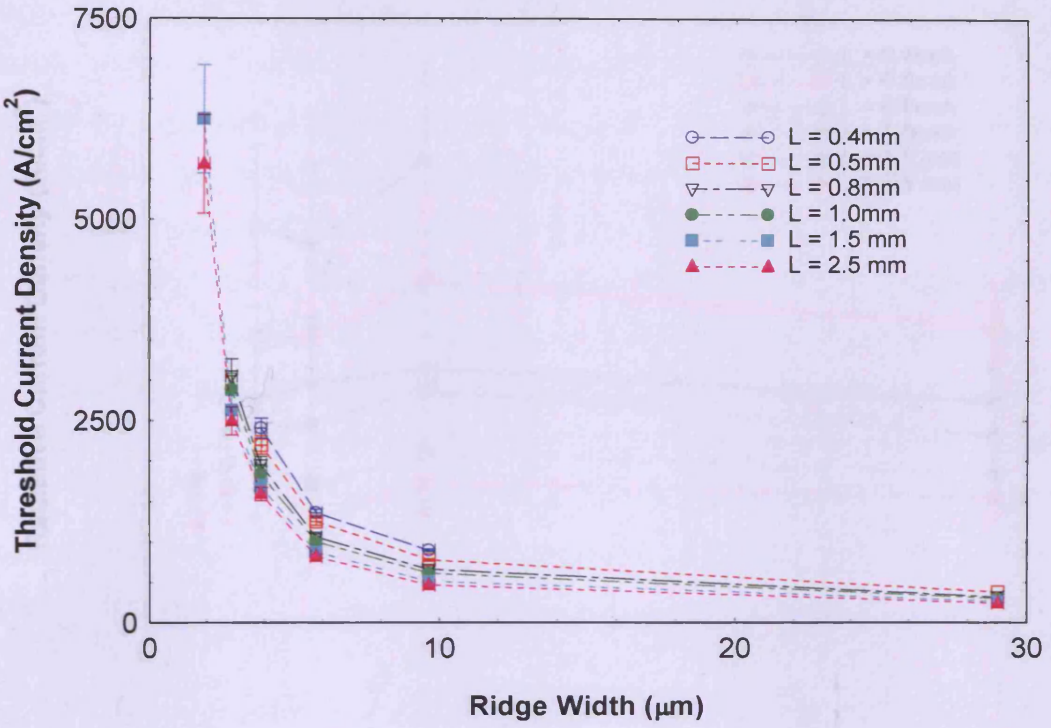

Figure 5-25. Threshold current density (J_{th}) dependence on ridge width (W) for laser lengths of 0.4, 0.5, 0.8, 1.0, 1.5, and 2.5 mm.

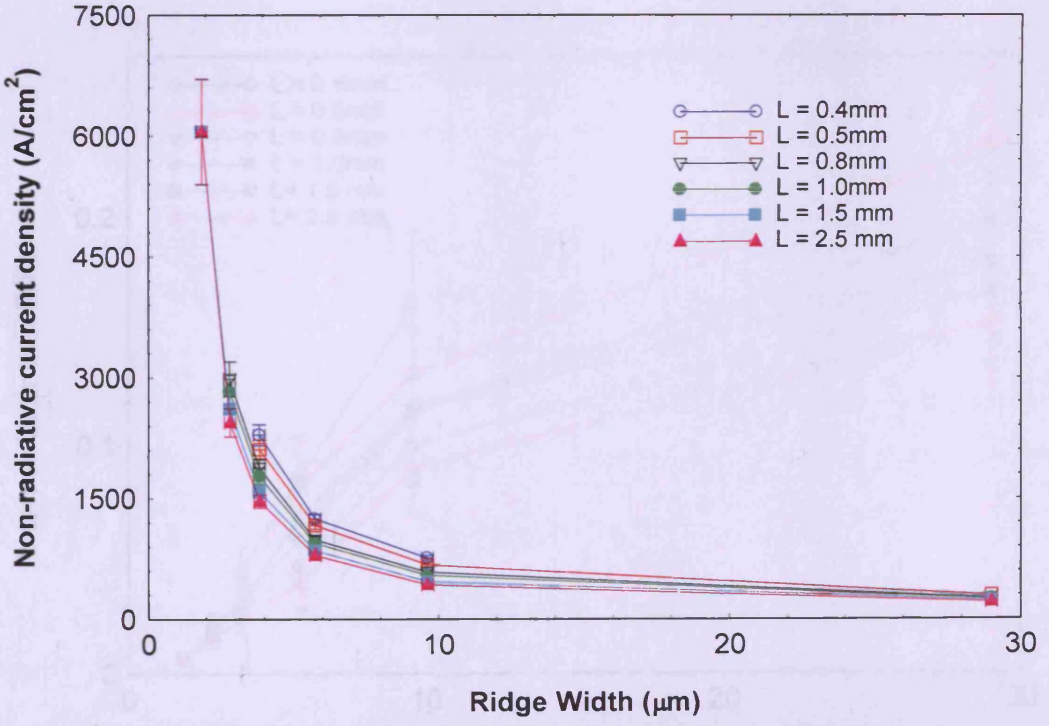

Figure 5-26. Non-radiative current density (J_{nr}) dependence on ridge width (W) at threshold for laser lengths of 0.4, 0.5, 0.8, 1.0, 1.5, and 2.5 mm.

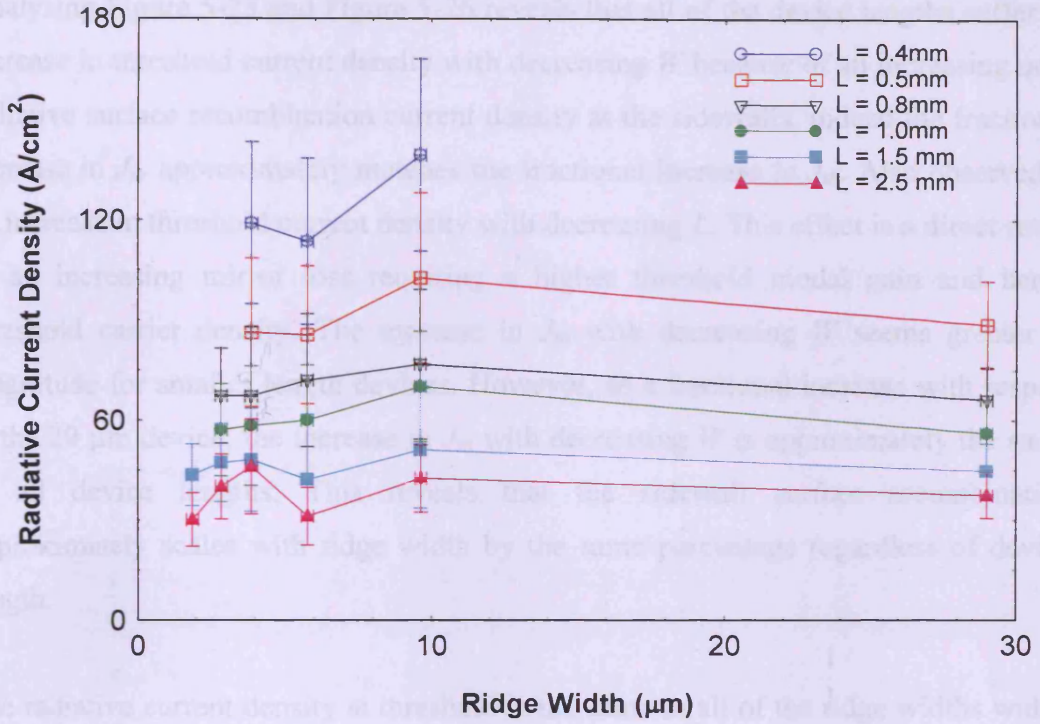

Figure 5-27. Threshold radiative current density (J_{rad}) dependence on ridge width (W) for laser lengths of 0.4, 0.5, 0.8, 1.0, 1.5, and 2.5 mm.

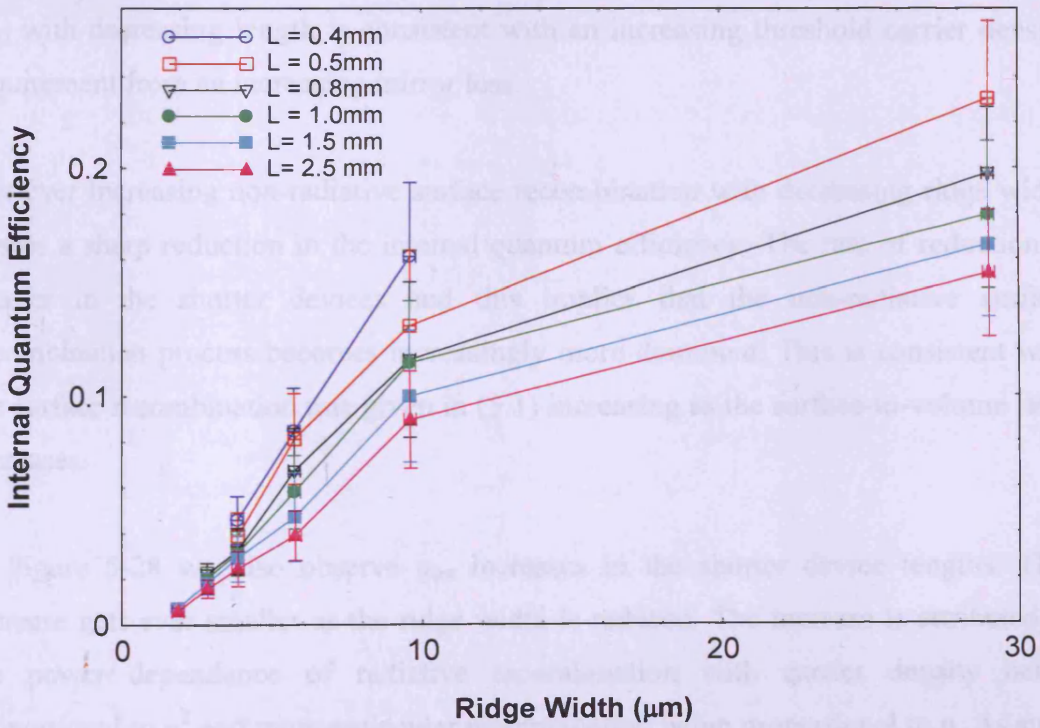

Figure 5-28. Internal quantum efficiency (η_{int}) dependence on ridge width (W) at threshold for laser lengths of 0.4, 0.5, 0.8, 1.0, 1.5, and 2.5 mm.

Analysing Figure 5-25 and Figure 5-26 reveals that all of the device lengths suffer an increase in threshold current density with decreasing W because of an increasing non-radiative surface recombination current density at the sidewalls. Indeed the fractional increase in J_{nr} approximately matches the fractional increase in J_{th}. Also observed is an increase in threshold current density with decreasing L. This effect is a direct result of an increasing mirror loss requiring a higher threshold modal gain and hence threshold carrier density. The increase in J_{th} with decreasing W seems greater in magnitude for smaller length devices. However, as a fractional increase with respect to the 29 μm device, the increase in J_{th} with decreasing W is approximately the same in all device lengths. This reveals that the sidewall surface recombination approximately scales with ridge width by the same percentage regardless of device length.

The radiative current density at threshold is the same in all of the ridge widths within the uncertainty of the experiment. This was also found to be the case in the 1.5 mm lasers and was shown to indicate that the modal gain was not being significantly affected by gain-mode overlap changes with ridge width. The increase in threshold J_{rad} with decreasing length is consistent with an increasing threshold carrier density requirement from an increasing mirror loss.

The ever increasing non-radiative surface recombination with decreasing ridge width causes a sharp reduction in the internal quantum efficiency. The rate of reduction is greater in the shorter devices and this implies that the non-radiative surface recombination process becomes increasingly more dominant. This is consistent with the surface recombination rate given in (5.1) increasing as the surface-to-volume ratio increases.

In Figure 5-28 we also observe η_{int} increases in the shorter device lengths. This increase gets ever smaller as the ridge width is reduced. The increase is attributed to the power dependence of radiative recombination with carrier density being proportional to n^2 and monomolecular recombination being proportional to n. As such the radiative recombination rate is expected to increase at a faster rate with increasing carrier density than monomolecular recombination (as discussed in 5.3.3). It should be

noted that if a significant Auger component existed in the total non-radiative recombination process (e.g. a n^3 dependence in the power law analysis) then η_{int} could even or might well decrease with decreasing L. The increase in η_{int} with decreasing L is smaller in the narrower ridge widths because the monomolecular non-radiative surface recombination process is also proportional to the surface-to-volume ratio (as discussed earlier). Thus in the narrower ridge widths the non-radiative surface recombination process becomes more dominant over the radiative process.

5.4 Summary and Conclusions

In summary we have examined the threshold current and current density characteristic of 1.5 mm D-RWG InGaAs quantum well lasers as a function of ridge width (Figure 5-1). Over the ridge width range 29 to 2.8 μm the apparent threshold current density was observed to increase at an ever increasing rate with decreasing ridge width. The increase from 29 to 2.8 μm was by a factor of 12. Measurements of the lasing wavelength were found to be the same in all of the ridge widths which suggested, but could not confirm, that the threshold losses in the system were not changing.

In order to establish the cause of the threshold increase, the multisection technique was used to characterise D-RWG segmented test structures of varying ridge widths. The initial net modal gain characterisation was shown to agree extremely well the laser threshold data, thereby confirming the accuracy of the measurements. From the gain spectra, the internal optical losses in the various ridge widths were determined. It was found that the internal optical loss did not change over the range 29.1 to 2.8 μm; the mean value was approximately 3.2 cm^{-1} with a standard error of 0.2 cm^{-1}. Therefore an increasing internal optical loss was not the cause of the threshold increase in the 1.5 mm D-RWG lasers.

The internal optical loss did however increase to 12.2 cm^{-1} in the 1.9 μm ridge. This was attributed to a significant increase in the wave amplitude at the rough sidewalls. In comparison to the S-RWG structures, the D-RWG structures have a stronger optical confinement due to the higher-index contrast. Consequently D-RWG can be made much narrower in width before an increase in scattering losses increases the

threshold. However, once a significant interaction of the wave amplitude and rough sidewalls does occur, the scattering loss in D-RWG structures is much more strongly affected. A sharp increase in the threshold current can then be expected to occur at this point; however other mechanisms may additionally contribute to the overall threshold increase. To scale down the size even further will then require reducing the surface roughness and increasing the index-contrast by using a lower refractive index material than BCB (~ 1.54 at λ=1.3 μm) to planarize and insulate the sidewalls.

Further analysis of each ridge width's threshold modal gain spectra, and peak modal gain as a function of carrier injection-level, demonstrated that the modal gain was the same for all of the ridge widths. Therefore the gain-mode overlap was not significantly changing with W. This concluded that the threshold increase in the 1.5 mm lasers with decreasing W was not the result of a deteriorating gain-mode overlap.

Measurements of the radiative current density were then acquired from the unamplified spontaneous emission spectra. It was found that the total radiative current density decreased with ridge width for a given current density. This indicated an increasing loss of applied current to other recombination paths, and furthermore illustrated why the apparent threshold current density increased with decreasing width in the 1.5 mm lasers. At threshold however, the radiative current density was found to be independent of ridge width. This observation separately confirmed that a changing α_i and gain-mode overlap were not the cause the apparent threshold current density increase in the 1.5 mm lasers. Further measurements of the radiative current density as a function of carrier injection-level demonstrated that all of the ridge widths have the same characteristics and at a common operating point (such as any common threshold condition) the radiative current density is the same in all of the ridge widths. This was confirmed by showing that the same radiative current density was required to produce the same modal gain.

Non-radiative current density measurements at a common carrier injection-level showed an increase with decreasing ridge width. This accounted for the decreasing fraction of applied current recombining radiatively with decreasing W. The behaviour was stated to be typical of an increasing surface recombination current at the exposed

sidewalls. Reports in literature have attributed threshold increases and poor device performance in D-RWG and VCSELS to this effect but, to the best of our knowledge, the presumed increase in non-radiative recombination has not yet been quantified. By measuring the non-radiative current density at the threshold condition of the D-RWG 1.5 mm lasers, we for the first time quantified the increase in non-radiative current density with decreasing *W*. Moreover, these measurements are of high-level injection conditions (desirable for characterising the device performance under proper working conditions). The increase from 29.1 to 2.8 μm was measured to be a factor of 12. By comparing the fractional increase in non-radiative current density to the fractional increase in threshold current density of the 1.5 mm lasers, the non-radiative current density measurements were found to accurately describe the threshold increase. This revealed that the dominant cause of the threshold increase in the 1.5 mm lasers was an increasing non-radiative current density.

By performing a power law analysis of the non-radiative current density we revealed a dominant monomolecular recombination process; this was in accordance with the surface recombination process being proportional to *n*. Additional evidence for surface recombination was found by simulating the device operation using SimWindows in order to convert the J_{nr} vs. *carrier injection-level* characteristic in to an equivalent J_{nr} vs. *carrier density characteristic*. From this analysis, J_{nr} was found to be linear with *n* in all of the ridge widths. Moreover, the differential increase in J_{nr} with n was found to increase with decreasing *W*. This observation was consistent with the surface recombination rate being proportional to the exposed surface to volume ratio as well as *n*.

Internal quantum efficiency measurements at a common carrier injection-level showed a decrease with ridge width. This was consistent with the increasing fraction of non-radiative surface recombination with decreasing *W* causing the narrower ridge widths to require a higher applied current density in order to operate at the same carrier injection-level. The quantified decrease in efficiency in the 1.5 mm lasers from a width of 29.1 to 2.8 μm is 14.8 % of the applied current density.

The final part of the analysis used the multisection data to characterise the J_{th} vs. W, J_{nr} vs. W, J_{rad} vs. W and η_{int} vs. W of other length lasers. This analysis found the threshold current density increased with decreasing device length and ridge width due to an increasing mirror loss and non-radiative surface recombination respectively. Furthermore the surface recombination process increased the threshold current density in the same fraction with decreasing ridge width regardless of device length. The threshold radiative current density was found to be approximately independent of ridge width for all length (as was found in the J_{rad} vs. *carrier injection-level* characteristic), but did increase with decreasing device length. Measurements of the internal efficiency revealed a decrease with ridge width in all of the laser lengths. This effect was more pronounced in the smaller length devices. Furthermore, it was also revealed that the internal efficiency actually increased with decreasing length. This effect was attributed to the power relationship of radiative recombination being proportional to n^2 and monomolecular recombination being proportion to n. Thus the efficiency increases as the threshold requirement and concomitant carrier density increases. However the extent of the increase decreases with ridge width; as here the surface recombination effect becomes so dominating that the differential increase in radiative current density with applied current density reduces significantly.

[1] V. Malyarchuk, J. W. Tomm, V. Talalaev, and Ch. Lienau, "Nanoscopic measurements of surface recombination velocity and diffusion length in a semiconductor quantum well," Applied Physics Letters, 81, 2, p346, 2002.
[2] J. S. Osinski, K. M. Dzurko, S. G. Hummel, and P. D. Dapkus, "Optimization of stripe width for low-threshold operation of quantum well laser diodes," Applied Physics Letters, 56 (25), p2487, 1990.
[3] C. Shieh, J. Mantz, H. Lee, D. Ackley, and R. Engelmann, "Anomalous dependence of threshold current on stripe width in gain-guided strained-layer InGaAs/GaAs quantum well lasers," Applied Physics Letters, 54 (25), p2521, 1989.
[4] T. R. Chen, Y. H. Zhuang, L. E. Eng, and A. Yariv, "Cavity length dependence of the wavelength of strained-layer InGaAs/GaAs laser," Applied Physics Letters, 57, p2402, 1990.
[5] M-K Chin, C-W Lee, S-Y Lee, and S. Darmawan, "High-index-contrast waveguides and devices," Applied Optics, 44, 15, p3077, 2005.
[6] K. K. Lee, D. R. Lim, H-C Luan, A. Agarwal, J. Foresi, "Effect of size and roughness on light transmission in a Si/SiO_2 waveguide: Experiments and model," Applied Physics Letters, 77, 11, p1617, 2000.
[7] D. Liang, J. Wang, J. –T. Huang, J. Yeh, L. Mawst and D. Hall, "Deep-etched native-oxide-confined high-index-contrast AlGaAs heterostructure lasers with 1.3μm dilute-nitride quantum wells," IEEE Journal of Selected Topics in Quantum Electronics, 13, 5, p1324-1331, 2007.
[8] R. J. Deri, E. Kapon, "Low-Loss III-V Semiconductor Optical Waveguides," IEEE Journal of Quantum Electronics, 27, 3, 1991.
[9] H. P. Zappe, "Introduction to semiconductor integrated optics," Artech House Publishers, ISBN 0-89006-789-9.
[10] R. A. Smith, "Semiconductors," Cambridge University Press, second edition, 1978.

[11] F. Stern, "Gain-Current Relation or GaAs Lasers With n-Type and Undoped Active Layers," IEEE Journal of Quantum Electronics, 9, 2, p290, 1973.
[12] L. A. Coldren and S. W. Corzine, "Diode lasers and photonic integrated circuits," Wiley Series in Microwave and Optical Engineering, 1995.
[13] P. Blood, G. M. Lewis, P. M. Smowton, H. Summers, J. Thompson, and J. Lutti, "Characterisation of semiconductor laser gain media by the segmented contact method," IEEE Journal of Selected Topics in Quantum Electronics, 9, 5, p1275, 2003.
[14] R. Fehse, S. Tomic, A. R. Adams, S. J. Sweeney, E. P. O'Reilly, A. Andreev, H. Riechert, "A quantitative study of radiative, Auger, and defect related recombination processes in 1.3-μm GaInNAs-based quantum-well lasers,"IEEE Journal of Selected Topics in Quantum Electronics, 8, 4, p801, 2002.
[15] http://www.ocs.colorado.edu/SimWindows/simwin.html
[16] D. W. Winston, R. E. Hayes, "Optoelectronic device simulation of Bragg reflectors and their influence on surface-emitting laser characteristics," IEEE Journal of Quantum Electronics, 34, 4, p707, 1998.
[17] J. D. Thompson, I. A. Pope, P. M. Smowton, P. Blood, R. J. Lynch, G. Hill, T. Wang, and P. Parbrook, "The influence of acceptor anneal temperature on the performance of InGaN/GaN quantum-well light-emitting diodes," Journal of Applied Physics, 99, 024507, 2006.
[18] S. Y, Hu, S. W. Corzine, K. K. Law, D. B. Young, A. C. Gossard, L.A. Coldren, and J. L. Merz, "Lateral carrier diffusion and surface recombination in InGaAs/AlGaAs quantum-well ridge waveguide lasers," Journal of Apllied Physics, 76, 4479, 1994.
[19] P. M. Smowton and P. Blood, "The differential efficiency of quantum-well lasers," IEEE Journal of Selected Topics in Quantum Electronics, 3,2, 1997.

Chapter 6: Overall Summary & Conclusions

In this project I investigated the performance limiting mechanisms which restrict the further miniaturisation of S-RWG and D-RWG laser diodes and also how the dimensionality of the active region material system can affect the scaling behaviour. These devices and material systems are current technology and are in the near-term potential candidates for use in OEICs. Focus was put on the effects of:

(1) the internal optical loss

(2) gain-mode overlap

And primarily:

(3) the loss of carriers to recombination processes outside of the pumped area where round trip amplification occurs (lateral out-diffusion) in S-RWG devices with a quantum-dot active region

(4) the loss of carriers to recombination at exposed sidewalls of the active region (surface recombination) in D-RWG devices with a quantum-well active region.

The approach used primarily involved the multisection characterisation technique to measure the modal gain, internal optical loss, radiative and non-radiative recombination current density, and overall internal quantum efficiency. By evaluating these device characteristics as a function of ridge width and comparing the changes at a common carrier injection-level, I was able to circumvent the problems of previous techniques and measure the effects of all of these mechanisms separately and take into account their relative impact. These observed trends provided a comprehensive view of how these mechanisms affected device performance, and indeed were shown to accurately explain the increase in apparent threshold current with decreasing ridge width. Moreover, these measurements enabled me to evaluate the lateral ambipolar diffusion process in the quantum-dot system as a function of injection-level and temperature. This provided a better understanding of how lateral carrier diffusion is currently thought to be inhibited in such systems by revealing there to be two regimes where the ambipolar diffusion length is reduced. Together these measurements were insightful in understanding the criteria for improving the performance of RWG devices with size reduction.

What follows is a brief summary of the investigations.

6.1 Lateral carrier out-diffusion in a quantum-dot ridge waveguide structure

- From the net modal gain data it was apparent that as the ridge width was reduced the current density required to produce a given net modal gain (i.e. a given threshold condition) increased. For example, the current density for a net modal gain of 4.7 cm^{-1} (calculated to be the threshold condition for a laser of length 2.7 mm) in the 10, 6, and 4 μm ridges was 490, 577, 1010 A/cm^2 respectively.
- The cause of this increase was investigated in terms of three key mechanisms: (1) an increasing internal optical loss, (2) a deteriorating gain-mode overlap, and (3) an increasing fraction of lateral out-diffusion current.
- Measurements of the internal optical loss in the various ridge widths found an increase with decreasing ridge width. The measured values were 2.57, 3.42, 5.87 cm^{-1} for the 10, 6, and 4, μm ridges respectively. The cause of increase was attributed to an increase in scattering from the ridge sidewalls. This finding revealed that the mechanism of an increasing internal optical loss should not be neglected when attempting to model the threshold current dependence on the ridge width. Nor is it accurate to measure the internal optical loss from a broad area ridge and apply it to calculations involving narrow ridge widths.
- To account for the effect of an increasing internal optical loss, the peak modal gain for the various ridge widths were compared as a function of current density. This comparison revealed that the current density for a given modal gain was still higher in the narrower ridge widths: thereby implying that at least one of the other key mechanisms was having a significant impact on the threshold behaviour.
- Comparing the modal gain spectra of the various ridge widths at a common drive current density showed that the narrower ridge widths were being pumped to a lower level: the transparency energy was lower and the gain spectrum was narrower. This also inferred an increasing loss of applied current

to lateral out-diffusion and/or a decrease in the overlap between the gain profile and optical mode profile.

- Additional evidence for the above point was provided by comparing the Fermi-level separation with respect to the transition energy (carrier injection-level) as a function of current density for the various ridge widths. This showed the narrower ridge widths had a lower carrier injection-level for a given current density.
- Through comparing the peak modal gain and the modal gain spectra of the various ridge widths at a common carrier injection-level each device was shown to exhibit the same spectra and peak modal gain. This result was consistent was a negligible change in the gain-mode overlap with reducing the ridge width. Had the overlap changed then the modal gain spectra at a common inversion-level would have been different. This result is not to say however that the change in gain-mode overlap is negligible for all ridge widths. At some width narrower than this studies experimental range the optical overlap is expected to reduce. The overlap will also presumably decrease in cases of an extremely non-uniform lateral carrier density profile and hence gain profile.
- Confirmation of a negligible change in the gain-mode overlap was observed by comparing the peak modal gain of the various ridge widths as a function of total radiative current density. From this it was found that the same peak modal gain was produced by the different ridge widths for a given radiative current density.
- The total non-radiative current density (i.e. taken to be the difference between the applied current density and total radiative current density within the ridge) as a function of carrier injection-level revealed that the narrower ridge widths had a higher non-radiative current density. This finding was consistent with the previous findings and implied a greater impact from the lateral out-diffusion current mechanism.
- The general trend of the total non-radiative current density dependence on injection-level was the same in all ridge widths. After an injection-level of about 84 meV a higher order non-radiative recombination rate was observed. This implied that, apart from lateral out-diffusion, all of the other non-

radiative carrier loss processes were occurring in the same manner with increasing carrier injection-level.

- From these evaluation processes, it was apparent that the current density dependence on the ridge width at a fixed modal gain was the result of lateral out-diffusion.
- Using the measured current density values at a common carrier injection-level, the lateral carrier density profile in the various ridges widths were modelled with the fitting condition of a common average carrier density within the ridge. This yielded a value for the lateral ambipolar diffusion length. The fitting condition was based on the fact that the total radiative current density within the ridge was measured to be the same at a common carrier injection-level (i.e. common modal gain).
- At a carrier injection-level of approximately 0.122 eV the lateral ambipolar diffusion length was estimated to be 0.84 μm.
- Modelling the threshold current density dependence with ridge width for this lateral ambipolar diffusion length showed excellent agreement with the measured data. The model showed the lateral out-diffusion effect had a negligible impact on the threshold performance of devices with widths greater than about 20 μm. However, as the ridge width is reduced the fraction of carriers lost to lateral out-diffusion becomes significant and the apparent threshold current density rapidly increases with decreasing ridge width.
- The fraction of applied current lost to lateral out-diffusion was 4.2 % in the 20 μm. This increased to 20.3 % when the ridge width was reduced to 4 μm. Consequently this observation highlights that as the ridge width becomes comparable to the lateral ambipolar diffusion length; the fraction of applied current lost to lateral out-diffusion becomes evermore significant.
- Analysing the lateral ambipolar diffusion length as a function of carrier injection level revealed a strong dependence on the Fermi-level separation. From an injection-level of 65 meV to 84 meV the lateral ambipolar diffusion length increased from 0.75 μm to a maximum value of 1.5 μm. Further increasing the injection-level then resulted in the lateral ambipolar diffusion length decreasing. At an injection-level of 122 meV the lateral ambipolar diffusion length had reduced to 0.85 μm.

- The increase in lateral ambipolar diffusion length with injection-level was attributed to an increase in the number of carriers thermally escaping out of the dot and into the wetting-layer where they can laterally diffuse along the wetting-layer plane. The point after which the diffusion length decreased with increasing injection-level coincided with a higher order non-radiative recombination process and also a sharp decrease in overall internal quantum efficiency. As such, the decrease in lateral ambipolar diffusion length was attributed to an apparent increase of the non-radiative recombination rate in the wetting-layer with increasing carrier density and consequently a decrease in the carrier lifetime and hence diffusion length.

6.2 *Surface recombination in quantum-well deep-etched ridge waveguides*

- Laser measurements on 1.5mm long devices showed the threshold current to initially decrease by 22 % from a ridge width of 29 to 5.7 μm. This was consistent with a reduced inversion area requiring less current for a given transparency current density. Reducing the ridge width beyond 3.8 μm caused a rapid rise in threshold current: For the 2.8 μm ridge the threshold current increased by 48% with respect to the 5.7 μm ridge, and 16% with respect to the 29 μm ridge. An optimum ridge width with the lowest threshold current occurred at the inflection point somewhere between 5.7 μm and 3.8 μm.
- The apparent threshold current density was observed to increase at an ever increasing rate with decreasing ridge width. The increase from 29 to 2.8 μm was by a factor of 12!
- The three key mechanisms which can cause the apparent threshold current density to increase were stated to be: (1) an increasing internal optical loss, (2) a deteriorating gain-mode overlap, (3) an increasing fraction of applied current being lost to surface recombination at the exposed sidewalls.
- The lasing wavelength of the different width devices were all measured to be approximately 974 ± 1 nm.
- ASE measurements were found to dominantly TE polarised with a negligible TM component.

- The internal optical loss was found to be invariant with ridge width in the range 29 to 2.8 μm. The mean value was 3.2 cm^{-1}. This revealed that an increasing internal optical was not having an impact on the laser threshold data. However, at a ridge width of 1.9 μm there was a significant increase by a factor of 3.8. This was attributed to increased wave amplitude interacting with the rough sidewalls and thereby increasing the scattering loss.
- In comparison to the S-RWG structure, the D-RWG structure can be made much narrower (< 2.8 μm) before a significant increase in the internal optical loss occurs. This is due to stronger optical confinement from the higher lateral index-contrast. However, once a significant interaction of the wave amplitude and rough sidewalls does occur, the scattering loss in D-RWG structures is much more strongly affected. To scale down the size even further will then require reducing the surface roughness and increasing the index-contrast by using a lower refractive index material than BCB (~ 1.54 at λ=1.3 μm) to planarize and insulate the sidewalls.
- Measurements of peak modal gain and modal gain spectra at a common current density showed that the narrower ridge widths were being pumped to a lower inversion level: the peak modal gain, transparency energy and gain bandwidth were all lower. This finding suggested that a larger fraction of current was being lost to other current paths other than radiative, and/or the gain-mode overlap was decreasing.
- An analysis of the peak modal gain and modal gain spectra at various common injection-levels – including that which corresponded to the threshold condition of the 1.5 mm lasers – showed each device to exhibit the same characteristic. This indicated a negligible change in the gain-mode overlap over the range 29 μm to 1.9 μm. However, it was noted that a significant change maybe expected to occur for ridge widths narrower than have been studied.
- In the peak modal gain vs. injection-level characteristic, a band-tail feature was observed in the region below 0 eV.
- By comparing the total radiative current density in each device as a function of current density it was found that an increasingly lower fraction of the applied current density was recombining radiatively as the ridge width was reduced. Measurements of the spontaneous emission spectra at a common current

density confirmed this. These findings were in agreement with the modal gain analysis. The implication of this effect on the threshold performance is that narrower ridge widths require a larger current density to generate the necessary radiative current density and modal gain.

- Measurements of the total radiative current density at threshold for the various width 1.5 mm long lasers showed no variation with ridge width. This separately verified that the internal optical loss and gain-mode overlap were not changing with ridge width.
- Analysis of the non-radiative current density at a common carrier injection-level showed a considerable increase in non-radiative recombination with decreasing ridge width. The analysis also found the rate of increase in non-radiative current density with carrier injection-level increased as the ridge width was reduced. Both of these observations were consistent with a suspected increase in surface recombination rate with ridge width reduction.
- The fractional increase in threshold non-radiative current density with decreasing ridge width was determined for the 1.5 mm lasers. This showed good agreement with the fractional increase in threshold current density dependence on ridge width. As such it was clear that the increasing non-radiative process with decreasing ridge width was the dominant cause of the apparent laser threshold dependence on ridge width.
- The fractional increase in threshold non-radiative current density for the 1.5 mm lasers was significant. From a width of 29.1 to 9.6 μm the non-radiative current density increased by factor of 2 to a value of 462 A/cm^2, and from 29.1 to 2.8 μm by a factor of 11 to 2612 A/cm^2.
- Information about the origin of the increasing non-radiative recombination process was obtained by a power law analysis on the slope of a natural log-log plot of the non-radiative current density vs. radiative current density. The analysis revealed that the dominant recombination process in the narrowest ridges – where the increasing non-radiative mechanism caused more than a doubling of the non-radiative current density with respect to the 29.1 μm ridge – was monomolecular. This recombination behaviour is consistent with surface recombination.

- In order to provide more evidence to correlate the increasing non-radiative recombination current density with decreasing ridge width to surface recombination, the measured non-radiative current density vs. carrier injection-level characteristic was transformed into a plot of non-radiative current density vs. carrier density. This required modelling the carrier density dependence on Fermi-level separation using a program called SIMWIN. From the transformation it was clearly seen that all of the different ridge widths exhibited a linear increase in non-radiative current density with carrier density. However the rate of increase was significantly larger in the narrower ridge widths. Since the surface recombination rate is linear with carrier density (i.e. monomolecular) and also increases with surface-to-volume ratio (i.e. reducing the ridge width), these findings were highly supportive of surface recombination being the origin of the increase in non-radiative recombination.
- The overall internal quantum efficiency at threshold in the 1.5 mm lasers was measured to significantly decrease as the ridge width was reduced. This is a direct consequence of an increasing fraction of applied current recombining via surface recombination. The measured decrease from a ridge width of 29.1 μm to 2.8 μm was 16.6 % to 1.8 %.
- However the internal quantum efficiency was seen to increase with carrier injection-level. This is assumed to be due to the radiative recombination rate increasing with a square dependence on carrier density (bimolecular), while the surface and defect recombination rate increased with a linear dependence (monomolecular). It was stated that the increase will probably not continue indefinitely with inversion-level as higher-order non-radiative recombination process might become significant.
- The effect of surface recombination in different length devices was modeled by using the measured characteristics. From this it was found that the sidewall surface recombination approximately scales with ridge width by the same percentage regardless of device length.
- The threshold radiative current density was approximately the same in all ridge widths of the same length. Shorter length devices did however have a higher threshold radiative current density due to an increased mirror loss.

- The overall internal quantum efficiency was observed to drop with ridge width in all length devices. However the smaller length devices did have higher internal quantum efficiency due to a high injection-level requirement. It should be noted that if a significant Auger component existed in the total non-radiative recombination process (e.g. a n^3 dependence in the power law analysis) then the internal quantum efficiency could even or might well decrease with decreasing device length.
- One way of reducing the loss of carriers to surface recombination in D-RWG structures and thereby improving the threshold performance, is by using a quantum-dot active region instead of a quantum-well. From the study in chapter 4 it was apparent that the lateral ambipolar diffusion process can be inhibited by the three-dimensional confinement of carriers in the quantum-dot. Whilst carriers are localised in the quantum-dots they can not interact with the surface-states. The best reduction in surface recombination will occur when lasing is on the ground state. Carriers in the ground state experience the greatest confining potential and are thereby better confined. Also device operation at low temperatures will help as the thermal broadening of carriers over the higher energy states will be reduced and also the probability of thermal escape into the wetting-layer where they can laterally diffuse will be less. In terms of device miniaturisation, a quantum-dot D-RWG structure should permit smaller devices than either quantum-dot S-RWG or quantum-well D-RWG, as the increase in the internal optical loss occurs at narrower ridge widths and the surface recombination should be less. At some point though further reduction will increase the internal optical loss and may also decrease the gain-mode overlap. This will increase the threshold gain requirement and may induce lasing on the higher energy states of the quantum-dot. In this case the lateral ambipolar diffusion length can increase due to increased thermal escape to the wetting-layer and surface recombination will increase. Laser operation at an even higher injection-level will eventually reduce the ambipolar diffusion length but at the expense of losing additional carriers to higher order non-radiative recombination processes. These detrimental effects can even occur in wide ridge width devices if there is insufficient gain to lase on the ground-state. Measures for

inducing lasing on the ground state include: reducing the scattering loss and thereby also allowing smaller devices; and increasing the ground state gain by increasing the number of quantum-dot layers, reducing the inhomogeneous broadening, and non-radiative process.

Chapter 7: Further Work

Several useful investigations have emerged as a result of the work carried out in this project. These include:

(a) further investigations on the lateral carrier diffusion mechanism in quantum-dot and quantum-well systems,

(b) measuring the surface recombination velocity,

(c) evaluating different methods of passivating exposed surfaces to reduce surface-states,

(d) and a concept of a new test-structure for measuring the lateral ambipolar diffusion length and surface recombination velocity together

What follows is a brief description of each proposed investigation.

(a)

In Chapter 1 I mentioned that the dimensionality of the active region can influence the apparent lateral ambipolar diffusion length. In quantum-wells, carrier confinement in the growth direction restricts diffusion to the two dimensions of the QW plane. By further reducing the dimensionality for confinement in all three dimensions (quantum-dot) the diffusion of carriers can be further restricted. In an ideal quantum-dot system, where the dots are isolated zero-dimensional states, three-dimensional confinement completely localises carriers and thereby prevents diffusion.

However, in self-assembled S-K quantum-dot systems, the formation and proximity of a wetting-layer provides a means for carriers to laterally diffuse along the 2-dimensional plane. The process is that of: thermal escape into the wetting layer where carriers laterally diffuse; recapture into a dot; and eventual recombination of the electron-hole pair at some point in the structure. This coupled transport mechanism is thought to inhibit lateral carrier diffusion rather than completely suppressing it. The question that naturally emerges as a result of this is: do S-K quantum-dots have a lower ambipolar diffusion length than quantum-well systems?

In the first instance, this question can be indirectly answered by comparing the laser threshold dependence on ridge width between quantum-well systems and quantum-

dots systems. If a reduction is seen in the fractional increase of threshold current density with decreasing ridge width then this can imply a smaller ambipolar diffusion length. This is provided that the other threshold increasing mechanisms in the two systems have the same dependence with ridge. Such a comparative study has already commenced with work on comparing the laser threshold behaviour of D-RWG quantum-dot devices with the D-RWG quantum-well devices studied in Chapter 5. Given in Figure 7-1 are the results of this initial comparison at 300 K. The quantum-dot system analysed here is essentially the same as that analysed in Chapter 4 apart from the growth temperature of the GaAs spacer layer being at 585 °C. The consequence of this change in spacer growth temperature is that this sample has a lower threshold performance than the system studied in Chapter 4: as such the 1.5 mm lasers were all found to lase on the 1st excited state at 300K. Despite this the results in Figure 7-1 clearly show that the quantum-dot D-RWG structures have a distinct reduction in the fractional increase of threshold current density with decreasing ridge width as compared to the quantum-well D-RWG structures. This preliminary result directly shows clear promise for improved scaling behaviour with quantum-dot devices. Furthermore this improvement in scaling behaviour can be expected to be even better by using the quantum-dot samples studied in Chapter 4 where lasing occurs on the ground state at 300 K for 1.5 mm lasers.

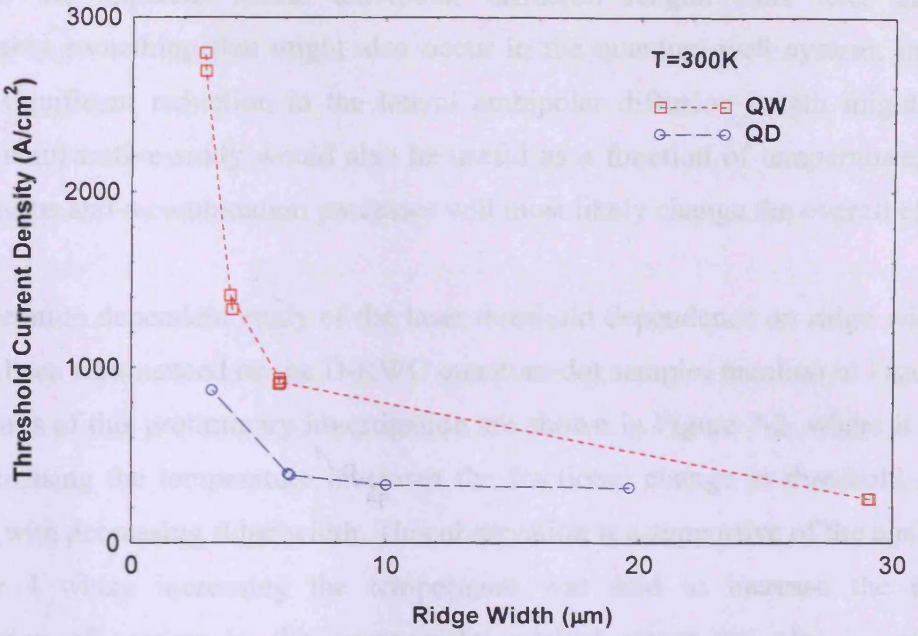

Figure 7-1. Comparison of the threshold current density dependence on ridge width between quantum-well D-RWG and quantum-dot D-RWG lasers of length 1.5 mm at 300K.

In order to directly relate the improved scaling behaviour to a reduced ambipolar diffusion length and also quantify the change, the study in Chapter 4 can be carried out on the quantum-well material system and compared to the quantum-dot results. This approach circumvents the problems of previous studies by: measuring the device characteristics and considering the three key mechanisms which influence the threshold current density dependence on ridge width. Moreover the approach permits the lateral ambipolar diffusion length to be measured as a function of inversion-level – this benefit was particularly insightful for understanding the diffusion mechanism in the quantum-dot system.

Such measurements would then allow a comparative analysis between quantum-wells and quantum-dots as a function of inversion-level. This will then show the difference in apparent lateral ambipolar diffusion length; if any at all. Moreover it will provide a greater insight into the mechanisms that affect the lateral ambipolar diffusion length. For example, in Chapter 4 I have already found that increasing the population of the higher energy states in the quantum-dot and wetting-layer can lead to an increase in the lateral ambipolar diffusion length. However, with further increasing of the population in the wetting-layer, higher-order non-radiative recombination processes

decrease the apparent lateral ambipolar diffusion length. This later affect is presumably something that might also occur in the quantum-well system, in which case a significant reduction in the lateral ambipolar diffusion length might occur. Such a comparative study would also be useful as a function of temperature, as the mechanisms and recombination processes will most likely change the overall effect.

A temperature dependent study of the laser threshold dependence on ridge width has already been commenced on the D-RWG quantum-dot samples mention in Figure 7-1. The results of this preliminary investigation are shown in Figure 7-2, where it is seen that increasing the temperature increases the fractional change in threshold current density with decreasing ridge width. This observation is a supportive of the analysis in Chapter 4 where increasing the temperature was said to increase the thermal distribution of carriers in the quantum-dot excited states and also increase the likelihood of thermal re-emission of carriers into the wetting-layer. The net result of this increased thermal re-emission into wetting-layer process is an apparent increase in the lateral ambipolar diffusion length. Consequently there is an increased impact of either lateral out-diffusion losses or surface recombination (as is seen in Figure 7-2).

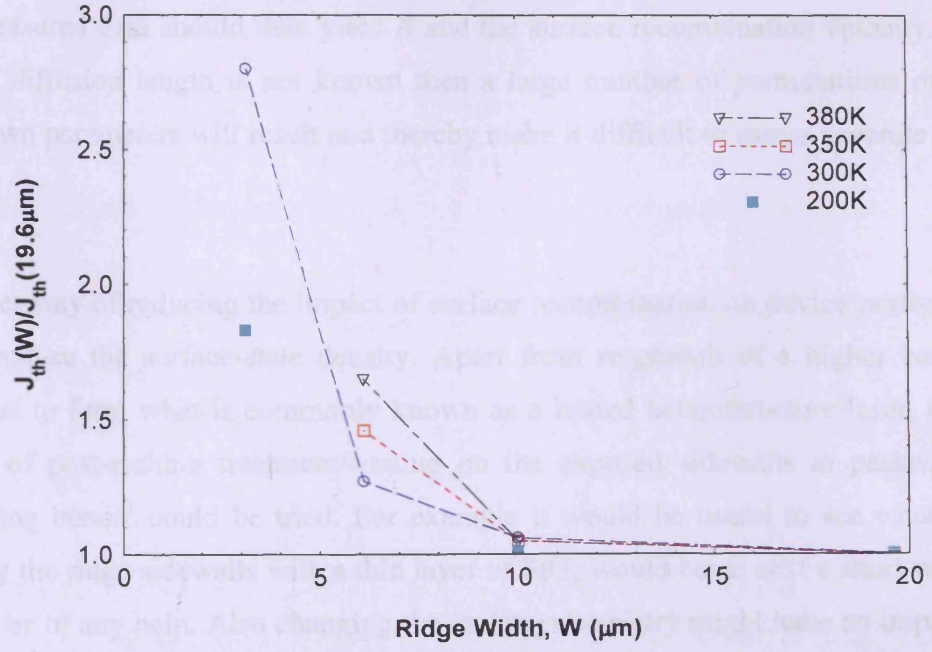

Figure 7-2. Fractional increase in threshold current density with respect to the 19.6 μm ridge ($J_{th}(W)/J_{th}(19.6\mu m)$) for D-RWG quantum-dot lasers of length 1.5 mm at various temperatures. The 3.1 μm ridge was found not to lase at 350 K and above.

(b)

By measuring the lateral ambipolar diffusion length in the quantum-well, it might then be possible to determine the surface recombination velocity from the measured non-radiative current density characteristics in Chapter 5. The approach would use a standard lateral ambipolar diffusion model similar to that used in Chapter 4 to model the lateral carrier density profile in the D-RWG structures. The boundary conditions in these devices would require: (1) a symmetrical carrier density profile about the centre of the ridge, and (2) the carrier diffusion current to be equal to the surface recombination current at the exposed sidewalls. This profile will have a dependence on lateral ambipolar diffusion length and surface recombination velocity. The total radiative recombination current density will then need to be found by:

$$J_B = \frac{d \cdot q \cdot B}{W} \int_{-W/2}^{W/2} n^2(x)$$

Where B is the radiative recombination coefficient and the other terms are the same as previously stated. The radiative recombination current density was found to be independent of ridge width at threshold. This condition could then be used to formulate a set of simultaneous equations for the radiative recombination current density in the various ridge widths. Solving these equations and best-fitting them to the measured data should then yield B and the surface recombination velocity. If the lateral diffusion length is not known then a large number of permutations of these unknown parameters will result and thereby make it difficult to assess accurate values.

(c)

Another way of reducing the impact of surface recombination on device performance is to reduce the surface-state density. Apart from re-growth of a higher band-gap material to form what is commonly known as a buried heterostructure laser, various forms of post-etching treatment/coating on the exposed sidewalls to passivate the 'dangling bonds' could be tried. For example it would be useful to see what effect coating the ridge sidewalls with a thin layer of SiO_2 would have, or if a short wet-etch would be of any help. Also changing the etching chemistry might have an impact e.g. adding BCl_3 to the chemistry to passivate the sidewalls during the etching might improve performance. The effects of these processes can all be assessed by characterising D-RWG multisection test-structures as a function of ridge width – as

was done in Chapter 5. This approach will then not only assess the changes in non-radiative surface recombination but also the changes in internal optical loss. This is important for correctly attributing any observed improvement or deterioration in the threshold current density performance to the correct mechanism.

(d)

During the course of the investigations in this project, a concept for a new test-structure was developed. This test-structure was intended to measure the lateral ambipolar diffusion length and surface recombination velocity without the need for separate studies on S-RWG and D-RWG devices. Its design is illustrated below in Figure 7-3:

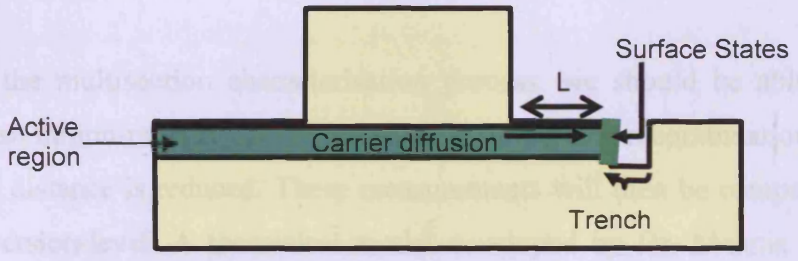

Figure 7-3. Schematic of the S-RWG test-structure with a deep-etched trench placed at a controlled distance L from the side of the ridge.

The test-structure is still designed for multisection device characterisation – thereby retaining the benefits of the characterisation technique that proved advantageous in studying the lateral out-diffusion effect and surface recombination velocity. The key points in its design are:

- Current spreading is eliminated by etching the ridge through the conductive upper-cladding region and down to the waveguide core.
- A 200nm wide deep-etch trench is placed at a controlled distance from the side of the ridge. This distance effectively varies the position of the surface-states. When the distance is on the order of the diffusion length, an increased fraction of carriers should be observed to recombine non-radiatively.
- The width of the ridge is typically 4 μm and is not varied. This width was chosen on the basis that as the trench distance is varied a significant effect on device performance should occur. For example, the effects on a broad area ridge of greater than 20 μm would probably be negligible. However, the width

of the ridge should not be too small so as to affect the gain-mode overlap as the trench distance is varied. From the study in Chapter 4, we know that this will probably only occur for widths smaller than 4 μm.

I have already done some preliminary development work towards fabricating such a device. The fabrication process is much more complicated than that of the RWG multisection test-structures. For example it requires: extremely accurate placement accuracy of an overlay pattern using EBL; the patterning has to be stable so as not to change the distance of the trench over the length of the device; multiple masking stages are required for the various etching stages; good mask definition to avoid transfer of serrated edges into the trench profile (otherwise a variation in the internal optical loss might arise); and the trench has to fully planarised and insulated. An example of a fabricated structure is shown in Figure 7-4.

From the multisection characterisation process, we should be able to measure the increase in non-radiative current density from surface recombination in the trench as trench distance is reduced. These measurements will then be compared as a function of inversion-level. A theoretical model developed by Dr. Meletis Mexis at Cardiff University has shown that the lateral ambipolar diffusion length and surface recombination velocity can be extracted from these measurements. In order to confirm the validity of the model and also the concept of this test-structure a full investigation is required. These measurements can be checked with S-RWG and D-RWG investigations as was done in Chapter 4 and Chapter 5.

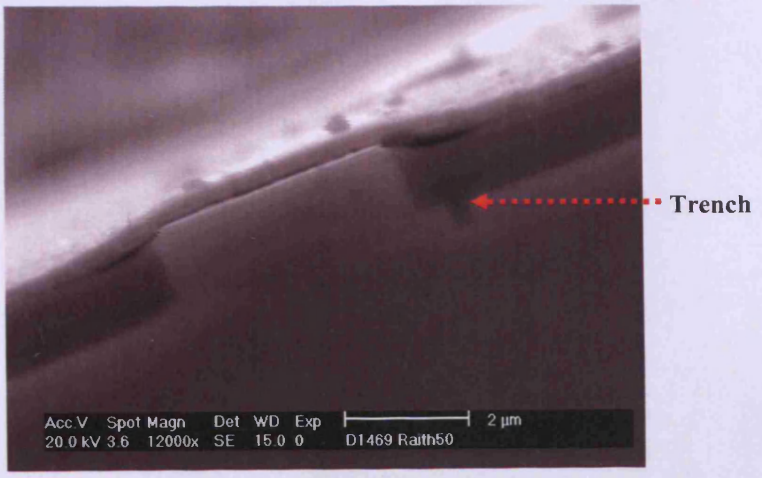

Figure 7-4. SEM image of a fabricated S-RWG test-structure with a deep-etched trench

Publications

- D. S. Naidu, A. Sobiesierski, M. Mexis, P. M. Smowton and H. D. Summers, "Surface recombination measurements on quantum dot and quantum well active regions: A comparative study," Semiconductor Integrated Optoelectronics (SIOE), 2007, Cardiff, UK. (Conference Poster)
- D. S. Naidu, A. Sobiesierski, M. Mexis, P. M. Smowton and H. D. Summers, D. Mowbray, H. Y. Liu, M. Hopkinson, "Role of Device Structure on the Performance of Quantum Dot Lasers." IEEE Lasers & Electro-Optics Society Annual Meeting (LEOS), 2007, Florida, USA. (Conference Presentation)
- D. S. Naidu, A. Sobiesierski, M. Mexis, P. M. Smowton and H. D. Summers, "Effect of Device Structure on the Performance of Quantum-Dot Lasers," Institute of Physics One Day Quantum-Dot Meeting, 2008, Imperial College, UK. (Conference Poster)
- D. S. Naidu, A. Sobiesierski, M. Mexis, P. M. Smowton and H. D. Summers, "Effect of Surface Recombination on In(Ga)As Quantum Dot Lasers," Institute of Physics QEP-18 Photon 08 meeting, 2008, Edinburgh, UK. (Conference Poster)